Preparation and characterization of silica, reduced graphene oxide and composite aerogels

by

Oznur Kaya

A thesis presented for the degree of

Doctor of Philosophy

School of Engineering

Newcastle University, UK

April 2021

Abstract

In this thesis, experimental results are reported on the synthesized of waterglass-based silica aerogels monoliths by mixing graphene oxide. The new ambient pressure approach is used to produce aerogels by using a mixture of sodium bicarbonate and water instead of low surface tension solvent. Furthermore, to enhance mechanical properties graphene oxide as nanofillers is added into silica matrix to synthesize composite aerogels based on sol-gel technology.

Furthermore, we report a simple method for obtaining reduced graphene oxide aerogels doped with different metal oxide nanoparticles, germanium dioxide (GeO_2), cobalt ferrite ($CoFe_2O_4$), and iron(III) oxide (Fe_3O_4) by using supercritical drying method. Firstly, all metal oxide nanoparticles are synthesized. Then metal oxide nanoparticles are added into graphene oxide solution and sodium bisulfide is utilised as a cheap reducing agent. Lastly, prepared aerogels' properties such as surface area, morphology, the chemical composition, and electrochemical measurements as an anode material for lithium-ion batteries are investigated.

Finally, ambient pressure dried graphene-based aerogels are produced with common devices by rewording a partially reduced graphene oxide hydrogel with an ice-template method. This work can be cost effective of high-performance graphene aerogels.

Scanning electron microscope (SEM), X-ray diffraction (XRD), uniaxial compression test, fourier transform infrared spectroscopy (FTIR), raman spectroscopy, Brunauer - Emmett - Teller (BET) theory and Barret - Joyner - Halenda (BJH) method are utilised to characterise the produced aerogels.

ACKNOWLEDGEMENTS

First of all, I would like to express my sincere gratitude to Allah for helping me in completing this thesis and Turkish government for the scholarship. I would like to thank to my supervisor for the comments on this dissertation.

I would also like to thank my lab mates for their help and support during my research.

My deepest gratitude goes to my parents Ibrahim Kaya and Ayse Gursel Kaya, without their continuous support, I could not finish my work.

I would like to thank my sister, my brother and his wife who provided happy distraction to rest my mind outside of my research.

Finally, I am truly thankful to Turkish government for the scholarship.

I dedicate this thesis to
my lovely nieces
Zeynep Sude and Ayse Dila.

Contents

List of Figures

List of Tables

Abbreviations

AM	Active material
APD	Ambient pressure drying
BET	Brunauer, Emmett and Teller
BJH	Barrett-Joyner-Halenda
BSEs	Back scattered electrons
CA	Carbon additive
$CoFe_2O_4$	Cobalt ferrite
DI	Deionised water
DMC	Dimethyl carbonate
EC	Ethylene carbonate
EDAS	Propyltrimethoxysilane
EtOH	Ethanol
Fe_3O_4	Iron (III) oxide
FTIR	Fourier transform infrared spectroscopy
GeO_2	Germanium dioxide
GO	Graphene oxide
HOMO	Highest occupied molecular orbital
IUPAC	International Union of Pure and Applied Chemistry
LiBs	Lithium ion batteries
LST	Low surface tension
LUMO	Lowest unoccupied molecular orbital
MTES	Methyltrimethoxysilane
MTMS	Methyltrimethoxysilane
$NaHSO_3$	Sodium bisulfide
NMP	N methyl 2 pyrolidone
OCV	Open circuit voltage
PEDS	Polyethoxydisiloxane
PFAS	Perfluoroalkysilane
PVDF	Polyvincylidene fluoride
rGO	Reduced graphene oxide
SEI	Solid electrolyte interphase
SEM	Scanning electron microscopy
SEs	Secondary electrons

TEM	Transmission electron microscopy
TEOS	Tetraethyl orthosilicate
TMCS	Chlorotrimethylsilane
TMOS	Tetramethyl orthosilicate
XRD	X-ray powder diffraction

Chapter 1 General review of aerogels

This chapter presents the progressive development of aerogels such as synthesis techniques and reinforcement techniques to improve mechanical and characteristic properties as well as developing their applications.

1.1 Foundations of Kistler about aerogels

The first aerogel was introduced by Steven Kistler in 1932. It was silica aerogel where within the gel, the liquid was replaced with a gas without collapsing the gel solid network (Kistler, 1931). Previously, the wet gels were dried by vaporization. Kistler carried out a supercritical drying method. The gel was heated to transform the liquid in gel pores into a supercritical fluid. This technique avoided the development of liquid–vapour meniscus at the exit of the gel pores, which is responsible for a mechanical tension of the liquid and a pressure on the pore walls, resulting in a gel shrinkage. The dried samples that were synthesized had a very open porous structure.

Kistler also produced organic and metal oxides aerogels from alumina, tungsten oxide, ferric oxide, tin oxide, nickel tartrate, cellulose, nitrocellulose, gelatine, agar, egg albumen, and rubber (Kistler, 1932). He studied the physical properties of silica aerogels, their structure, density, and thermal conductivity by varying the mechanical pressure with gases such as air, carbon dioxide, and chlorofluorocarbon (Kistler, 1935).

Consequently, silica aerogel was defined as the solid with the lowest thermal conductivity at atmospheric pressure (Kistler and Caldwell, 1934). In 1950s, one of Kistler's patents was assigned by Monsanto Corporation for large-scale production of silica aerogels for applications such as thickening agents and thermal materials (Carraher, 2005). However, Kistler's method became inefficient due to time-consuming procedures involved in the synthesis of aerogels and the high manufacturing cost. Later, the silica aerogels were firstly commercialized in 1969 as additives for toothpaste and cosmetics, and as thickening agents for paints (Maleki *et al.,* 2014). Afterwards, the organic and hybrid aerogels have also been developed, which further spread the areas of application of aerogels. These are available in the forms of beads, monoliths, fibres and composites which are now used in various applications such as drug delivery, biomedical, food processing, optics, shock absorbers, catalysts and energy storage (Paraskevopoulou *et al*., 2019; Gurav *et al*., 2010; Veronovski *et al.,* 2011).

1.2 Silica aerogels

Silica aerogels are nanostructured materials that have attracted considerable attention due to their properties such as low density, transparency, high surface area, high porosity and low thermal conductivity. Silica aerogels are commonly synthesized by following four stages in

processing: sol-gel process, ageing, solvent exchange, and drying (Heinrich *et al.,* 1995; Soleimani Dorcheh and Abbasi, 2008; Gurav *et al.,* 2010). Figure 1.1 shows the general steps in the production of silica aerogels. Sol gel process is a complex chemical synthesis procedure with the initial step of forming a gel from a precursor solution. It is generally used to describe any chemical process capable of producing ceramic oxides from the solution (Bhaduri, 1993). The ageing process provides the growth of a network to complete gelation. Solvent exchange is a selection of a drying solvent which designates the drying method. There are three common drying methods: freeze drying, ambient pressure drying, and supercritical drying. These drying techniques will be mentioned in more detail later in this chapter.

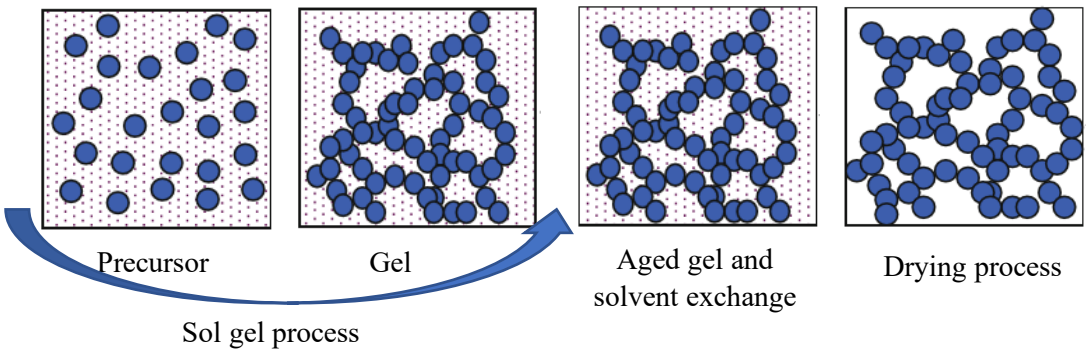

Figure 1. 1 General stages of silica aerogels synthesis.

Silica aerogels have often incorporated other varieties of compounds into the network, which then tends to enhance the properties of the synthesized composite materials compared to the monolithic silica aerogels. New hybrid materials have been developed which give more powerful, combined, and desired properties of composites (Sanchez, Belleville, Popall and Nicole, 2011). For instance, silica aerogels are fragile materials, when combined with organic or inorganic substances, exhibit better mechanical strength (Leventis *et al.,* 2002; Meador *et al.,* 2005). Besides, some additives in a transparent silica aerogel structure can eliminate the radiative thermal conductivity of the material and increase the thermal performance at high temperatures (Caponi *et al.,* 2004).

Additional components of the silica aerogel composite materials can be added in sol before or after hydrolysis of the silicon precursor (Meador *et al.,* 2005). In some processes, other components can be incorporated into the silica structure after gelation or after drying. Silica aerogel composites can be synthesized generally with organic or inorganic molecules and specifically with a precursor different from the silica precursor (e.g., titanium precursors), a metallic solid (e.g. Au, Pd), organometallic compounds, powders (e.g. carbon black), functional molecules or polymers (e.g. PMMA) (Leventis, 2007).

1.2.1 Sol-gel process

Silica aerogels are generally obtained from gels made through a sol-gel chemistry which is a process when a nanostructured solid network is formed in a liquid reaction medium as a result of a polymerization process generating siloxane bridges (≡Si–O–Si≡) between Si atoms delivered by precursor molecules (Zha and Roggendorf, 1991). Such transformations are the equivalent of a polymerization process in organic chemistry, where direct bonds between the carbon atoms of organic precursors are constituted resulting in linear chains or branched (crosslinked) structures depending on the type of reactive monomers and crosslinkers used (Dvornic and Owen, 2009). Dispersed solid colloidal silica particles (i.e., nanoparticles with a size well below 1 mm) lead to "more or less" linear oligomers that are created in the early stage of the sol–gel process. In the second stage, these elementary objects can link with each other while they are still in the solvent to make up a three-dimensional (3D) open network structure termed a gel, where size and shape is only limited by the container. The continuous transformation of a sol into a gel establishes the gelation process. The abrupt change from the liquid to the solid stage is entitled as the sol–gel transition. The gels that are produced are either colloidal or polymeric depending on the nature of the building blocks from which the network is combined of, whether they are nanoparticulate or more linear (polymer-like) like. For both stages, the driving reactions are hydrolysis and water and/or alcohol condensation. The first significant precursor for silica gels is sodium metasilicate Na_2SiO_3, also entitled waterglass (Venkateswara Rao *et al.,* 2004; Hwang *et al.,* 2007) which was used for the first silica aerogels reported in the literature (Kistler, 1932). This precursor reacts with an acid such as HCl as illustrated in equation (1.1). A salt that is generated has to be removed by tedious dialysis or by ion exchange for H+ through an acidic ion exchange column (Stojanovic *et al.,* 2019).

$$Na_2SiO_3 + 2HCl + (x-1)\,H_2O \longrightarrow SiO_2\,.xH_2O + 2NaCl \qquad (1.1)$$

However, metal alkoxide precursors are mostly preferred as a Si precursor. Alkoxide precursors can vary in type depending on the metal and side groups, named as ligands. The general form of a metal precursor is M(OR)x where M can be a silicon, titanium, aluminium or a transition metal, R is an alkyl group, and x is the number of alkoxide groups that the metal can have which determines the functionality and molecular conformation of the precursor (Baetens *et al*., 2010). The most common alkyl groups are methyl and ethyl groups, attached to the tetra–functional silicon atom. Thus, tetraethoxysilane (TEOS) and tetramethoxysilane (TMOS) are the most well-known silica aerogel precursor compounds having the molecular formulas of $Si(OC_2H_5)_4$ and $Si(OCH_3)_4$, respectively (Nakanishi *et al.,* 1998; Wagh *et al.,* 1999). In 1846, the first inorganic gels produced were in fact the silica gels made by Ebelmen from such precursors, but they were not dried by supercritical techniques to synthesize aerogels (Ebelmen *et al.,*

1846).There are some other silicon alkoxide precursors to prepare polymeric silica gels, such as polyethoxydisiloxane (PEDS) (Einarsrud *et al*., 2001; Zhou *et al.,* 2007), methyltrimethoxysilane (MTMS) (Venkateswara Rao, Bhagat, Hirashima and Pajonk, 2006), methyltriethoxysilane (MTES) (Harreld, Ebina, Tsubo and Stucky, 2002), 3-(2-aminoethylamino) propyltrimethoxysilane (EDAS) (Alié, Pirard, Lecloux and Pirard, 1999), Noctyltriethoxysilane (Rodríguez and Colón, 1999), dimethyldiethoxysilane (Venkateswara Rao and Haranath, 1999), and perfluoroalkysilane (PFAS) (Zhou et al., 2007).

There are four alkoxide groups which are tetrahedrally bound to the silicon atom making it tetra functional. The four alkoxide groups are evenly spaced in three dimensions leading to a net cancellation of dipole moments which result in a non–polar structure and immiscibility with water. Therefore, in order for hydrolysis reactions to occur, a necessity for a co–solvent arises with which both the precursor and water are miscible. The commonly used co–solvents are the alcohols of the alkyl groups attached to the silicon, such as ethanol and methanol for TEOS and TMOS, respectively. The co–solvents enable good miscibility and homogenous mixing of the precursor and water for hydrolysis reaction (Kauffman, 2000; Baetens *et al*., 2010). In addition to that, acid or base catalysts are widely used in order to accelerate the hydrolysis and condensation reactions. Figure 1.2 displays a typical sol–gel route for an alkoxysilane. Understanding the underlying chemistry of the sol–gel process is necessary for the improvement of the aerogel hybrid materials. The following subsections give detailed information about each step of the sol–gel process.

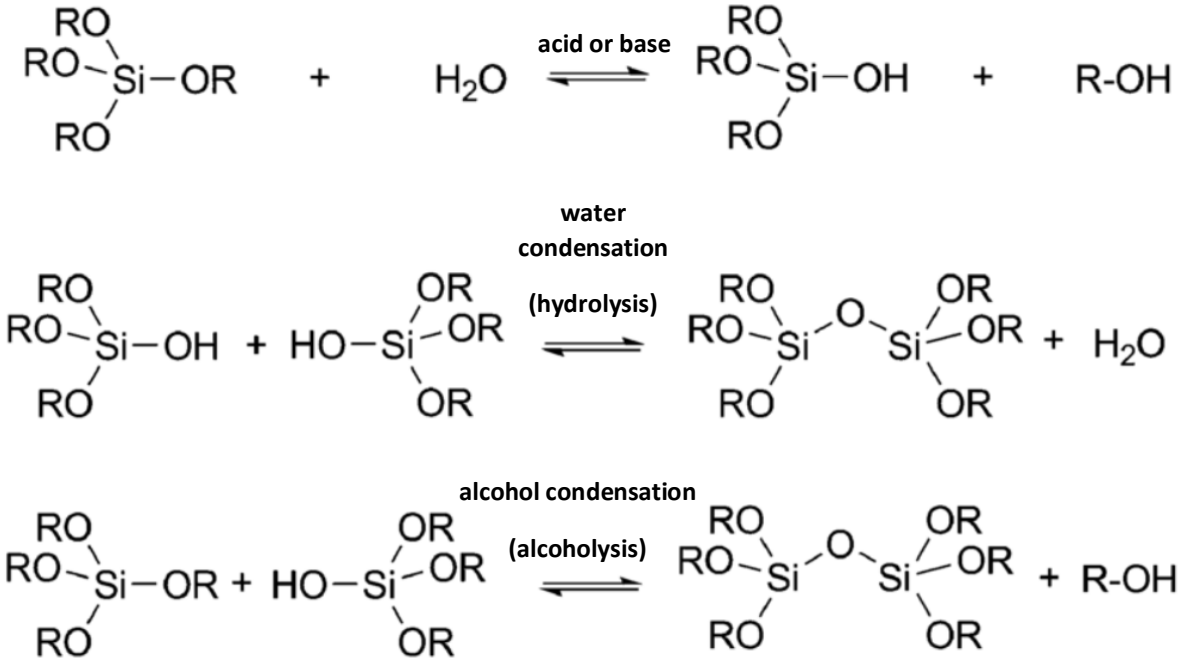

Figure 1. 2 A typical sol–gel route for an alkoxysilane (Maleki, 2016).

Hydrolysis:

It is the initial step of the sol–gel process which includes fundamentally the hydrolysis of the metal precursor, replacing the alkoxide groups (OR) with hydroxyl groups (OH). As mentioned above, the addition of the co-solvent provides the formation of a homogenous mixture of the precursor and water, thus enables the hydrolysis reaction of the precursor molecule.

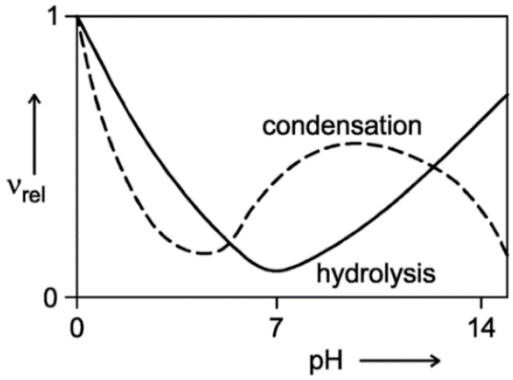

Figure 1. 3 Dependence of the relative rates of $Si(OH)_4$ hydrolysis and condensation reactions on the pH (Leventis et al., 2002)

The hydrolysis reaction takes place by nucleophilic attack of oxygen lone pairs of H_2O molecule on Si atoms (Livage, Henry and Sanchez, 1988). This nucleophilic attack includes bimolecular nucleophilic displacement reactions involving penta–coordinate intermediates or transition states (Baetens *et al*., 2010). The rate of the hydrolysis reaction and the condensation reaction are intensively pH dependent which can be observed from Figure 1.3 given above (Leventis *et al.,* 2002). Strong pH dependency of the hydrolysis reaction evokes the utilization of catalysts in order to achieve rapid and complete reaction. Depending on the catalysts used, the hydrolysis reactions can be attained in two different ways: acid and base catalyzed hydrolysis.

The rate and extent of the hydrolysis reaction is mostly dependent on the strength and the concentration of the acid or base catalyst utilized. The mineral acids are more effective catalysts than the equivalent concentrations of base catalysts (Baetens *et al*., 2010).

In addition to pH and form of catalyst, the reaction to hydrolysis is also affected by steric and inductive effects, the ratio of water to silicon and solvent effects. Steric conditions have the greatest effect on the precursor's hydrolytic stability. The hydrolysis rate is mostly reduced by bulky, branched alkoxide groups, which explains the delayed hydrolysis of TEOS compared to TMOS (Hagemans *et al.,* 2018). Although the increased water-to-silicon ratio tends to facilitate hydrolysis, this increase will decrease the condensation reaction rate resulting in an increase in gelation time as water is also the condensation reaction by-product. On the other hand, the form and physicochemical properties of the solvent used, such as a polarity, dipole moment and

viscosity, are important as the solvent regulates the silicate and water concentrations that affect the gelation kinetics (Danks, Hall and Schnepp, 2016).

Condensation:

Condensation is essentially a polymerisation reaction of precursor species of hydrolysed / unhydrolyzed silica to form siloxane bonds. This reaction to polymerisation will occur in two different ways depending on the product type. Firstly, when an un-hydrolyzed precursor molecule interacts with a hydrolysed molecule in alcohol, it produces condensation reaction, and leaves the alcohol group. Secondly, the condensation occurs also when the reaction of two hydrolysed precursor molecules form the water molecule (Issa and Luyt, 2019). In Figure 1.4, the reaction schemes for these two separate condensation reactions are presented (Lamy-Mendes, Silva and Durães, 2018).

The most complicated step of the sol – gel cycle is the condensation step as all reactions are reversible and occur simultaneously. Therefore, condensation is initiated during hydrolysis, and the formation of siloxane bonds usually starts before the hydrolysis reactions are completed, making it much more difficult (Pierre, 1998). Condensation reactions similar to hydrolysis also have a high pH dependence which can be observed from Figure 1.3. There are two forms of condensation reactions as shown in Figure 1.3, in which acid and base are catalysed while condensation of silanols can proceed thermally without involving catalysts. The overall condensation rate is reduced at around pH 1.5 and it is maximised at intermediate pH (Suib, 2013).

Condensation happens between the more condensed species. This implies that the dimerization rate is small but, once dimers are formed, they preferentially react with monomers to form trimers, which in turn react with monomers to form tetrameters. More development results in the introduction of lower species of molecular weight to more condensed species and the aggregation of condensed species to form chains and networks (Baetens *et al*., 2010).

Kinetics of the condensation reaction is affected by both inductive and steric influences. Reduced steric crowding in the state of transition or on intermediate molecules improves the kinetics of condensation while the large groups attached to silicon delay the condensation. The form of the solvent used in condensation kinetics is also efficient, similar to hydrolysis (Baetens *et al*., 2010).

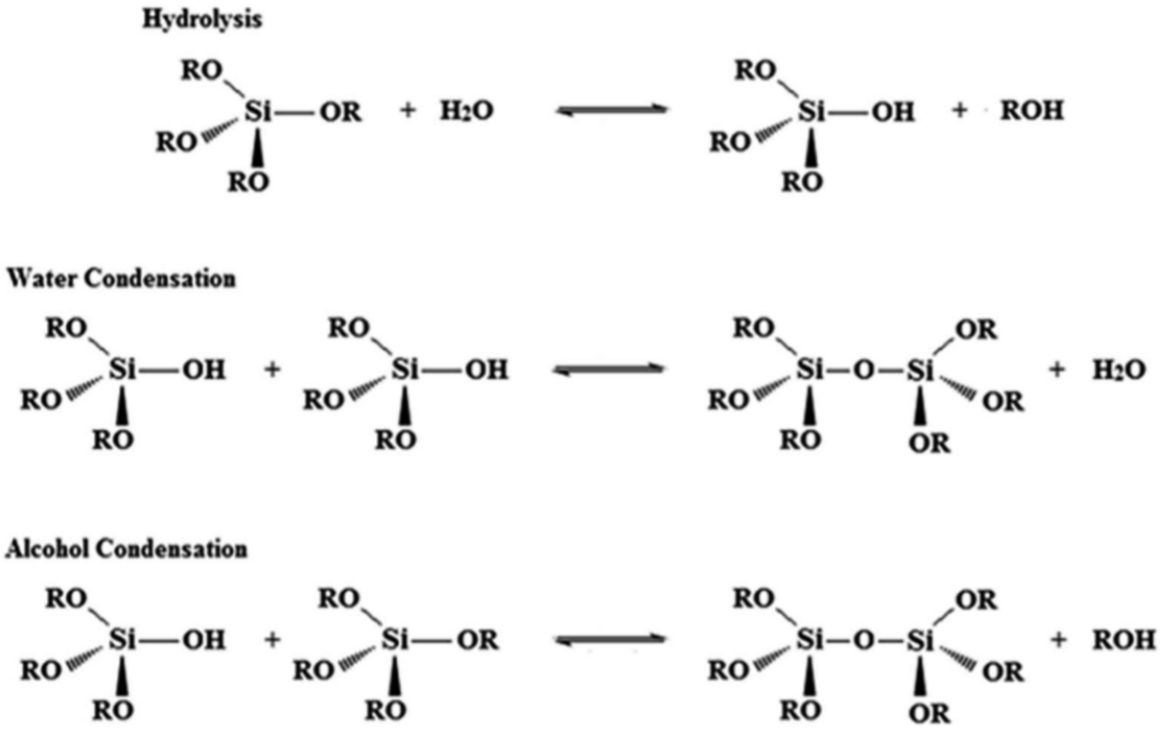

Figure 1. 4 Overview of condensation reactions. The first step is alkoxysilane hydrolysis, followed by water condensation and alcohol condensation of the newly formed silanols (Lamy-Mendes, Silva and Durães, 2018).

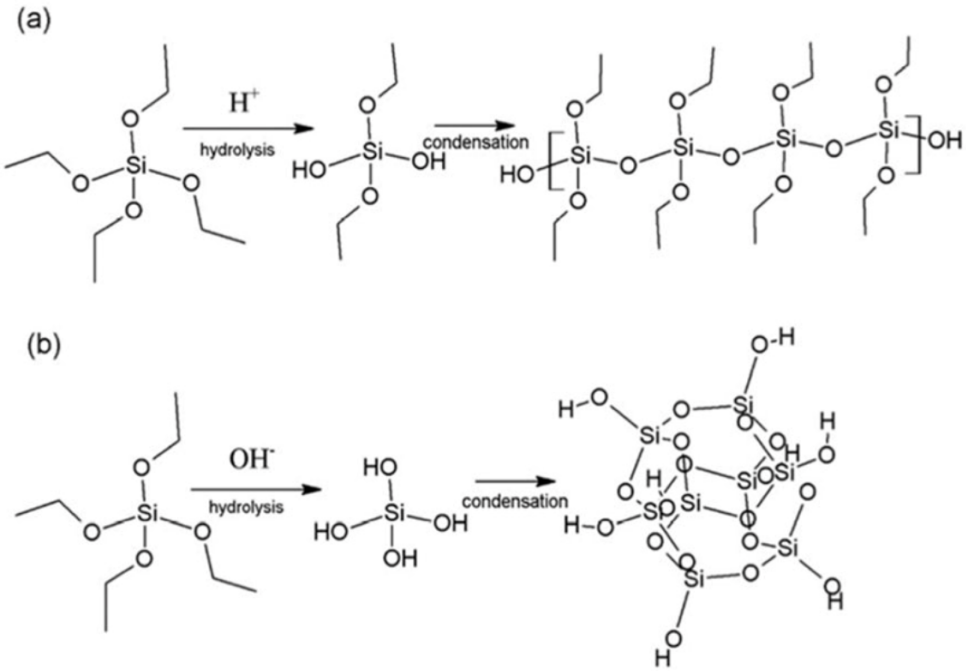

Figure 1. 5 Schematic description of the sol-gel reaction using (a) acid and (b) basic catalyst (Vieira, Panzera, Ferrari and Schiavon, 2018).

The form of the catalyst used during hydrolysis and condensation reactions has a major influence on the solid network microstructure. An open network structure is initially allowed for acid-catalyzed reactions, followed by further hydrolysis and co-condensation reactions. On the other hand, highly cross-linked large sol particles are initially obtained in base catalysed

reactions which eventually are linked together to form gels with the creation of large pores between the interconnected network of particles. Gel structures are shown in Figure 1.5 for the acid and base catalysed reactions (Baetens *et al*., 2010; Leventis *et al.,* 2002; Capadona *et al.,* 2006).

The reverse reactions of siloxane bonds (alcoholysis and hydrolysis) by alcohol and water condensation will cause the bond breakage and re-formation allowing for continuous reconstruction of the polymers. These reverse reactions also have a pH-dependence similar to condensation reactions and have a deciding role in the re-distribution of siloxane bonds and solid network structuring (Baetens *et al*., 2010).

Gelation:

Gelation takes place when links between the colloidal sol particles are formed by hydrolysis and condensation reactions. These assemblies occur to such an extent that a massive cluster of spans passes through the containing vessel. At this point, with the high viscosity mixture, when the vessel in which the reactions occur is tipped, it does not spill. However, there are still many sol particles that remain in the spanning cluster. They are trapped and entangled species within this spanning cluster. There is a high viscosity but low elasticity of this initial gel. This is not an endotherm or exothermic reaction, nor any distinct chemical change happens at the gel point. Only the sudden rise in viscosity can be observed as illustrated in Figure 1.6 (Baetens *et al*., 2010).

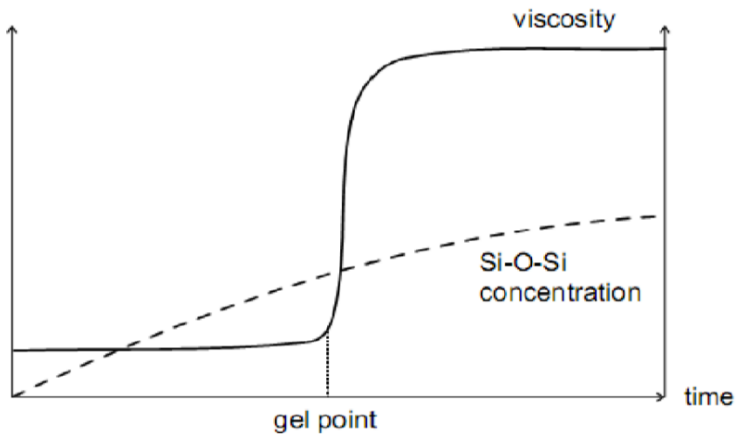

Figure 1. 6 Evolution of viscosity and Si–O–Si as a function of time (Baetens et al., 2010).

Further cross-linking and chemical incorporation of isolated sol particles into the spanning cluster continue after the gelation, causing an increase in elasticity. The gelation time is used as a measure of the total condensation kinetics, since it is inversely proportional to the average condensation rate (Baetens *et al*., 2010).

Aging:

The chemical reactions to the gel formation are not completed (Hench and West, 1990). It is due to the existence of an additional probability that the gel network will continue to expand in the gelation solvent during a process called "aging" phase. Indeed, the gelation solvent within the pores includes the reactive species (such as –OH) or unreacted monomers that can further condense with each other on the network. In general, the entire ageing cycle takes from hours to days by soaking the gel in the initial solvent or appropriate solvent under managed conditions (Zha *et al*., 1991; Davis *et al*.,1994). The key role of ageing is to strengthen the gel, the mechanical strength of the tenuous aerogel network. In the ageing process, the network particles undergo several phenomena where the "Ostwald ripening' or "coarsening" is the most important one (Reichenauer, 2004). The Ostwald ripening stems from the fact that entities or molecules in the aggregates (or in solution) dissolve from the less energetically preferred (convex) locations and accumulate on the more energetically preferred (concave) network sites, i.e. on the neck region or network contact points, thereby strengthening and coarsening the network (Otterstedt and Brandreth, 1998). Some parameters, including pH, time and temperature, are the most important variables that can affect the ageing process kinetics (Davis *et al.,* 1992; Hench and West, 1990; Hench and Ulrich, 1986). Additionally, during the ageing process, most of the textural properties, such as pore size, porosity, and surface area of synthesised gels, change. Aging is recognised as a simple and robust network enhancement technique and has been explored in many works with the goal of strengthening the gels as prepared (Einarsrud *et al.,* 2001; Nadargi *et al*., 2008).

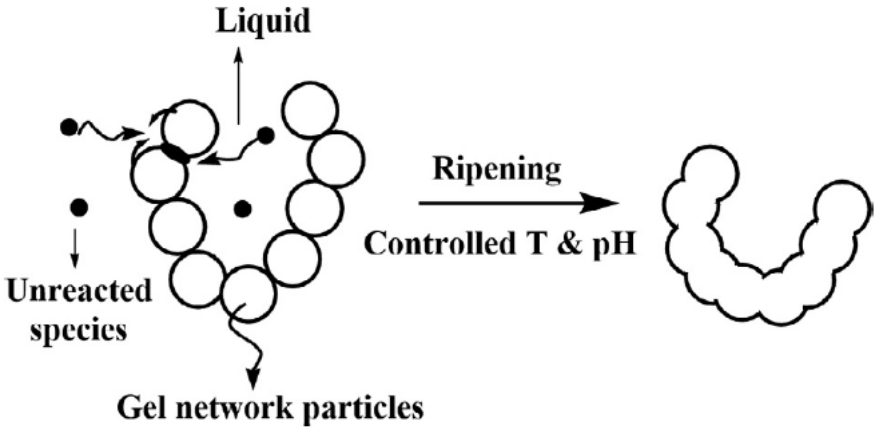

Figure 1. 7 Ostwald ripening phenomenon on gel nanoparticles during the aging process (Maleki, 2016).

Drying:

Drying is removing the liquid from the pores by replacing it with air, which is one of the most critical steps in the sol-gel cycle. Due to the nano-porous structure of the gels, drying is typically problematic as removing the filler liquid interferes with the pore structure resulting in altered material properties. During drying, the destruction of the pore structure occurs caused by the capillary stresses created in the pores due to the phase boundary of the liquid-gas. Therefore, capillarity is a key parameter that dominates the formation of aerogels when silica gels dry (Kistler, 1931). When aerogel pores are modelled as cylinders, the capillary pressure in those pores (P) satisfies the Young – Laplace equation (Equation (1.2)) (Rowlinson and Widom, 2013).

$$P = \frac{2\gamma\cos\theta}{R} \tag{1.1}$$

where γ is the solvent surface tension, θ is the contact angle between the solvent and the surface and R is the radius of the pore in the wet gel. The pores diameters in the gel are of the order of nanometers, so the gel liquid exerts a high hydrostatic pressure. The meniscus in the pores and the forces of surface tension seek to pull the particles together as the liquid evaporates in the pores. Such forces can behave in such a way that the pores (i.e the structure) collapse. Thus, gels that have very small pores appear to crack and shrink when drying (Gurav *et al*., 2010). As a result, in order to make an aerogel, one must avoid crossing the phase boundary of vapour – liquid. The latest methods used in aerogel fabrication to prevent pore collapse can be classified into three general techniques. Due to surface tension effects each is designed to reduce or remove the capillary forces. These techniques are supercritical drying, freeze drying, and following surface modification ambient pressure drying techniques (APD) (Bisson *et al*., 2003). Gels are dried at a critical point in supercritical drying methods to remove capillary forces as described below.

As soon as the liquid begins evaporating from the gel, surface tension produces concave meniscus in the pores of the gel. As the liquid evaporation begins, compressive forces build up across the pore's surface and it contracts. Ultimately, surface stress causes the gel body to collapse (Mandal *et al*., 2019). As shown in Figure 1.7, the gel is dried supercritically in an autoclave to prevent the surface tension from building up (Gurav *et al*., 2010).

As the temperature and pressure in the autoclave rises above a certain point, the liquid is converted into a "supercritical" fluid in which each molecule can pass freely, and the surface tension stops. Meniscus do not form without a surface tension. The vapours are then released gradually from the autoclave until atmosphere pressure is reached by the pressure in the

autoclave. Lastly, the system is depressurized which results in a gaseous process inside the pores. Since no phase boundary is encountered in the cycle, removal of the pore fluid is accomplished without compromising the structure of the aerogel. Since CO_2 is fairly non-toxic and cheap, it is the most commonly used solvent in supercritical drying processes because of its strong solvent capacity for alcohols as the pore liquid is typically an alcohol in the sol-gel phase. Additionally, CO_2 has mild critical conditions with a critical temperature of 304 K and an easily reachable critical pressure of 74 bar. Figure 1.8 displays the pressure-temperature cycles during the alcohol's supercritical drying (Gurav *et al.,* 2010).

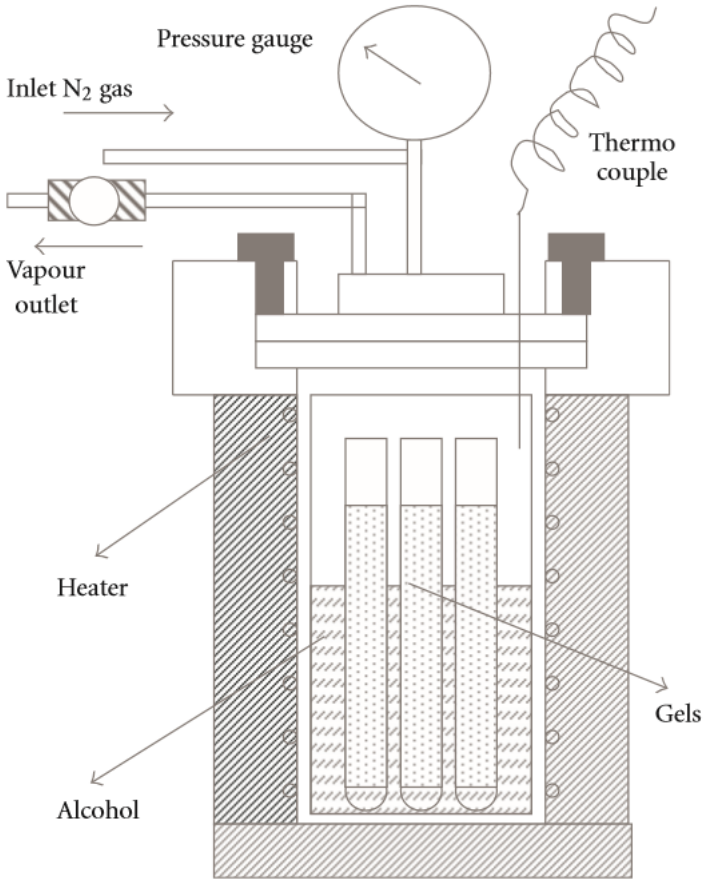

Figure 1. 8 Schematic representation of supercritical drying autoclave (Gurav et al., 2010).

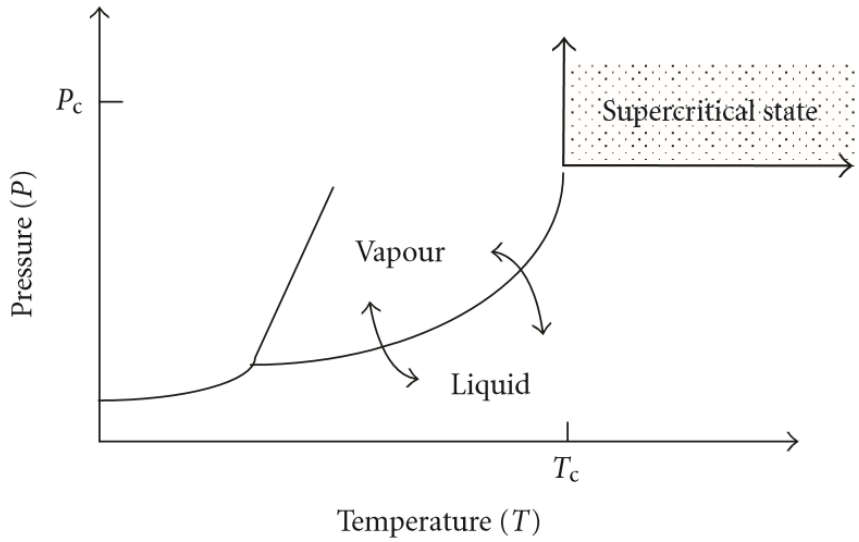

Figure 1. 9 Pressure-temperature correlation for phase equilibrium diagram of the solid-liquid-vapour system (Gurav et al., 2010).

Another option to prevent phase boundaries during drying between the liquid and the gas process is freeze drying which is a simple, economical, and eco-friendly drying approach used to prepare aerogels with reasonable porous structures (Zuo *et al.,* 2015).

The end products are called "cryogel" with maximum 80% porosity and just half of the surface area of their aerogel equivalent (Maleki, 2016).

Several pre-drying gel treatments exist which can improve the structure of the gel. For instance, long ageing, a solvent exchange with a low expansion coefficient and strong sublimation pressure, can afford a better end properties aerogel. Freezing rate is also a crucial parameter and correlates with the ice crystals (shape and size) that can affect the consistency of the pore structure in the resulting aerogel. A rapid freezing rate, for example, also leads to small ice crystals, resulting in products with small pore sizes and high pore surface. In comparison, the slow freezing rate results in large ice crystals, resulting in an aerogel with relatively large pores (Fricke, J. and Emmerling, A, 2010).

Compared to their supercritical CO_2 counterparts, the high volume of macroporosity, a significant amount of shrinkage and lower specific surface area are more prominent in cryogels (Kalinin *et al*., 1999; Pajonk *et al*., 1990). At a practical point of view, the aerogels that have been extracted from a hydrogel or a gel prepared from an aqueous solution (e.g. cellulose, PI, PVA, pectin) may be dried by freezing process although sometimes the ice within the pores may cause their porous micro-fibrillary structures to fail in part. The low freeze-drying temperature favours the production of aerogels used for medical study because high temperatures can harm the medicine (Maleki, 2016).

Traditionally, silica aerogels have been synthesised using supercritical drying processes, but this has some disadvantages in terms of cost effectiveness, process consistency and protection as it needs high temperature and pressure to reach the critical point. If liquid carbon dioxide is used as a solvent during the supercritical drying process at low temperatures, the chemical toughness of the aerogels in the atmosphere will slowly decrease since the aerogel particles are hydrophilic. A commercially appealing ambient pressure drying (APD) system has been introduced for the development of silica aerogel to solve these problems (Zha and Roggendorf, 1991). In this process, the surface of the wet gel is chemically changed by removing hydrophobic functional groups by removing H with hydroxyl groups followed by drying at the ambient pressure. On the adjacent silica cluster, surface silanol groups (Si – OH) undergo condensation reactions resulting in an irreversible shrinkage of the gel network during drying, as shown in Figure 1.9 (Gurav *et al*., 2010). This process can create extremely low- surfaces energy that dramatically reduces the surface tension. Therefore, alcohol surfaces are modified with sufficient modifying agents and the aerogel surface is made hydrophobic.

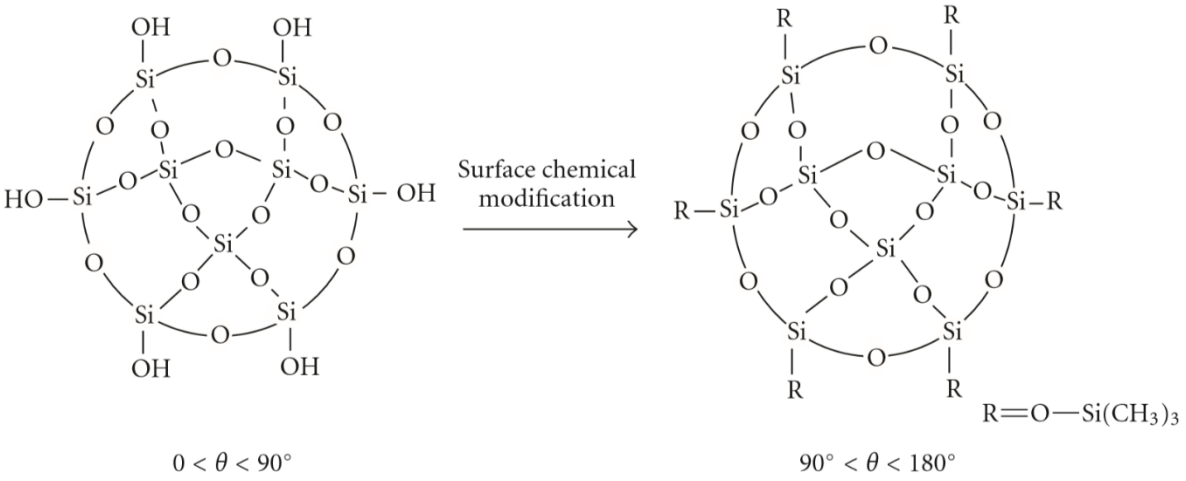

Figure 1. 10 Surface chemical modification of the gel (Gurav et al., 2010).

There are some substances such as hydrophobic reagents that can change the surface's wetting properties. These include methyltrimethoxysilane (MTMS), dimethylchlorosilane (DMCS), trimethylchlorosilane (TMCS), trimethylethoxysilane (TMES) and so on. Gel surface modification by replacing H from Si – OH with non-polar alkyl or aryl groups is a key step in the method of drying ambient strain. It prevents silica cluster condensation reactions and prevents the gel from shrinking during drying by extension (Gurav *et al.,* 2010). Since ambient pressure drying can reduce the aerogel production costs, its value has shifted from a field of solely scientific interest to practical use.

Han and Siller (2015) have recently developed a new approach to ambient pressure drying by reducing the exchange of solvents and the process of surface modification, which in turn

reduces the cost of synthesis of silica aerogels. The novel ambient pressure drying process makes use of sodium bicarbonate solution, as a substitute of organic low surface tension (LST) solvents, to produce CO_2 gas in the wet gel pores drying the gel at certain temperature. This process has been inspired from the life cycle of a damselfly and in particular from the drying manner of their wings. Solvent that exists in gel pores in traditional APD evaporates immediately from the gel surface. Different LST solvents have been explored with a view of rising a capillary strain. Figure 1.10 (a) shows a schematic of the traditional APD technique and usage of a solvent. If the wet gel is exposed to a mixture of sodium bicarbonate solution and TMCS, carbon dioxide is created inside the bulk of the silica gel without any modification to the surface. Within the wet gel, this process generates pressure, CO_2 bubbles, and the produced CO_2 is trapped within the gel, partially dries gel, and trapped CO_2 gas opposes to the capillary pressure. The strain, which is created by CO_2 production, prevents the wet gel structure from collapsing during the drying of the ambient pressure. The aerogel is dried and has hydrophilic properties. Figure 1.10 shows the difference in process between APD using an organic low surface tension (LST) solvent and APD using inorganic sodium bicarbonate solution (Han and Siller, 2015; Han *et al.,* 2018).

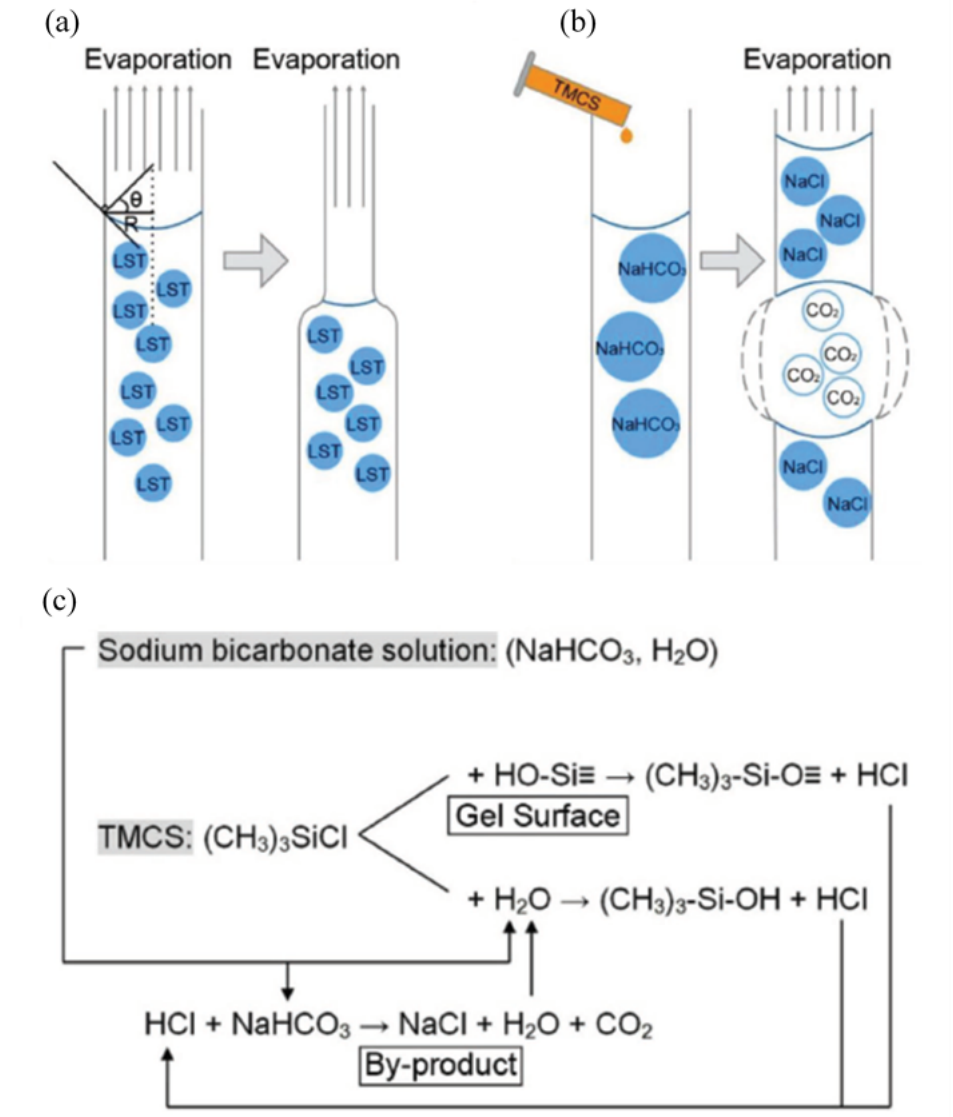

Figure 1. 11 A schematic diagram of methods of drying at the atmospheric pressure of aerogels. (a) Traditional APD with organic solvent LST. (b) APD by inorganic solution of sodium bicarbonate. (c) Proposed net-chemical reaction route of the TMCS ((CH3)3SiCl) and sodium bicarbonate solution, in APD process by Han et al. (2018).

1.3 Structure and Properties of Silica Aerogels

Silica aerogels are highly porous materials which consist of up to 99% air and less than 1% silicon dioxide (Hrubesh, 2010). Silica aerogels are the most widely studied and used type of aerogels among the various organic and inorganic aerogels. They are amorphous materials with a disordered molecular structure across their solid network, with tortuous paths (Lamy-Mendes, Silva and Durães, 2018). Silica aerogels are mesoporous materials that have pores in a range of 2-50 nm. The solid skeleton of silica aerogels consists of so-called secondary silica particles with sizes 5-10 nm (they look as they are arranged on a string like random beads). Such secondary particles are composed of primary silica particles, formed from non-porous, dense silica. The air-filled voids between the secondary particles are the so-called pores which have nanometres-sized widths. Figure 1.12 illustrates the structure of nano-scale silica aerogels

(Thapliyal and Singh, 2014). They have the unique properties described in Table 1, the majority of which occur due to their highly porous structure. For starters, they have extremely high specific surface areas and low densities because of their high porosity, so that they are one of the lightest solid materials extracted so far. They do have a monolithic construction which means they can be built in any shape or size. Its transparency is another significant property of silica aerogel. The light scattering property of aerogels basically differs with the solid network and pore structures that can be tuned to precursor form, composition of the materials, and processing conditions such as the temperature during synthesis. Consequently, clear, translucent, or opaque aerogels can be obtained by modifying the above variables for different applications. Aerogels are materials which have the lowest values of thermal conductivity of any solid known to date. They possess even lower thermal conductivities than still air. In ambient conditions, standard thermal conductivity values of silica aerogels differ in the range of 0.010–0.020 W / mK. Because of this unique thermal property, the thermal insulation applications of silica aerogels have gained tremendous interest. The basic reasons for the low thermal conductivity of silica aerogels are described in the section below (Bhaduri, 1993; Leventis *et al*., 2002; Capadona *et al.,* 2006; Cai *et al.,* 2012).

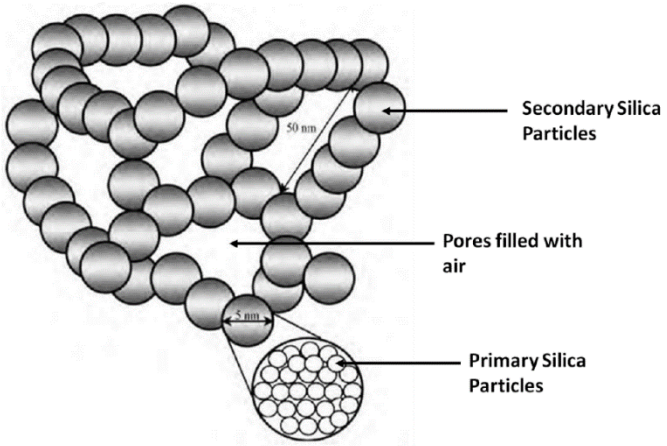

Figure 1. 12 Structure of silica aerogels at nanometer scale (Thapliyal and Singh, 2014).

Table 1 Properties of silica aerogels

Property	Value	Comment
Density	~0.003g/cm^3	one of the lowest density solids (Maximiano *et al.,* 2019).
Porosity	80–99.8%	high porosity (Hrubesh, 2010).
Surface Area	500–1200 m^2/g	determined by nitrogen adsorption/desorption (BET) (Soleimani Dorcheh and Abbasi, 2008)
Mean Pore Diameter	20–150 nm	mostly in mesoporous range (Soleimani Dorcheh and Abbasi, 2008)
Thermal Conductivity	0.017–0.021 W/m.K	high thermal insulation property (Soleimani Dorcheh and Abbasi, 2008)
Thermal Tolerance	up to 1100 ºC	shrinkage starts at 500ºC and increases with temperature. melting point is 1200ºC (Cai *et al.,* 2020)
Index of refraction	~1.05	low for a solid material (Soleimani Dorcheh and Abbasi, 2008)

One of the most vital aspects of silica aerogels is that their properties can be tailor-made for specific applications and hence silica aerogels have wide variety of utility areas such as acoustic insulation, catalyst support, optical applications, low dielectric constant materials, batteries, and many others (Soleimani Dorcheh and Abbasi, 2008). Although it does have many interesting properties, there is one inadequate characteristic of silica aerogels: they are highly brittle substances unable to endure mechanical loads, which causes difficulties in processing and handling, and accordingly limit their vast use in a quite number of application fields. Because of weak interactions among the strong silica network elements, aerogels are very fragile materials that are insufficient to bear even a small quantity of mechanical loading. Therefore, even small cracks in the microstructure damages the entire shape and makes manufacturing of monolithic and crack–free silica aerogels distinctly challenging. However, these problems can be overcome by reinforcing silica aerogels with polymers in such a way that monolithic, crack-free silica aerogels can be obtained with improved mechanical properties. Some of the remarkable studies that attempted to improve silica aerogel composites with polymers are described in the following section.

1.4 Mechanical reinforcement of silica aerogels

In the literature, various techniques are reported to strengthen silica aerogels' mechanical properties (Leventis *et al.,* 2002; Randall *et al*., 2011). The purpose of such methods is to develop aerogels of low density that can be easily deformed and exhibit a capability to absorb shock energy at some stage in bending and compression (Guise *et al*., 2001).

As previously mentioned, the aging of wet gels results in mechanically stronger inorganic networks (Reichenauer, 2004) by improving the strength of the final silica aerogels by dissolving and re-precipitating the silica at the inter-particle neck surface (Lucas *et al*., 2004). With this process, the elasticity modulus will achieve an improvement of approximately one to two factors. But clearly, a reinforcing agent is only the silica at the end; therefore, it remains as a brittle substance with poor tensile strength.

An alternative solution is the hybridisation of silica aerogels (Kramer *et al.,* 1996; Yim *et al.,* 2002) promoting co-gelation of silicon alkoxide with hybrid precursors such as poly(dimethylsiloxane) (PDMS) for strengthening purposes. Gels thus obtained are called "ORMOSIL" (ORganically MOdified SILica) Hybrids. They have the flexibility of rubber-like amore. With the 20 wt.% PDMS, they can be compressed elastically to 30% (by volume) without damage (Kramer *et al.,* 1996).

Compounding of an inorganic aerogel network with various chemical procedures is carried out with polymeric systems. This method results in a massive rise in the tensile strength and the aerogel robustness (Leventis, 2007). Additionally, incorporation of various fibrous support materials, such as polymeric fibres (Li *et al*., 2009), carbon nanofibers (Leventis, 2007) and fibreglass (Yuan *et al*., 2012) into the aerogel systems has also proved to be positive in enhancing the mechanical properties of aerogels. The fibre matrix can aid the aerogel and reduce aerogel bulk size inside aerogel-fibre composite matrix (Chakraborty *et al*., 2017). By this time, fibre and silica aerogel composites have been manufactured using various methods to strengthen the structure of silica aerogels.

The subsequent sections below will cover the above-mentioned mechanical reinforcement techniques of the silica aerogels based on updated literature survey on the subject.

Structural reinforcement of silica aerogels:

The trifunctional organosilane compounds of the type are generally $RSiX_3$ (where, in groups R = alkyl, aryl, or vinyl, X = Cl, or alkoxy) which generate flexible aerogels with decreased overall bonding and good hydrophobicity (Ochoa *et al*., 2012; Parale *et al*., 2018) due to the fact that one of the ends of Si atom incorporates a non-hydrolysable R group. Because of the presence of this organic group, R attached to the silica polymer chains reduces the interchain bonding resulting in an elastic and flexible three-dimensional matrix (Venkateswara Rao *et al.*,

2006). Kanamori and others (2007) have proven that MTMS-derived gels can have reversible deformation upon compression. The molecular structure of the silica aerogels derived from MTMS is shown schematically in fig 1.13 (Kanamori *et al*., 2007). The elasticity of these aerogels has been studies with respect to the Young's modulus (γ), the use of uniaxial compression measurements. It was possible to obtain aerogels with a high elasticity, durability and with Young's modulus as small as 1.094×10^4 $N.m^{-2}$. They related the easiness of condensation and hydrolysis reactions within the silica precursor to the length of methyl and methoxy groups since these are the smallest of all alkyl and alkoxy groups (Hegde and Venkateswara Rao, 2007; Venkateswara Rao *et al.*, 2006).

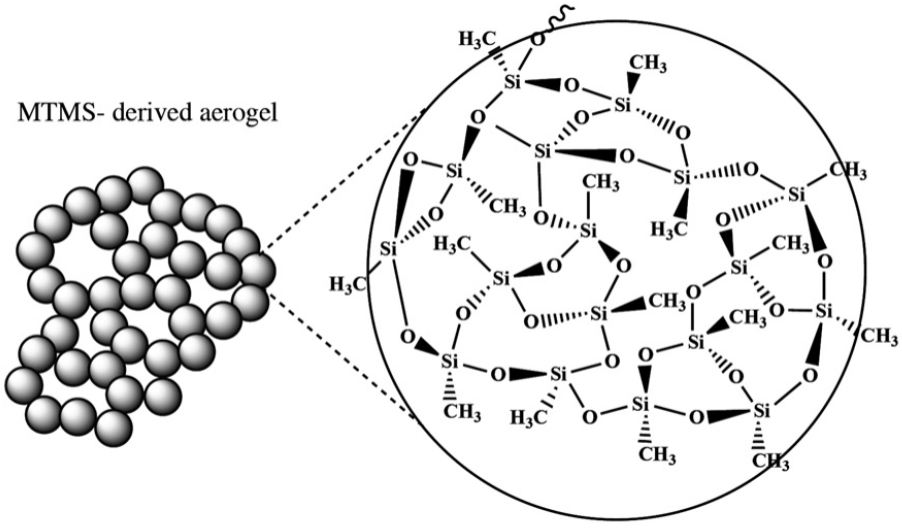

Figure 1. 13 MTMS-derived three-dimensional aerogel network with its detailed molecular structure (Kanamori et al., 2007).

A confined determination of the monofunctional and difunctional organosilane compounds of the kind $RSiX_3$, R_2SiX_2 as properly as $X_3Si\text{-}RSiX_3$ bis silane precursors, in which R is an alkyl or aryl group, is illustrated in fig 1.13 (Maleki, Durães and Portugal, 2014). In this figure, various organosilica precursors are grouped under different categories, and different aerogels with different material properties can be synthesized from them. Any of these precursors for silica contains different organic functionalities that are useful for surface decoration or aerogel surface treatment to add one's needs. To some degree, the inorganic-organic (hybrid) materials (ORMOSIL) that can be derived from these precursors combine the most significant properties of their constituents, such as high clarity (glass-like), low processing temperatures (polymer-like) and adequate thermal stability (silicone-like) and are easily prepared due to the specific availability of the precursors concerned (Maleki, Durães and Portugal, 2014).

In addition to simple precursors to metal or silicon alkoxide (for example, TMOS) that, after hydrolysis and condensation, resulting in the formation of an inorganic oxidic network with most effective siloxane (Si-O-Si) bonds. The organo (alkoxy) silanes, relying on what sort of functionalities they have, can be used to comprise polymerizable organic substituents, including epoxy, vinyl, or methacryloxy groups, into the final aerogel product (Randall *et al*., 2011). In such molecules the Si\C bonds are stable under the mild conditions of sol – gel processing (Pandey and Mishra, 2011).

Besides, hybrid organo (alkoxy) silane precursors, silica backbone crosslinking with more flexible, elastic alkyl bridged bis-silane precursors can increase aerogel strength continuously (Maleki *et al.,* 2014). For instance, Randall and others (2011) have studied the relative value of three types of bis-silane precursors on epoxy-reinforced silica aerogels with different lengths of the alkyl groups. They applied four types of bridged alkyl-connected bis-silanes and a difunctional silica precursor showing extended chemical structures in Figure 1.14. In the case of the co-gelation with TEOS of bridged bis-silane precursors, the flexible alkyl links / bridges between the secondary silica particles, depending on the size of the bridge, that give the network flexibility. Both these precursors enhanced the aerogel's elastic recovery with an amount as high as 15% contained in the silica backbone. This research team also reduced Si-O-Si bond numbers by use of DMDES, a difunctional silane, by lowering the stiffness of the silica network to enhance the elastic response (Randall *et al*., 2011). It has been reported that polyvinylmethyldimethoxysilane (PVMDMS) polymers which are efficient and multifunctional reinforcing agents were used for strengthening methyltrimethoxysilane-based silica aerogels (MSAs). PVMDMS reinforced MSAs display a perfectly elastic recovery property, the compressive strength of which ranges from 0.19 to 1.98 MPa (Wang *et al.,* 2019).

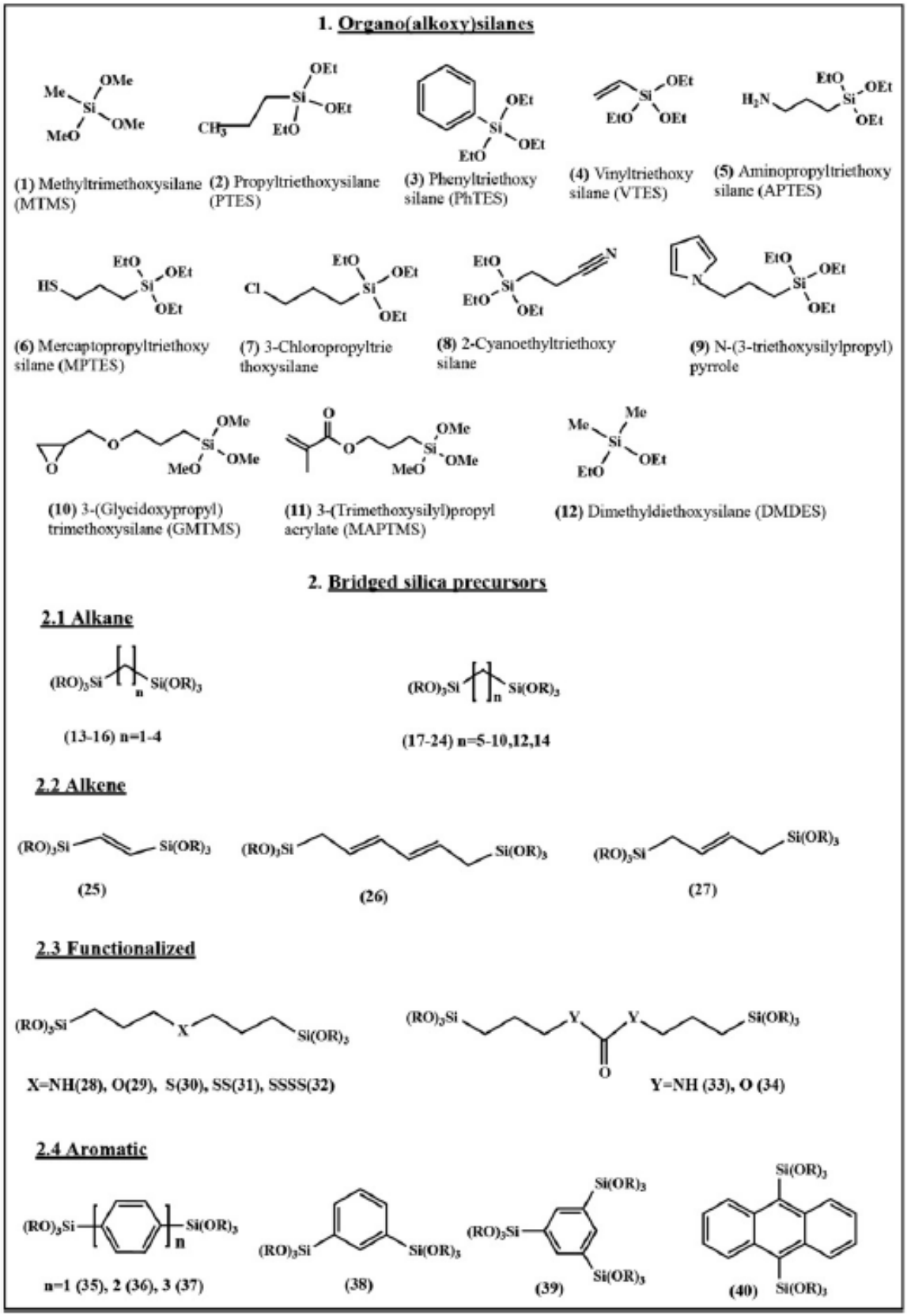

Figure 1. 14 Organo (alkoxy) and bridged silanes used in sol – gel-derived (hybrid) products as precursors (Maleki, Durães and Portugal, 2014)

Polymer reinforced silica aerogels:

It has been proven that the silica backbone, when mixed with polymer, improves the mechanical strength up to three orders of magnitude just by doubling the density over those of native or non-reinforced aerogels (Maleki, Durães and Portugal, 2014). Different types of interfacial interactions of secondary silica particles (inorganic parts) with appropriate functionality of organic polymers can achieve compounding of the silica network with polymer (Fu et al., 2019). Polymer / sol – gel composites are classified into two categories depending on the chemical relationship between the polymer and the surrounding silica network: Class I hybrid composite aerogels and Class II hybrid composite aerogels (Salimian *et al*., 2017).

Class I hybrid composite aerogels are formed by weak interactions, such as Van der Waals bonding, electrostatic forces or hydrogen bonding between the organic and inorganic parts (Tiwari and Mahanwar, 2018). Organic compounds, pre polymers or even polymers are incorporated in this form of composite materials through the inorganic matrix being completely independent from each other. Such materials are synthesised by the introduction of several different paths, for example inorganic network formation by hydrolysis and condensation of precursors to silica, in the presence of organic compound or polymerization of organic monomers in porous inorganic host. The most notable examples of class I are organic dyes or biomolecules embedded in porous sol – gel matrix (Raman, Sudharsan and Pothiraj, 2012). The guest molecules are dissolved physically together with inorganic host precursors (e.g., TEOS, or TMOS) or introduced to the sol state, and ended up captured within the gel that comes about from condensation and drying of the blend (Maleki, Durães and Portugal, 2014).

Though the resulting hybrid gels are highly transparent and thermally stabile without any phase separation between the two materials, there is no clear example of this composite family for the purpose of mechanical strengthening of native silica aerogels. In fact, with the addition of an inorganic SiO_2 filler, this class of hybrid materials is commonly used to enhance the very weak mechanical properties of organic polymers such as polysiloxanes polymer (PDMS) (Fragiadakis *et al.,* 2006; Fragiadakis and Pissis, 2007).

Since post - gelation washing is frequently needed in the processing of silica aerogels, class I hybrid silica composite aerogels are rarely studied. This is because of the weak interfacial bonds that exist between both phases, and therefore easy liquidation of the polymer silica pores by extensive exchange of solvents, that occurs during either the post-gelation washing steps or solvent moving into pores of the gel during the supercritical drying process (Fu *et al.,* 2019).

In practical terms, the ambient dried aerogel-like class I composites are more useful, because they are cost-effective and easy to synthesise. Additionally, the removal of the post-gelation

process steps is an advantage for the additional mass production of this kind of materials (Maleki, Durães and Portugal, 2014).

The composite network that applies to Class II hybrid aerogel composites is when the interfacial linkages are based on tight covalent bonds between the organic phase and silica. This method usually includes molecular precursors containing a chemical connexion between elements of the inorganic network that is hydrolytically stable in shape with organic moieties throughout the stage of sol gel. The polymer binds at points along the skeletal frame of 3D nanoparticle assemblies in these materials, and the resulting composites are called polymer cross-linked aerogels. The advantages of such materials that have both organic and inorganic parts is that they are unique in properties are they are expected to be individually distinctive organic or inorganic products (Maleki, Durães and Portugal, 2014).

Enhancement mechanical properties of silica aerogels by using secondary materials:

Studies have shown that different additives such as nanoparticles, fibers or nanofibers serve as a reinforcing scaffold of the aerogel construction and provide the aerogel network with a strong physical structure, as a result of which aerogels are flexible and mechanically strong (Maleki, Durães and Portugal, 2014).

The graphene oxide (GO), which has a unique two-dimensional structure (Podsiadlo *et al.,* 2007), has recently been considered as a promising nanofiller for 3D architectures (Compton and Nguyen, 2010). Prior research showed that reducing graphene oxide (rGO) was successfully integrated into silica aerogels matrices. For example, Patil, (2019) have reported that graphene-reinforced silica aerogel nanocomposite shows a higher stiffness compared to the monolithic silica aerogel. This nanocomposite aerogel gave a high deformation resistance and demonstrated greater rigidity and a high maximum indentation force.

Lei et al., (2017) found out that when applied to the silica aerogel matrix as a nanofiller, GO has a positive impact on the comprehensive performance of silica aerogels. Schematic illustration of the formation of composite aerogels is shown in figure 1.15. The compressive force is increased as the GO mass content increases. Composite aerogel 's compressive modulus with 0.4 wt%, 1.0 wt%, 5.0 wt% are 0.356 MPa, 0.361 MPa, or 0.394 MPa, respectively. Comparing the weak mechanical strength of silica aerogels, the authors explained that the increased mechanical properties of silica aerogel can be inked with the added strength of GO due to the rooting effect of anchoring of GO 's chemical interaction with nanoparticles. The other reason is that when the aerogels have external force, the impact of the rivet can inhibit the slipping, dropping and collapse of GO nanoparticles. In addition, the GO nanosheet can prevent further spread of cracks, which can destroy fracture energy parts (Lei *et al.,* 2017).

Figure 1. 15 Schematic illustration of the formation of composite aerogels (Lei et al., 2017).

Graphene oxide is a nano-filler, which does not only improve mechanical properties but also enhances physical properties. For instance, Dervin and others, (2017) reported that graphene oxide was mixed with sodium silicate to synthesize GO/silica aerogels in various weight percentages of GO to improve the physical properties of silica aerogels. The integration of GO inside the silica matrix has increased the surface area from 390 m^2/g (pure SiO_2 aerogel) to 798 m^2/g (with 2.2 w% of GO in SiO_2 aerogel) (Dervin *et al*., 2017).

1.5 Silica aerogels applications

Since aerogel's chemical and physical properties are so diverse, it is not surprising that there have been many applications. The general overview of aerogel applications based on such basic characteristics are presented in Figure 1.16 (Akimov, 2003; Gurav *et al.,* 2010). Besides all these applications, hybrid silica-gelatin aerogels exhibit both fast and retarded drug release properties (Kéri *et al.,* 2020). Zhao et al (2020) studied to produce 3D printed silica aerogel materials by direct ink writing of a slurry of silica aerogel powder. The printed materials include entirely of hydrophobic silica aerogel. The 3D-printer process eliminates subtractive manufacturing problems and opens up new applications for silica aerogels (Zhao *et al.,* 2020). Wang et al (2019) reported that graphene doped silica aerogels as sorbents delivered high CO_2 sorption capacity of 6.02 mmol g^{-1}. Woignier et al (2018) studied to synthesize silica glasses from silica aerogels by using viscous flow sintering model. In addition, this viscous flow sintering method provides to calculate the viscosities of aerogels at different temperatures.

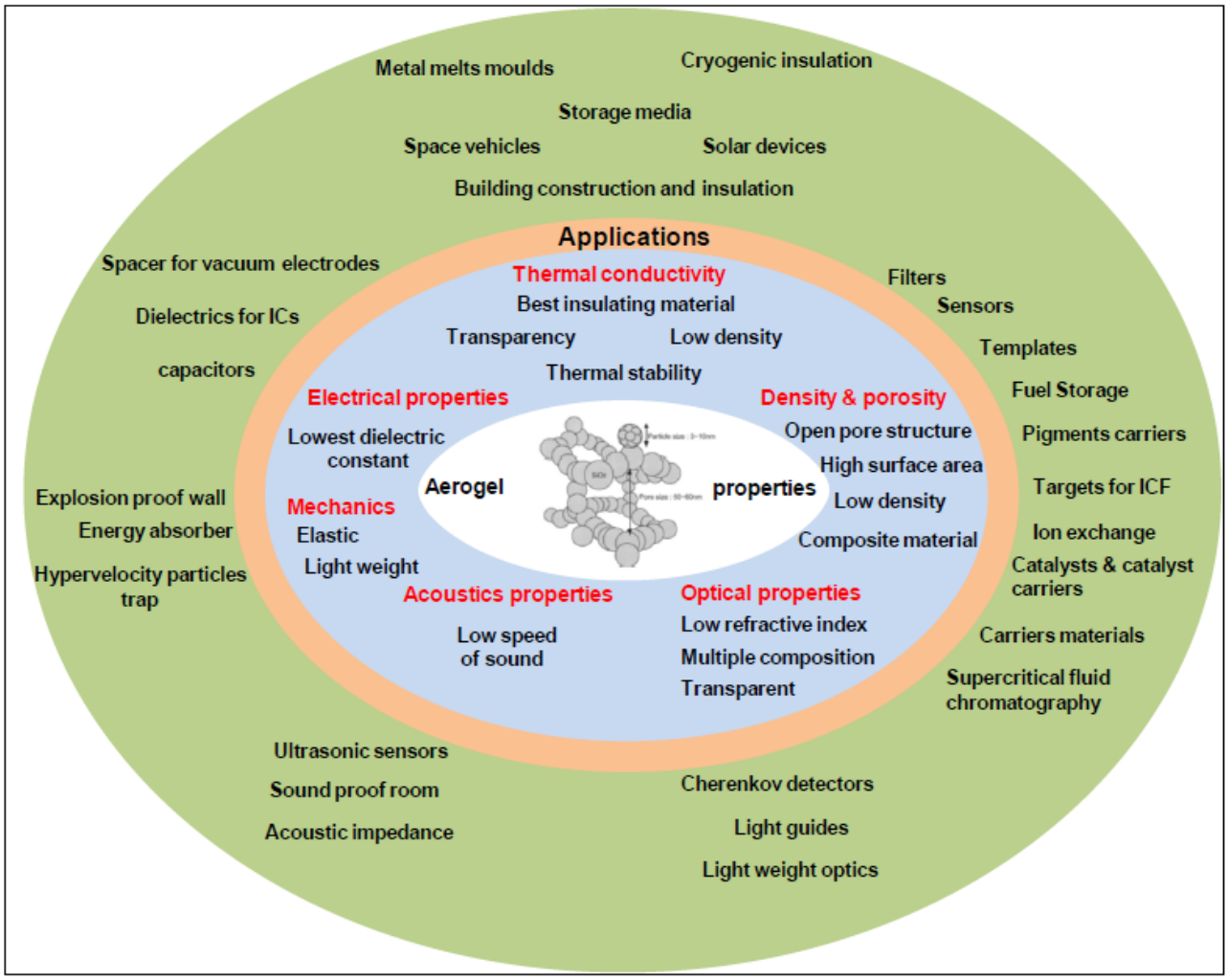

Figure 1. 16 The general overview of aerogel applications (Akimov, 2003; Gurav et al., 2010).

Heat Transfer in Aerogels:

As previously indicated, the isolation applications of aerogels have achieved attention due to their superior insulation properties compared to conventional insulation materials.

Conduction, convection and radiation are the three primary processes by which heat can be transferred. Nevertheless, certain components that contribute to each of these processes vary from those of homogeneous media to those made from porous materials like aerogels. For example, due to the fine pores of aerogels (2–50 nm) the flow of the gas molecules inside their pores has been reduced. Thus, the contribution from convection heat transfer is negligible for structures that are consisting of pores smaller than 1 mm at environmental pressure (Lee *et al.,* 2002). Consequently, convection heat transfer for aerogels is not pronounced. The transfer of heat is accomplished by phonon conduction of the solid matrix and gas phase conduction due to the collisions between the gas molecules and the pores. The heat transfer between the interfaces and grain boundaries is generally achieved by radiation. The schematic

representation of different heat transfer mechanisms in a porous material that consists of interconnected pores is shown in Figure 1.17 (Balaji *et al.*, 2014). All these mechanisms apply simultaneously, which can be presented as parallel resistors in the circuit; thus, the total thermal conductivity in the aerogels is the sum of these terms (Balaji *et al.,* 2014):

$$\lambda_{total} = \lambda_{solid\ conduction} + \lambda_{gaseous\ conduction} + \lambda_{radiation}$$

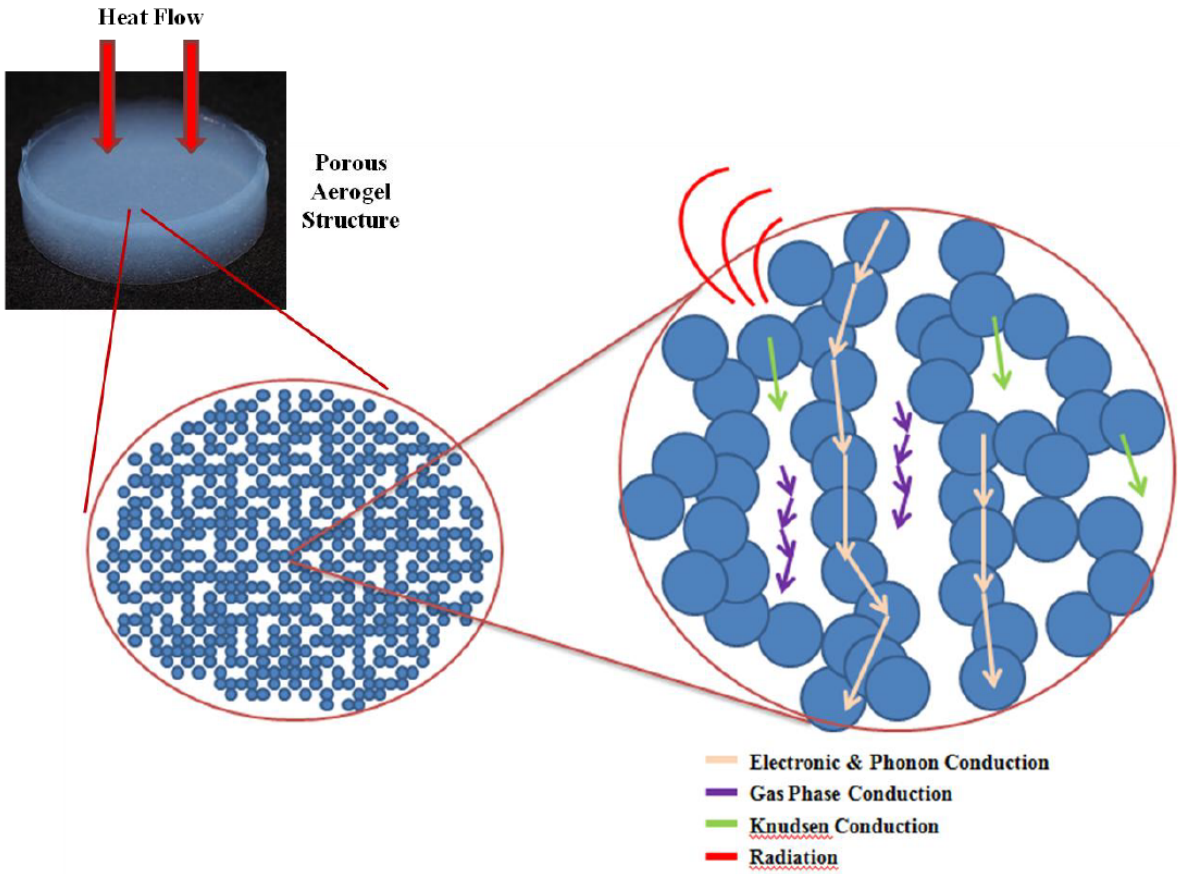

Figure 1. 17 Mechanisms of heat transfer in a porous environment (Balaji et al., 2014).

Aerogel as adsorbent:

Silica aerogels are an ideal filter or sorbent medium due to their highly specific surface area, high porosity and non-toxic nature of the silica element. Hrubesh, Coronado and Satcher (2001) published a comparative analysis for the cleaning of certain hydrocarbon components (i.e. toluene, ethanol, chlorobenzene) from wastewater and compared the fluorinated silica aerogel and granular activated carbon. For the high and low water miscible components, the capacity for adsorption of the modified silica aerogels exceeded that of comparable granular activated carbon by 30 to 130, respectively. It has been reported that flexible silica aerogel based on MTMS is an appropriate absorber for decontamination of seawater from crude oil (Abolghasemi Mahani *et al.,* 2018). Thakkar et al. (2020) synthesized composite aerogels made from reduced graphene oxide nanofillers and used them as the current sorbents for oil spills

inside highly porous SiO_2. Experiments with oil sorption showed that composite aerogels are highly active oil sorbents with around seven to eleven times of the sorbent mass.

Aerogel as a catalyst:

In a variety of industrial and environmental processes, catalytic CO and oxidation of hydrocarbons are considered significant reactions. These contaminants are usually eliminated by complete oxidation in a catalytic reactor including noble metals supported on metal oxide monoliths as catalysts. Al Soubaihi *et al.* (2020) reported that Pd/SiO_2 aerogel catalysts were produced by sol-gel synthesis method using supercritical drying. The catalyst has been tested for carbon monoxide (CO) oxidation reaction under ignition/extinction conditions. The produced catalyst exhibited a high catalytic activity at low operating temperatures (<200 °C) compared to unsupported Pd nanoparticles (Al Soubaihi *et al.,* 2020). Posada *et al.* (2019) studied to synthesize ceria-silica (CeSi) catalytic aerogels. These aerogels display catalytic activity towards CO at high temperature (600 °C) (Posada *et al.,* 2019).

Yousefi Amiri, Moghaddas and Rahmani Khajeh (2015) synthesized copper–silica aerogel via a sol – gel synthesis of silica supports with lower cost precursor water – glass. Copper- silica aerogel catalysts' behaviour and selectivity have been investigated by methanol steam reforming reaction, which has yielded good results for the hydrogen manufacturing process.

1.6 Other applications of silica aerogels

Commercial production of aerogel "blankets" began around the year 2000. The aerogel blanket is typically a silica aerogel with a fibrous reinforcing compound that transforms the breakable aerogel into a robust and flexible material. The mechanical and thermal characteristics of the product may be different depending on the different types of fibre reinforcement, aerogel matrix and composite pacification additives. A Spaceloft is an innovative and lightweight blanket that contains a fine layer of aerogel directly in the fabric. It was developed by Aspen Aerogels Inc. of Marlborough, Massachusetts. Another type of aerogels is organic (made of carbon and hydrogen atoms). The aerogel insoles and the sleeping bags were used by mount Everest climbers (Gurav *et al.,* 2020).

NASA has utilized aerogels to capture particles of space dust on the Stardust spacecraft. The particles vaporise with solids and go through gases, but they can be trapped in aerogels. NASA have used aerogels on Mars Rover and have made space suits out of aerogels for thermal insulation. The US Navy finds aerogel garments to be passive thermal protection for divers (Gurav *et al.,* 2020).

1.7 General review of graphene aerogels

Graphene oxide (GO) is an ideal precursor for preparing 3D graphene structure because of its high dispersion in aqueous media and its functionality. GO is also a perfect starting material to produce graphene-based aerogels (GAs), since the oxygen moieties present at both the basal planes and edges can react covalently with a variety of compounds, yielding new materials with properties that can be adapted to specific applications (Tiwari *et al.,* 2020). For example, energy storage, catalyst supports, supercapacitor (Korkmaz and Kariper, 2020), and thermal insulation are common specific applications (Yue *et al.,* 2016). In this thesis, application areas of graphene aerogels were mentioned with detail in chapter 4, page 90.

1.7.1 Structural characteristics of graphene aerogels

The structural characteristics of GAs involve low density, high porosity, large surface areas, excellent electrical conductivity, good mechanical strength, and great compressibility (Li *et al.,* 2020). Because of these properties, GAs can be very useful in electrodes by supplying conductive channels for the transmission of both lithium ions and electrons, as well as by serving as a buffer matrix for volume changes to stabilize the electrode structure. Many researchers have been working on developing successful structures using different graphene composites. Graphene's large specific surface area and loose structure allow electrolyte to penetrate more easily, improving the electrochemical properties of composites in LIBs (Tang *et al.,* 2021).

In the recent times, GAs, which show a 3D spherical configuration at the macroscale and a porous network structure with proper central divergent micropore channel at the microstructure, have great interest. Compared to the other forms of aerogels, GAs have a greater accessible surface area, a managed shape and size, and tailored pore structures (Wang *et al.,* 2015; Zhao *et al.,* 2016; Zhang *et al.,* 2020).

Furthermore, monolithic GAs, which have a macroscopic structure that varies depending on the container's size and volume, are typically generated in simple cubic or cylindrical reactors. The aerogels' macroscopic size can be easily controlled by modifying the container's volume. Monolithic GAs usually have homogeneous pore structures inside and outside, and the microstructure can be controlled by adjusting concentration of GO. Since monolithic GAs have a relatively complete three-dimensional network structure, compression can change their pore size (Fig. 2.1d) (Zhang *et al.,* 2015). Monolithic GAs can be made in a variety of techniques, for example chemical vapor deposition (Chen *et al.,* 2013), ice template method (Zhuo *et al.,* 2018), hydrothermal method (Kotal *et al.,* 2017), and 3D printing method (Zhu *et al.,* 2015). Based on the preparation method, the pore structure varies. For example, the pore structure of

the GAs produced using the ice template technique can be a unidirectional honeycomb porous structure or a bidirectionally arranged layered structure (Zhi *et al.,* 2021). Additionally, the GAs can be produced with heart-shaped (Fig. 2.1b) (Li *et al.,* 2020), swan-shaped (Fig. 2.1c) (Shang *et al.,* 2020), cylindrical (Fig. 2.1a) (Sun *et al.,* 2013) and other shapes depending on the various moulds used in the preparation process.

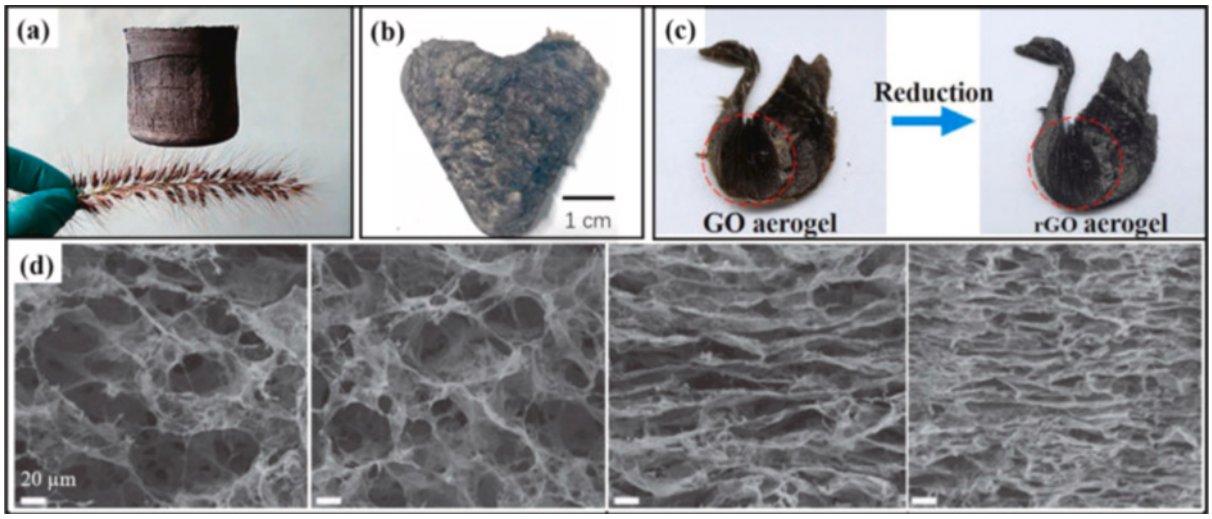

Figure 1. 18 GAs in different shapes. (a) Cylindrical (Sun et al., 2013). (b) Heart-shaped (Li et al., 2020). (c) Swan-shaped (Shang et al., 2020). (d)The cross-sectional SEM images of the GAs under different compressive strains of 30%, 60%, and 90%, correspondingly (Zhang et al., 2015; Zhi et al., 2021).

Chemical reduction;

The reduced graphene aerogels produced via hydrothermal do not have any chemical reagents, so the prepared aerogels have no impurities. However, the harsh nature of the hydrothermal reaction environment restricts the practical application of GAs to a certain extent. The chemical reduction method requires a lower temperature than the hydrothermal method does. NaHSO3 (Tong *et al.,* 2018), ethylene diamine tetraacetic acid (EDTA) (Tang *et al.,* 2019), ethylenediamine (EDA) (Shu *et al.,* 2020), ascorbic acid (Xu *et al.,* 2019), hexamethylenetetramine (HMTA) (Moon *et al.,* 2015), and hydrogen iodide (HI) (Li *et al*., 2017) reducing agents are widely used.

Reduced graphene oxide aerogels were prepared by using chemical reduction methods in this thesis for chapter 4 and chapter 5. Furthermore, reduction mechanism and hydrogel formation were explained with detail in chapter 5, page 109.

Chemical cross-linking;

The 3D porous network structure of GAs is generally connected via weak physical interaction between GO nanosheets, for example electrostatic interaction, hydrogen bonding and π-π interaction. As a consequence, the porous structure can be irreversibly deformed or collapsed (Zhi *et al.,* 2021). Chemical cross-linking can synergistically enhance the structural stability of

GAs through strong covalent bonds and weak non-covalent bonds, corresponding to the formation of aerogels through weak physical interactions. In recent years, different types of cross-linking agents have been improved to obtain the GAs, such as polymers, metal ions and small organic molecules (Cui *et al.,* 2020). As shown in Fig. 2.2a-e, Ye et al. (2017) developed a method for cross-linking GO and poly (vinyl alcohol) (PVA) with glutaraldehyde (G) to produce a series of lightweight, amphiphilicity-controllable, and shape-recoverable cross-linked GAs. For both GO sheets and PVA, the G molecule is an efficient cross-linker (Hong *et al.,* 2015). Intermolecular acetalization was achieved when the aldehyde groups of G molecules interacted with neighbouring hydroxyl groups on the surface of GO sheets and PVA chains. GAs showed a honeycomb-like cellular structure with interconnected pores and had high elasticity, allowing them to be squeezed and bounced back at high speed (Fig. 2.2f-h) (Ye, Liu and Feng, 2017).

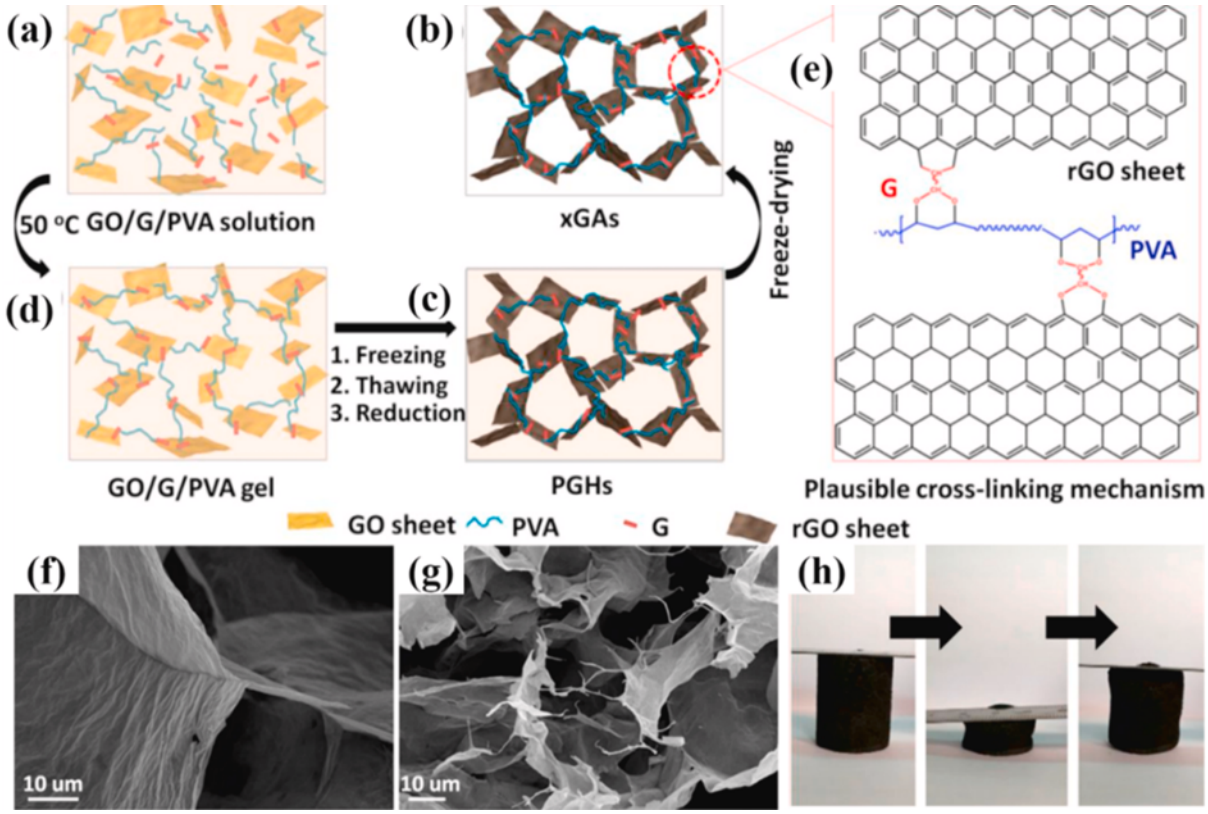

Figure 1. 19 Schematic showing the formation of PVA/graphene hydrogels and PVA/GAs. (e) A plausible cross-linking mechanism between PVA and RGO sheets through G molecules. (f–g) At high magnification showing the corrugated cell walls. SEM image of RGO aerogel showing the fiber-like PVA bridges RGO sheets. (h) Digital photographs of a compressed PVA/GAs showing the recovering process) (Ye et al., 2017; Zhi et al., 2021).

Chen et al. (2018) reported small organic molecule of cysteamine as covalent cross-linker to fabricate GAs. Because of strong covalent cross-linking between the GO nanosheets through cysteamine as the linkage, the porosity and mechanical stability of GAs were both enhanced. In addition, the remaining hydrophilic region, which retains water as a spacer, produced

mesopores and macropores, which caused the planes to self-assemble into a 3D structure (Chen *et al.,* 2018; Zhi *et al.,* 2021).

1.8 The aims of research

In combination with a solid network and nanosized air pores, the special optical, thermal and acoustic mechanical characteristics of an aerogel arise. Choosing precursors and optimising sol-gel parameters will deduce the physical characteristics of the final aerogel product. Drying the gels is achieved in conjunction with the industrial aerogel procedure with supercritical or ambient pressure drying methods. Drying techniques at ambient pressure can likely make industrial preparation much cheaper so that aerogels become more efficient. Therefore, in an approach to lower the manufacture cost and decrease the used chemical waste of ambient pressure drying method, a novel attempt has been enhanced by Xiao Han and Lidija Siller in our nanoscale science and nanotechnology group at Newcastle University. Nevertheless, the mechanical properties of silica aerogels which are synthesized by this novel method need to be developed.

This PhD study is aiming to provide the following goals:

Graphene oxide reinforced silica aerogels

To improve the mechanical and physical properties of silica aerogels, GO as a nano additive was incorporated with the silica aerogel. Investigation of GO embedded in the silica matrix to identify the potential of carbon-based materials when used as a nanofiller for silica aerogels is one of the main purposes of this part of the thesis. Additionally, the influence of GO on the properties of silica aerogel composites was analysed.

Production of reduced graphene oxide aerogels using ambient pressure and supercritical drying methods

Graphene has been widely studied for electronics, sensors, actuators, catalytic devices and systems related to bio- or energy. In this context, graphene materials should normally be manufactured or assembled into desired electrical, optical, mechanical, chemical and electrochemical nano-architectures to be tested. Thus, in the studies of three-dimensional (3D), graphene has attracted a great attention. In this study, reduced graphene oxide aerogels were produced using ambient pressure and supercritical drying method. Drying techniques were compared. Furthermore, properties and application areas were discussed.

Synthesis of reduced graphene oxide aerogels doped with different metal oxide nanoparticles

A simple method for obtaining rGO aerogels doped with different metal oxide nanoparticles, GeO_2, ZnO, $CoFe_2O_4$, and Fe_3O_4 using supercritical drying method is discussed in the following chapter. Main objective of this study is analyzing physical properties such as surface area,

morphology, the chemical composition and electrochemical measurements as an anode material for LIBs.

Reduced graphene oxide aerogels by using ambient pressure drying method

A simple chemical reduction method was used for the synthesis of 3-D graphene aerogel with sodium bisulfite as the reducing agent. This work is mentioned in chapter 5. The aim of this work is to obtain ambient pressure dried graphene aerogel for large scale and low-cost industrial products using ordinary devices with freeze-thaw process.

1.9 Conclusion

Chapter 1 explained the different techniques utilised to produce aerogel in addition to potential applications of silica aerogels by the sol gel method. This chapter also gave information on the main drying techniques which are supercritical drying, freeze drying and ambient pressure drying to synthesize aerogels. Moreover, the lately sodium bicarbonate based ambient pressure drying method which was improved by Han and Siller (2015) to produce silica aerogels from TEOS precursor were mentioned. Furthermore, this chapter pointed out some promising applications of aerogels. Lastly, this review outlined the objectives and purposes of the study exhibited in the next chapters of this PhD thesis.

References

Abolghasemi Mahani, A., Motahari, S. and Mohebbi, A., 2018. Sol-gel derived flexible silica aerogel as selective adsorbent for water decontamination from crude oil. *Marine Pollution Bulletin*, 129(2), pp.438-447.

Akimov, Y., 2003. Journal search results. *Instruments and Experimental Techniques*, 46(3), pp.287-299.

Alié, C., Pirard, R., Lecloux, A. and Pirard, J., 1999. Preparation of low-density xerogels through additives to TEOS-based alcogels. *Journal of Non-Crystalline Solids*, 246(3), pp.216-228.

Al Soubaihi, R., Saoud, K., Ye, F., Zar Myint, M., Saeed, S., and Dutta, J. (2020) Synthesis of hierarchically porous silica aerogel supported Palladium catalyst for low-temperature CO oxidation under ignition/extinction conditions. *Microporous and Mesoporous Materials*, 292, p. 109758.

Baetens, R., Jelle, B., Thue, J., Tenpierik, M., Grynning, S., Uvsløkk, S. and Gustavsen, A., 2010. Vacuum insulation panels for building applications: A review and beyond. *Energy and Buildings*, 42(2), pp.147-172.

Balaji, N., Mani, M. and Reddy, B., 2014. Discerning Heat Transfer in Building Materials. *Energy Procedia*, 54, pp.654-668.

Bhaduri, S., 1993. THE PHYSICS AND CHEMISTRY OF SOL-GEL PROCESSING edited by C.J. Brinker and G.W. Scherer Academic Press, Inc., San Diego, CA 908 pages, hard cover, 1990. *Materials and Manufacturing Processes*, 8(3), pp.391-392.

Bisson, A., Rigacci, A., Lecomte, D., Rodier, E. and Achard, P., 2003. Drying of Silica Gels to Obtain Aerogels:Phenomenology and Basic Techniques. *Drying Technology*, 21(4), pp.593-628.

Boday, D., Keng, P., Muriithi, B., Pyun, J. and Loy, D., 2010. Mechanically reinforced silica aerogel nanocomposites via surface-initiated atom transfer radical polymerizations. *Journal of Materials Chemistry*, 20(33), p.6863.

Cai, H., Jiang, Y., Feng, J., Zhang, S., Peng, F., Xiao, Y., Li, L., and Feng, J. (2020) Preparation of silica aerogels with high temperature resistance and low thermal conductivity by monodispersed silica sol. *Materials & Design*, 191, p. 108640.

Cai, J., Liu, S., Feng, J., Kimura, S., Wada, M., Kuga, S. and Zhang, L., 2012. Cellulose-Silica Nanocomposite Aerogels by In Situ Formation of Silica in Cellulose Gel. *Angewandte Chemie International Edition*, 51(9), pp.2076-2079.

Capadona, L., Meador, M., Alunni, A., Fabrizio, E., Vassilaras, P. and Leventis, N., 2006. Flexible, low-density polymer crosslinked silica aerogels. *Polymer*, 47(16), pp.5754-5761.

Caponi, S., Carini, G., D'Angelo, G., Fontana, A., Pilla, O., Rossi, F., Terki, F., Tripodo, G., and Woignier, T. (2004) Acoustic and thermal properties of silica aerogels and xerogels. *Physical Review B*, 70(21).

Carraher, C., 2005. COLUMNS: General Topics. *Polymer News*, 30(2), pp.62-64.

Chakraborty, S., Pisal, A., Kothari, V. and Venkateswara Rao, A., 2017. Corrigendum to "Synthesis and Characterization of Fibre Reinforced Silica Aerogel Blankets for Thermal Protection". *Advances in Materials Science and Engineering*, 2017, pp.1-1.

Chen, Z., Xu, C., Ma, C., Ren, W. and Cheng, H., 2013. Lightweight and Flexible Graphene Foam Composites for High-Performance Electromagnetic Interference Shielding. *Advanced Materials*, 25(9), pp.1296-1300.

Compton, O. and Nguyen, S., 2010. Graphene Oxide, Highly Reduced Graphene Oxide, and Graphene: Versatile Building Blocks for Carbon-Based Materials. *Small*, 6(6), pp.711-723.

Cui, W., Pi, M., Li, Y., Shi, L. and Ran, R., 2020. Multimechanism Physical Cross-Linking Results in Tough and Self-Healing Hydrogels for Various Applications. *ACS Applied Polymer Materials*, 2(8), pp.3378-3389.

Danks, A., Hall, S. and Schnepp, Z., 2016. The evolution of 'sol–gel' chemistry as a technique for materials synthesis. *Materials Horizons*, 3(2), pp.91-112.

Davis, P., Deshpande, R., Smith, D., Brinker, C. and Assink, R., 1994. Pore structure evolution in silica gel during aging/drying. IV. Varying pore fluid pH. *Journal of Non-Crystalline Solids*, 167(3), pp.295-306.

Davis, P., Jeffrey Brinker, C. and Smith, D., 1992. Pore structure evolution in silica gel during aging/drying I. Temporal and thermal aging. *Journal of Non-Crystalline Solids*, 142, pp.189-196.

Dervin, S., Lang, Y., Perova, T., Hinder, S. and Pillai, S., 2017. Graphene oxide reinforced high surface area silica aerogels. *Journal of Non-Crystalline Solids*, 465, pp.31-38.

Dvornic, P. and Owen, M., 2009. *Silicon-Containing Dendritic Polymers*. [Dordrecht]: Springer.

Ebelmen, M., 1846. Recherches sur les combinaisons des acides borique et silicique avec les e ´thers. *Ann Chim Phys,* 16, pp.129–166.

Einarsrud, M., Nilsen, E., Rigacci, A., Pajonk, G., Buathier, S., Valette, D., Durant, M., Chevalier, B., Nitz, P. and Ehrburger-Dolle, F., 2001. Strengthening of silica gels and aerogels by washing and aging processes. *Journal of Non-Crystalline Solids*, 285(1-3), pp.1-7.

Fragiadakis, D. and Pissis, P., 2007. Glass transition and segmental dynamics in poly(dimethylsiloxane)/silica nanocomposites studied by various techniques. *Journal of Non-Crystalline Solids*, 353(47-51), pp.4344-4352.

Fragiadakis, D., Pissis, P. and Bokobza, L., 2006. Modified chain dynamics in poly(dimethylsiloxane)/silica nanocomposites. *Journal of Non-Crystalline Solids*, 352(42-49), pp.4969-4972.

Fricke, J. and Emmerling, A., 2010. Chem Inform Abstract: Aerogels. *ChemInform*, 23(44), p.no-no.

Fu, S., Sun, Z., Huang, P., Li, Y. and Hu, N., 2019. Some basic aspects of polymer nanocomposites: A critical review. *Nano Materials Science*, 1(1), pp.2-30.

Guise, M., Hosticka, B., Earp, B. and Norris, P., 2001. An experimental investigation of aerosol collection utilizing packed beds of silica aerogel microspheres. *Journal of Non-Crystalline Solids*, 285(1-3), pp.317-322.

Gurav, J., Jung, I., Park, H., Kang, E. and Nadargi, D., 2010. Silica Aerogel: Synthesis and Applications. *Journal of Nanomaterials*, 2010, pp.1-11.

Gurav, J., Jung, I., Park, H., Kang, E. and Nadargi, D., 2010. Silica Aerogel: Synthesis and Applications. *Journal of Nanomaterials*, 2010, pp.1-11.

Gurav, J., Jung, I., Park, H., Kang, E. and Nadargi, D., 2020. *Silica Aerogel: Synthesis and Applications*.

Hagemans, F., Pujala, R., Hotie, D., Thies-Weesie, D., de Winter, D., Meeldijk, J., van Blaaderen, A., and Imhof, A. (2018) Shaping Silica Rods by Tuning Hydrolysis and Condensation of Silica Precursors. *Chemistry of Materials*, 31(2), pp. 521-531.

Hamann, T., Martinson, A., Elam, J., Pellin, M. and Hupp, J., 2008. Atomic Layer Deposition of TiO2 on Aerogel Templates: New Photoanodes for Dye-Sensitized Solar Cells. *The Journal of Physical Chemistry C*, 112(27), pp.10303-10307.

Han, X. and Siller, L. (2015) 'Aerogel synthesis', P221149GB/DW (WO2016132117 A1).

Han, X., Hassan, K., Harvey, A., Kulijer, D., Oila, A., Hunt, M. and Šiller, L., 2018. Bioinspired Synthesis of Monolithic and Layered Aerogels. *Advanced Materials*, 30(23), p.1706294.

Harreld, J., Ebina, T., Tsubo, N. and Stucky, G., 2002. Manipulation of pore size distributions in silica and ormosil gels dried under ambient pressure conditions. *Journal of Non-Crystalline Solids*, 298(2-3), pp.241-251.

Hegde, N. and Venkateswara Rao, A., 2007. Physical properties of methyltrimethoxysilane based elastic silica aerogels prepared by the two-stage sol–gel process. *Journal of Materials Science*, 42(16), pp.6965-6971.

Heinrich, T., Klett, U. and Fricke, J., 1995. Aerogels-Nanoporous materials part I: Sol-gel process and drying of gels. *Journal of Porous Materials*, 1(1), pp.7-17.

Hench, L. and Ulrich, D., 1986. *Science of Ceramic Chemical Processing*. Chichester: Wiley-Interscience.

Hench, L. and West, J., 1990. ChemInform Abstract: The Sol-Gel Process. *ChemInform*, 21(25).

Hong, J., Bak, B., Wie, J., Kong, J. and Park, H., 2015. Energy Storage: Reversibly Compressible, Highly Elastic, and Durable Graphene Aerogels for Energy Storage Devices under Limiting Conditions (Adv. Funct. Mater. 7/2015). *Advanced Functional Materials*, 25(7), pp.1159-1159.

Hrubesh, L., 2010. ChemInform Abstract: Aerogels: The World′s Lightest Solids. *ChemInform*, 22(13), p.no-no.

Hrubesh, L., Coronado, P. and Satcher, J., 2001. Solvent removal from water with hydrophobic aerogels. *Journal of Non-Crystalline Solids*, 285(1-3), pp.328-332.

Hüsing, N. and U. Schubert., 2000. Aerogels, in Ullmann's Encyclopedia of Industrial Chemistry. *Wiley-VCH Verlag GmbH & Co. KGaA.*

Hwang, S., Jung, H., Hyun, S. and Ahn, Y., 2007. Effective preparation of crack-free silica aerogels via ambient drying. *Journal of Sol-Gel Science and Technology*, 41(2), pp.139-146.

Issa, A. and Luyt, A., 2019. Kinetics of Alkoxysilanes and Organoalkoxysilanes Polymerization: A Review. *Polymers*, 11(3), p.537.

Kalinin, S., Kheifets, L., Mamchik, A., Knot'ko, A. and Vertigel, A., 1999. Journal search results - Cite This For Me. *Journal of Sol-Gel Science and Technology*, 15(1), pp.31-35.

Kanamori, K., Aizawa, M., Nakanishi, K. and Hanada, T., 2007. New Transparent Methylsilsesquioxane Aerogels and Xerogels with Improved Mechanical Properties. *Advanced Materials*, 19(12), pp.1589-1593.

Kauffman, G., 2000. Ullmann?s Encyclopedia of Industrial Chemistry Fifth Edition, First International Edition in English by Wolfgang Gehartz, Gail Schulz Thomas Kellersohn, Barbara Elvers, Stephen Hawkins, and Ulrike Winter (Eds.). *The Chemical Educator*, 5(1), pp.49-53.

Kéri, M., Forgács, A., Papp, V., Bányai, I., Veres, P., Len, A., Dudás, Z., Fábián, I. and Kalmár, J. (2020). Gelatin content governs hydration induced structural changes in silica-gelatin hybrid aerogels – Implications in drug delivery. *Acta Biomaterialia*, 105, pp.131–145.

Kistler, S. and Caldwell, A., 1934. Thermal Conductivity of Silica Aërogel. *Industrial & Engineering Chemistry*, 26(6), pp.658-662.

Kistler, S., 1931. Coherent Expanded Aerogels and Jellies. *Nature*, 127(3211), pp.741-741.

Kistler, S., 1932. Coherent Expanded-Aerogels. *The Journal of Physical Chemistry*, 36(1), pp.52-64.

Kistler, S., 1935. The Relation between Heat Conductivity and Structure in Silica Aerogel. *The Journal of Physical Chemistry*, 39(1), pp.79-86.

Korkmaz, S. and Kariper, İ., 2020. Graphene and graphene oxide based aerogels: Synthesis, characteristics and supercapacitor applications. *Journal of Energy Storage*, 27, p.101038.

Kotal, M., Kim, H., Roy, S. and Oh, I., 2017. Sulfur and nitrogen co-doped holey graphene aerogel for structurally resilient solid-state supercapacitors under high compressions. *Journal of Materials Chemistry A*, 5(33), pp.17253-17266.

Kramer, S., Rubio-Alonso, F. and Mackenzie, J., 1996. Organically Modified Silicate Aerogels, "Aeromosils". *MRS Proceedings*, 435.

Lamy-Mendes, A., Silva, R. and Durães, L., 2018. Advances in carbon nanostructure–silica aerogel composites: a review. *Journal of Materials Chemistry A*, 6(4), pp.1340-1369.

Lee, CJ., Kim, GS., Hyun, SH., 2002. Synthesis of silica aerogels from water-glass via new modified ambient drying. *J Mater Sci,* 3(7), pp.2237–2241.

Lee, O., Lee, K., Jin Yim, T., Young Kim, S. and Yoo, K., 2002. Determination of mesopore size of aerogels from thermal conductivity measurements. *Journal of Non-Crystalline Solids*, 298(2-3), pp.287-292.

Lei, Y., Hu, Z., Cao, B., Chen, X. and Song, H., 2017. Enhancements of thermal insulation and mechanical property of silica aerogel monoliths by mixing graphene oxide. *Materials Chemistry and Physics*, 187, pp.183-190.

Leventis, N., 2007. Three-Dimensional Core-Shell Superstructures: Mechanically Strong Aerogels. *ChemInform*, 38(51).

Leventis, N., 2007. Three-Dimensional Core-Shell Superstructures: Mechanically Strong Aerogels. *Accounts of Chemical Research*, 40(9), pp.874-884.

Leventis, N., Sadekar, A., Chandrasekaran, N. and Sotiriou-Leventis, C., 2010. Click Synthesis of Monolithic Silicon Carbide Aerogels from Polyacrylonitrile-Coated 3D Silica Networks. *Chemistry of Materials*, 22(9), pp.2790-2803.

Leventis, N., Sotiriou-Leventis, C., Zhang, G. and Rawashdeh, A., 2002. Nanoengineering Strong Silica Aerogels. *Nano Letters*, 2(9), pp.957-960.

Li, C., Li, Y., Zhao, Q., Luo, Y., Yang, G., Hu, Y. and Jiang, J., 2020. Electromagnetic Interference Shielding of Graphene Aerogel with Layered Microstructure Fabricated via Mechanical Compression. *ACS Applied Materials & Interfaces*, 12(27), pp.30686-30694.

Li, L., Yalcin, B., Nguyen, B., Meador, M. and Cakmak, M., 2009. Flexible Nanofiber-Reinforced Aerogel (Xerogel) Synthesis, Manufacture, and Characterization. *ACS Applied Materials & Interfaces*, 1(11), pp.2491-2501.

Li, T., Zhi, D., Chen, Y., Li, B., Zhou, Z. and Meng, F., 2020. Multiaxial electrospun generation of hollow graphene aerogel spheres for broadband high-performance microwave absorption. *Nano Research*, 13(2), pp.477-484.

Livage, J., Henry, M. and Sanchez, C., 1988. Sol-gel chemistry of transition metal oxides. *Progress in Solid State Chemistry*, 18(4), pp.259-341.

Lucas, E., Doescher, M., Ebenstein, D., Wahl, K. and Rolison, D., 2004. Silica aerogels with enhanced durability, 30-nm mean pore-size, and improved immersibility in liquids. *Journal of Non-Crystalline Solids*, 350, pp.244-252.

Maleki, H., Durães, L., and Portugal, A. (2014) An overview on silica aerogels synthesis and different mechanical reinforcing strategies. *Journal of Non-Crystalline Solids*, 385, pp. 55-74.

Maleki, H., 2016. Recent advances in aerogels for environmental remediation applications: A review. *Chemical Engineering Journal*, 300, pp.98-118.

Mandal, C., Donthula, S., Rewatkar, P., Sotiriou-Leventis, C. and Leventis, N., 2019. Experimental deconvolution of depressurization from capillary shrinkage during drying of silica wet-gels with SCF CO2 why aerogels shrink? *Journal of Sol-Gel Science and Technology*, 92(3), pp.662-680.

Maximiano, P., Durães, L., and Simões, P. (2019) Organically-modified silica aerogels: A density functional theory study. *The Journal of Supercritical Fluids*, 147, pp. 138-148.

Meador, M., Capadona, L., McCorkle, L., Papadopoulos, D. and Leventis, N., 2007. Structure−Property Relationships in Porous 3D Nanostructures as a Function of Preparation Conditions: Isocyanate Cross-Linked Silica Aerogels. *Chemistry of Materials*, 19(9), pp.2247-2260.

Meador, M., Fabrizio, E., Ilhan, F., Dass, A., Zhang, G., Vassilaras, P., Johnston, J. and Leventis, N., 2005. Cross-linking Amine-Modified Silica Aerogels with Epoxies: Mechanically Strong Lightweight Porous Materials. *Chemistry of Materials*, 17(5), pp.1085-1098.

Moon, I., Yoon, S., Chun, K. and Oh, J., 2015. Aerogels: Highly Elastic and Conductive N-Doped Monolithic Graphene Aerogels for Multifunctional Applications (Adv. Funct. Mater. 45/2015). *Advanced Functional Materials*, 25(45), pp.6954-6954.

Nadargi, D., Latthe, S. and Venkateswara Rao, A., 2008. Effect of post-treatment (gel aging) on the properties of methyltrimethoxysilane based silica aerogels prepared by two-step sol–gel process. *Journal of Sol-Gel Science and Technology*, 49(1), pp.53-59.

Nakanishi, K., Minakuchi, H., Soga, N., Tanaka, N., 1998. Structure Design of Double-Pore Silica and Its Application to HPLC. J *Sol Gel Sci Technol*, 1(3), pp.163–169

Ochoa, M., Durães, L., Beja, A. and Portugal, A., 2012. Study of the suitability of silica based xerogels synthesized using ethyltrimethoxysilane and/or methyltrimethoxysilane precursors for aerospace applications. *Journal of Sol-Gel Science and Technology*, 61(1), pp.151-160.

Otterstedt, J. and Brandreth, D., 1998. *Small Particles Technology*. Boston, MA: Springer US.

Pajonk, G., Repellin-Lacroix, M., Abouarnadasse, S., Chaouki, J. and Klavana, D., 1990. From sol-gel to aerogels and cryogels. *Journal of Non-Crystalline Solids*, 121(1-3), pp.66-67.

Pandey, S. and Mishra, S., 2011. Sol–gel derived organic–inorganic hybrid materials: synthesis, characterizations and applications. *Journal of Sol-Gel Science and Technology*, 59(1), pp.73-94.

Parale, V., Lee, K., Jung, H., Nah, H., Choi, H., Kim, T., Phadtare, V. and Park, H., 2018. Facile synthesis of hydrophobic, thermally stable, and insulative organically modified silica aerogels using co-precursor method. *Ceramics International*, 44(4), pp.3966-3972.

Parale, V., Mahadik, D., Kavale, M., Rao, A., Wagh, P. and Gupta, S., 2011. Potential Application of Silica Aerogel Granules for Cleanup of Accidental Spillage of Various Organic Liquids. *Soft Nanoscience Letters*, 01(04), pp.97-104.

Paraskevopoulou, P., Chriti, D., Raptopoulos, G. and Anyfantis, G., 2019. Synthetic Polymer Aerogels in Particulate Form. *Materials*, 12(9), p.1543.

Patil, S., 2019. Nanoindentation of Graphene-Reinforced Silica Aerogel: A Molecular Dynamics Study. *Molecules*, 24(7), p.1336.

Pierre, A., 1998. *Introduction To Sol-Gel Processing*. Boston: Kluwer Academic Publishers.

Podsiadlo, P., Kaushik, A., Arruda, E., Waas, A., Shim, B., Xu, J., Nandivada, H., Pumplin, B., Lahann, J., Ramamoorthy, A. and Kotov, N., 2007. Ultrastrong and Stiff Layered Polymer Nanocomposites. *Science*, 318(5847), pp.80-83.

Posada, L., Carroll, M., Anderson, A., and Bruno, B. (2019) Inclusion of Ceria in Alumina- and Silica-Based Aerogels for Catalytic Applications. *The Journal of Supercritical Fluids*, 152, p. 104536.

Raman, N., Sudharsan, S. and Pothiraj, K., 2012. Synthesis and structural reactivity of inorganic–organic hybrid nanocomposites – A review. *Journal of Saudi Chemical Society*, 16(4), pp.339-352.

Randall, J., Meador, M. and Jana, S., 2011. Tailoring Mechanical Properties of Aerogels for Aerospace Applications. *ACS Applied Materials & Interfaces*, 3(3), pp.613-626.

Reichenauer, G., 2004. Thermal aging of silica gels in water. *Journal of Non-Crystalline Solids*, 350, pp.189-195.

Rodríguez, S. and Colón, L., 1999. Investigations of a sol–gel derived stationary phase for open tubular capillary electrochromatography. *Analytica Chimica Acta*, 397(1-3), pp.207-215.

Rowlinson, J. and Widom, B., 2013. *Molecular Theory Of Capillarity*. Newburyport: Dover Publications.

Salimian, S., Zadhoush, A., Naeimirad, M., Kotek, R. and Ramakrishna, S., 2017. A review on aerogel: 3D nanoporous structured fillers in polymer-based nanocomposites. *Polymer Composites*, 39(10), pp.3383-3408.

Sanchez, C., Belleville, P., Popall, M. and Nicole, L., 2011. Applications of advanced hybrid organic–inorganic nanomaterials: from laboratory to market. *Chemical Society Reviews*, 40(2), p.696.

Shang, Y., Yang, H., Qin, Z., Yin, S., Yang, L., Xu, M., Li, Z., Jin, Z. and Sun, H., 2020. Arbitrary-shaped reduced graphene oxide aerogels via an unsaturated water vapor reduction. *Carbon*, 168, pp.169-179.

Shu, R., Wan, Z., Zhang, J., Wu, Y., Liu, Y., Shi, J. and Zheng, M., 2019. Facile Design of Three-Dimensional Nitrogen-Doped Reduced Graphene Oxide/Multi-Walled Carbon Nanotube Composite Foams as Lightweight and Highly Efficient Microwave Absorbers. *ACS Applied Materials & Interfaces*, 12(4), pp.4689-4698.

Soleimani Dorcheh, A. and Abbasi, M., 2008. Silica aerogel; synthesis, properties and characterization. *Journal of Materials Processing Technology*, 199(1-3), pp.10-26.

Stojanovic, A., Zhao, S., Angelica, E., Malfait, W., and Koebel, M. (2019) Three routes to superinsulating silica aerogel powder. *Journal of Sol-Gel Science and Technology*, 90(1), pp. 57-66.

Suib, S., 2013. *New And Future Developments In Catalysis*. Amsterdam: Elsevier Ltd.

Sun, H., Xu, Z. and Gao, C., 2013. Multifunctional, Ultra-Flyweight, Synergistically Assembled Carbon Aerogels. *Advanced Materials*, 25(18), pp.2554-2560.

Tang, F., Jiang, T., Tan, Y., Xu, X. and Zhou, Y., 2021. Preparation and electrochemical performance of silicon@graphene aerogel composites for lithium-ion batteries. *Journal of Alloys and Compounds*, 854, p.157135.

Tang, J., Liang, N., Wang, L., Li, J., Tian, G., Zhang, D., Feng, S. and Yue, H., 2019. Three-dimensional nitrogen-doped reduced graphene oxide aerogel decorated with Ni nanoparticles with tunable and unique microwave absorption. *Carbon*, 152, pp.575-586.

Thakkar, S., Pinna, A., Carbonaro, C., Malfatti, L., Guardia, P., Cabot, A. and Casula, M., 2020. Performance of oil sorbents based on reduced graphene oxide–silica composite aerogels. *Journal of Environmental Chemical Engineering*, 8(1), p.103632.

Thapliyal, P. and Singh, K., 2014. Aerogels as Promising Thermal Insulating Materials: An Overview. *Journal of Materials*, 2014, pp.1-10.

Tiwari, I. and Mahanwar, P., 2018. Polyacrylate/silica hybrid materials: A step towards multifunctional properties. *Journal of Dispersion Science and Technology*, 40(7), pp.925-957.

Tiwari, S., Sahoo, S., Wang, N. and Huczko, A., 2020. Graphene research and their outputs: Status and prospect. *Journal of Science: Advanced Materials and Devices*, 5(1), pp.10-29.

Tobin, Z., Posada, L., Bechu, A., Carroll, M., Bouck, R., Anderson, A. and Bruno, B., 2017. Preparation and characterization of copper-containing alumina and silica aerogels for catalytic applications. *Journal of Sol-Gel Science and Technology*, 84(3), pp.432-445.

Tong, Y., He, M., Zhou, Y., Nie, S., Zhong, X., Fan, L., Huang, T., Liao, Q. and Wang, Y., 2018. Three-Dimensional Hierarchical Architecture of the TiO2/Ti3C2Tx/RGO Ternary Composite Aerogel for Enhanced Electromagnetic Wave Absorption. *ACS Sustainable Chemistry & Engineering*, 6(7), pp.8212-8222.

Venkateswara Rao, A. and Haranath, D., 1999. Effect of methyltrimethoxysilane as a synthesis component on the hydrophobicity and some physical properties of silica aerogels. *Microporous and Mesoporous Materials*, 30(2-3), pp.267-273.

Venkateswara Rao, A., Parvathy Rao, A. and Kulkarni, M., 2004. Influence of gel aging and Na_2SiO_3/H_2O molar ratio on monolithicity and physical properties of water–glass-based aerogels dried at atmospheric pressure. *Journal of Non-Crystalline Solids*, 350, pp.224-229.

Venkateswara Rao, A., Bhagat, S., Hirashima, H. and Pajonk, G., 2006. Synthesis of flexible silica aerogels using methyltrimethoxysilane (MTMS) precursor. *Journal of Colloid and Interface Science*, 300(1), pp.279-285.

Veronovski, A., Novak, Z. and Željko, K., 2011. Organic Biodegradable Aerogels Used in Controlled Drug Release. *MRS Proceedings*, 1306.

Vieira, K., Panzera, T., Ferrari, J. and Schiavon, M., 2018. Nanocomposites Based on Polyelectrolytes-Multiwalled Carbon Nanotubes Coated with a Silica Shell. *Materials Research*, 21(6).

Wagh, P., Begag, R., Pajonk, G., Rao, A. and Haranath, D., 1999. Comparison of some physical properties of silica aerogel monoliths synthesized by different precursors. *Materials Chemistry and Physics*, 57(3), pp.214-218.

Wang, J., Shang, L., Cheng, Y., Ding, H., Zhao, Y. and Gu, Z., 2015. Microfluidic Generation of Porous Particles Encapsulating Spongy Graphene for Oil Absorption. *Small*, 11(32), pp.3890-3895.

Wang, L., Feng, J., Jiang, Y., Li, L., and Feng, J. (2019) Elastic methyltrimethoxysilane based silica aerogels reinforced with polyvinylmethyldimethoxysilane. *RSC Advances*, 9(19), pp. 10948-10957.

Wang, W., Motuzas, J., Zhao, X., and Diniz da Costa, J. (2019) 2D/3D amine functionalised sorbents containing graphene silica aerogel and mesoporous silica with improved CO2 sorption. *Separation and Purification Technology*, 222, pp. 381-389.

Xu, D., Yang, S., Chen, P., Yu, Q., Xiong, X. and Wang, J., 2019. Synthesis of magnetic graphene aerogels for microwave absorption by in-situ pyrolysis. *Carbon*, 146, pp.301-312.

Ye, S., Liu, Y. and Feng, J., 2017. Low-Density, Mechanical Compressible, Water-Induced Self-Recoverable Graphene Aerogels for Water Treatment. *ACS Applied Materials & Interfaces*, 9(27), pp.22456-22464.

Yim, T., Kim, S. and Yoo, K., 2002. Fabrication and thermophysical characterization of nano-porous silica-polyurethane hybrid aerogel by sol-gel processing and supercritical solvent drying technique. *Korean Journal of Chemical Engineering*, 19(1), pp.159-166.

Yousefi Amiri, T., Moghaddas, J. and Rahmani Khajeh, S., 2015. Silica aerogel-supported copper catalyst prepared via ambient pressure drying process. *Journal of Sol-Gel Science and Technology*, 77(3), pp.627-635.

Yuan, B., Ding, S., Wang, D., Wang, G. and Li, H., 2012. Heat insulation properties of silica aerogel/glass fiber composites fabricated by press forming. *Materials Letters*, 75, pp.204-206.

Yue, C., Feng, J., Feng, J. and Jiang, Y., 2016. Low-thermal-conductivity nitrogen-doped graphene aerogels for thermal insulation. *RSC Advances*, 6(12), pp.9396-9401.

Zha, J. and Roggendorf, H., 1991. Sol-gel science, the physics and chemistry of sol-gel processing, Ed. by C. J. Brinker and G. W. Scherer, Academic Press, Boston 1990, xiv, 908 pp., bound?ISBN 0-12-134970-5. *Advanced Materials*, 3(10), pp.522-522.

Zhang, G., Dass, A., Rawashdeh, A., Thomas, J., Counsil, J., Sotiriou-Leventis, C., Fabrizio, E., Ilhan, F., Vassilaras, P., Scheiman, D., McCorkle, L., Palczer, A., Johnston, J., Meador, M. and Leventis, N., 2004. Isocyanate-crosslinked silica aerogel monoliths: preparation and characterization. *Journal of Non-Crystalline Solids*, 350, pp.152-164.

Zhang, Y., Huang, Y., Zhang, T., Chang, H., Xiao, P., Chen, H., Huang, Z. and Chen, Y., 2015. Broadband and Tunable High-Performance Microwave Absorption of an Ultralight and Highly Compressible Graphene Foam. *Advanced Materials*, 27(12), pp.2049-2053.

Zhao, C., Fan, J., Chen, D., Xu, Y. and Wang, T., 2016. Microfluidics-generated graphene oxide microspheres and their application to removal of perfluorooctane sulfonate from polluted water. *Nano Research*, 9(3), pp.866-875.

Zhang, C., Zhu, J., Cao, Z., Song, P. and Zhai, T., 2020. Flow-induced microchannel structure of the graphene-based aerogel microspheres and their use as superabsorbents. *Polymers for Advanced Technologies*, 31(11), pp.2789-2796.

Zhi, D., Li, T., Li, J., Ren, H. and Meng, F., 2021. A review of three-dimensional graphene-based aerogels: Synthesis, structure and application for microwave absorption. *Composites Part B: Engineering*, 211, p.108642.

Zhou, B., Shen, J., Wu, Y., Wu, G. and Ni, X., 2007. Hydrophobic silica aerogels derived from polyethoxydisiloxane and perfluoroalkylsilane. *Materials Science and Engineering: C*, 27(5-8), pp.1291-1294.

Zhu, C., Han, T., Duoss, E., Golobic, A., Kuntz, J., Spadaccini, C. and Worsley, M., 2015. Highly compressible 3D periodic graphene aerogel microlattices. *Nature Communications*, 6(1).

Zhuo, H., Hu, Y., Tong, X., Chen, Z., Zhong, L., Lai, H., Liu, L., Jing, S., Liu, Q., Liu, C., Peng, X. and Sun, R., 2018. A Supercompressible, Elastic, and Bendable Carbon Aerogel with Ultrasensitive Detection Limits for Compression Strain, Pressure, and Bending Angle. *Advanced Materials*, 30(18), p.1706705.

Zou, H., Wu, S. and Shen, J., 2008. Polymer/Silica Nanocomposites: Preparation, Characterization, Properties, and Applications. *Chemical Reviews*, 108(9), pp.3893-3957.

Zuo, L., Zhang, Y., Zhang, L., Miao, Y., Fan, W. and Liu, T., 2015. Polymer/Carbon-Based Hybrid Aerogels: Preparation, Properties and Applications. *Materials*, 8(10), pp.6806-6848.

Chapter 2 Synthesis methods to produce graphene oxide (GO) reinforced silica aerogels and characterization methods

This chapter outlines the experimental methods with the principles of operation of the techniques employed to study graphene oxide (GO) reinforced silica aerogels. Characterization of the morphology and microstructure of aerogels were analysed by using Scanning electron microscope (SEM). X-ray powder diffraction (XRD) is utilised to determine the structures of the produced aerogels. The Brunauer – Emmett – Teller (BET) method and the Barrett-Joyner-Halenda (BJH) method are used to describe specific surface area, pore volume and pore size distribution of aerogel materials. Uniaxial compression tests were used for the investigation of the mechanical properties of graphene oxide reinforced silica aerogel samples. Fourier transform infrared spectroscopy (FTIR) is used to investigate the chemical components of synthesized aerogels qualitatively and quantitatively. Lastly, Raman spectroscopy, which is a non-destructive chemical analysis technique, was applied to provide detailed information about chemical structure, phase and polymorphs, crystallinity, and molecular interactions within aerogels. In this chapter, principles of operation of all techniques are discussed in detail.

2.1 Materials and Methods

2.1.1 Synthesis of waterglass based silica aerogels with graphene oxide

Natural graphite flakes (99.8% purity) and sulphuric acid (98%) were purchased from VWR. Phosphoric acid (85%), dihydrogen dioxide (35%), potassium permanganate (99%), chlorotrimethylsilane (≥99%), hydrochloric acid (37%), and sodium silicate solution were purchased from Sigma. All reagents were used without further purification. Deionised (DI) water (18 MΩ/cm resistivity) from Nanopore purification system was used in all the experiments.

2.1.1a Synthesis of graphene oxide (GO)

GO was generated with oxidation and exfoliation of graphite with strong oxidants and mixed acids using Hummers method (Hummers and Offeman, 1958), revised in our laboratory by Wang et al., (2017). All the steps were done as explained in the paper from Wang et al., (2017), firstly, phosphoric acid (85%, 10ml) was added to sulphuric acid (98%, 50 ml) at room temperature by using magnetic stirrer. Then graphite (1.5 g) and potassium permanganate (4.08 g) were added to the solution. After three days, dihydrogen dioxide was put in the solution to cease reaction in which case the solution's colour turned into bright yellow. This solution was put in membrane, first washed with 5 % hydrogen chloride (200 ml) and then washed with DI

water to reach the pH 7. Lastly, it was dried at 70ºC in ordinary oven to produce graphene oxide sheets (Wang, Salihi and Šiller, 2017).

2.1.1.b Preparation of solutions

To make the silica precursor solution, the silicon source which was 6ml water glass (sodium silicate, 338443 Sigma Aldrich: Na2O~10.6%, SiO2~26.5%) and 30 ml distilled water were mixed. The molar ratio of the water glass and distilled water was 1:5. Three different solutions which have different amount of graphene oxide sheets (12 ml DI water and 22, 44 and 89 mg GO sheets) were prepared by mixing with ultrasonic probe for 15 min to make GO solutions. Graphene oxide weight percentages were 0.05, 0.1 and 0.2 wt% in silica aerogel composites.

2.1.1.c Synthesisation of SiO_2 and Si-GO wet gel

Sol gel technique is carried out to make silica gels with hydrolysis of water glass in distilled water. Firstly, 5 ml HCl (5M) was added to SiO_2 solution as a catalyst to turn sol into gel in 8 min. First day, it was washed with water then sodium bicarbonate solution was used as a solvent exchange. After using TMCS for carbon dioxide generation, the gel was washed by distilled water again to remove NaCl which came from the reaction between TMCS and $NaHCO_3$ (Han and Siller, 2015; Han *et al.,* 2018). The fourth day, water was replaced with ethanol. Finally, the gel was dried on the heater at 70°C for 24h. The prepared monolithic pure silica aerogel was ready to characterization. Fig. 2.1 shows the preparation of monolithic silica aerogels.

Firstly, two beakers were prepared because GO sheets were carried out using ultrasound treatment for homogeneous dispersion in water. One of them included GO solution (12ml distilled water+GO), the other one had 6 ml water glass as a silica precursor and 18 ml distilled water. First beaker was added into the second beaker and resulting 6 ml water glass, 30 ml water and GO (0.05wt%, 0.1wt%, 0.2wt%) stirred in sonication bath for 30 mins. Then the solution was left for one day to form sol. Next day, the addition of HCI turned the sol into gel. The remaining processes to produce final Si/GO composite aerogels were the same with the production of monolithic pure silica aerogel.

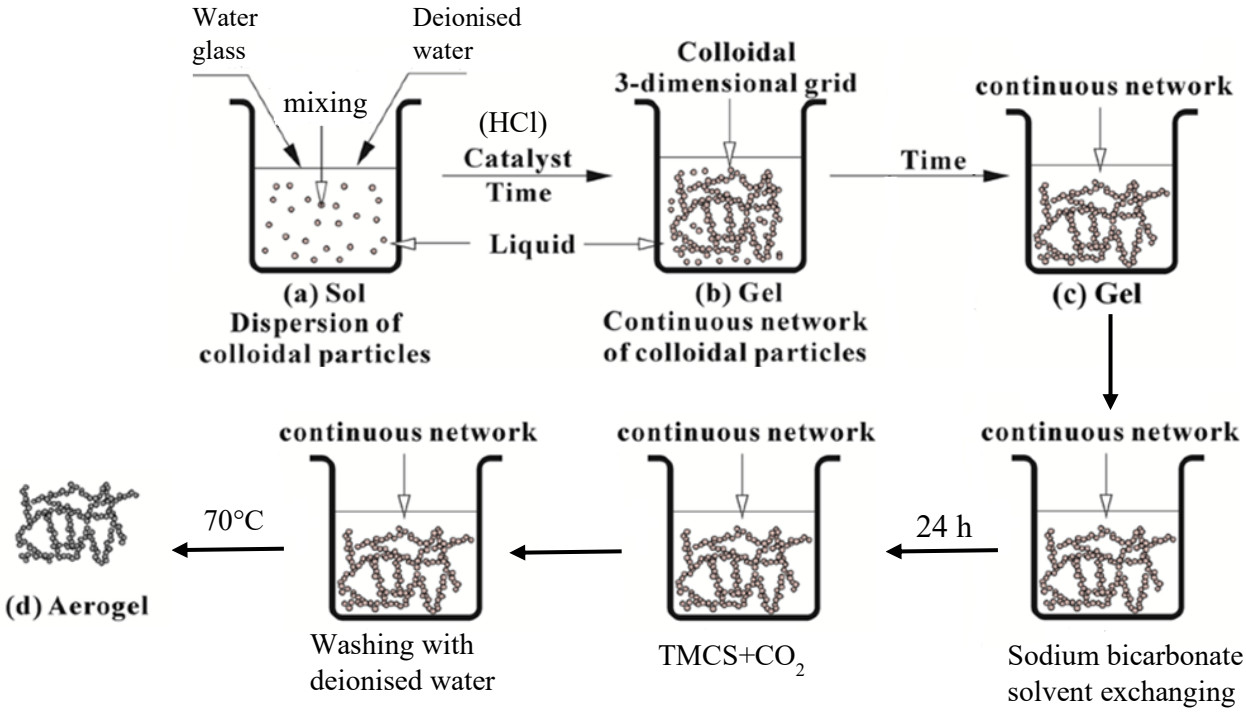

Figure 2. 1 Schematic diagram of silica aerogels

In addition to these aerogels, sodium silica aerogel without using novel ambient pressure drying method was produced to show how the novel APD technique effect the surface area, pore distribution and pore volume. Except using TMCS and sodium bicarbonate solution, other processes were the same as the synthesisation of monolithic pure silica aerogel through utilised novel ambient pressure drying method.

2.2 Characterization techniques

2.2.1 Scanning electron microscopy (SEM)

One of the most significant technological innovations of the twentieth century is scanning electron microscope (SEM). SEM increases the resolution of the light microscope by two different magnitudes. SEM was enhanced through a high-energy electron beam, using the short wavelengths of electrons, that are focused through electromagnetic lenses on the sample. SEM can generate high-resolution images with a large depth of field. The interaction of the electron beam with the specimen produces different signals such as backscattered electrons (BSEs), secondary electron (SEs), and typically X-rays for insights into the morphology, phase, and chemistry of the materials.

Why electrons?

The wavelength of the sampling radiation determines mainly the resolution of the images taken through the system. The shorter the wavelength, the smaller features of the sample can be resolved. Therefore, the shorter wavelength of electrons in contrast to visible light enables them to improve resolution. Electrons are given off by various sources such as tungsten filament, field emission gun and solid-state crystal. After acceleration with electronic lenses alongside the evacuated column, they are turned into a focused beam that is scanned over a surface of interest**.** When primary electrons hit a specimen surface, there is a broad range of interactions producing different electrons and photons which can be gathered to form images or a chemical spectrum of specimen. The image resolution is greater than 1 nm in modern SEM systems (Padua and Wang, 2012).

Electron–target interaction:

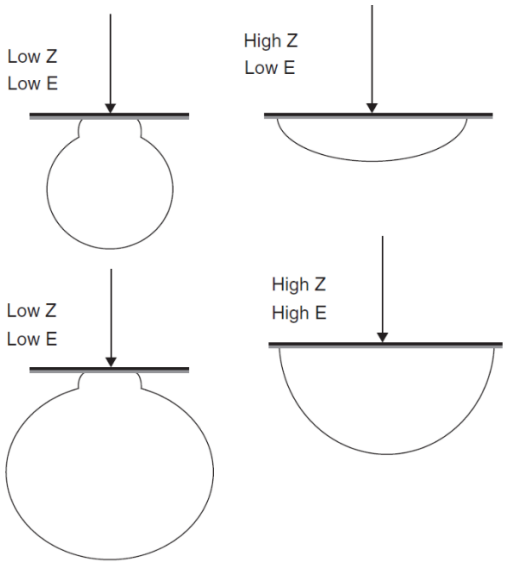

Figure 2. 2 Volumes of excitations at various atomic (Z) numbers and beam (E) energies (Padua and Wang, 2012).

SEM images rely on the signals obtained from the electron beam and sample interaction. Two types of interaction, elastic and inelastic electron scattering are known. Elastic scattering results from the deflection of the incident electron when the atomic nucleus or outer shell electrons of the specimen is hit. Elastic scattering has a minimal energy loss all through the collision and the scattered electron has a wide-angle directional change. If the directional shift is greater than 90 °, the electrons become BSEs that provide an efficient imaging signal. In the inelastic electron scattering, considerable energy is transferred to the specimen from electron, which in turn may become scattered or leave the specimen as a SE in motion. When the atom is ionised, the SE is expelled out from the inner orbital when the outer shell electrons fill the resulting electron hole created by ionisation (primary electron emission). An X-raying photon or another

electron, so called an Auger electron, can be also emitted during the characteristic de-excitation energy process. Chemical information about the material is obtained through a spectroscopic analysis of the characteristic X-rays and Auger electrons (Lyman, 2013).

If a finely oriented electron beam reaches the specimen surface, the energetic electrons will penetrate inside the sample to encounter and collide with sample atoms at some depth. The interaction region from which several signals are generated is in the micrometre range. The form of the region of interaction is more shallow depth for small atomic number samples and a hemisphere for high atomic number samples which is illustrated in Figure 2.2 (Padua and Wang, 2012). The depth of the interaction volume is dependent on the energy of the incident beam, the incidence angle, and the sample composition. With an improvement of the intensity of the beam or a decrease in the atomic number of the specimens, the volume and depth of the interaction area can be improved because of higher number of atomic particles on the electron path (Lyman, 2013).

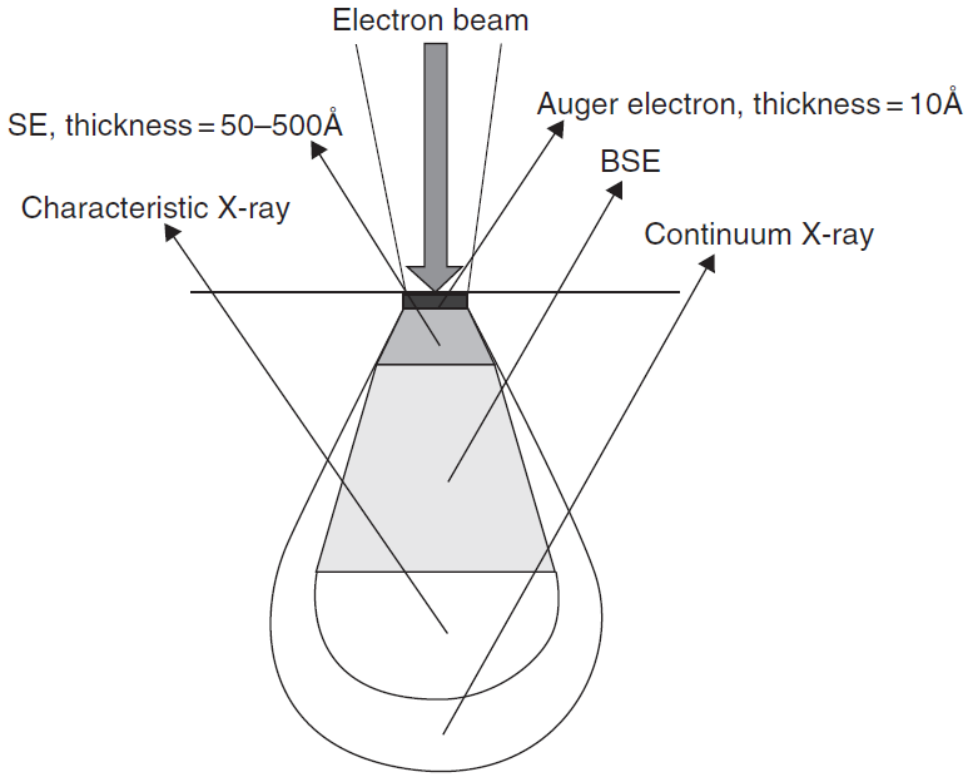

Figure 2. 3 Schematic representation of different interactions between electron and specimen (Padua and Wang, 2012).

The different elastic and inelastic electrons have various mean-free pathways in the sample, so they provide different signals, as shown in Figure 2.3 (Padua and Wang, 2012). Even if SEs and Auger electrons are released during the interaction volume, they have very small kinetic energies; therefore, they can only escape from a thin layer near the specimen surface. SEs or BSEs can be collected as an image to visually analyse the morphology of sample. X-ray or

Auger electron spectra are recorded to evaluate details about the chemical composition of the sample (Lyman, 2013).

Secondary electrons (SEs):

Secondary electrons arise from the sample's surface or near-surface regions. They occur as a result of inelastic interactions between the primary electron beam and the sample and have lower energy which is typically 1–10 eV with 50 eV being specified as the upper energy limit compared to the backscattered electrons. Secondary electrons are appropriate for evaluating the specimen's surface topography (Goldstein *et al.*, 2018).

In fact, many hundreds of secondary electrons can be excited inside the specimen by using a single primary electron; however, solely these which are excited inside ~10 nm of the surface can break out into the vacuum and be detected. Secondary electrons can therefore be subdivided into those which escape when the primary electrons are in the sample and those that are excited at the exit point if there is one. The primary-excited secondary electrons are generally able to give a higher resolution than the others (Mullerova and Konvalina, 2009).

Backscattered electrons (BSEs):

Some of the elastically scattered electrons are ultimately directed back from the specimen as backscattered electrons and compose a significant SEM imaging signal, rich in information on sample characteristics. The BSE signal provides details on the structure, topography, mass thickness and crystallography of the specimens (Goldstein *et al.*, 2018). Simulation by Monte Carlo can model these processes where incident electrons, after projecting onto the sample surface, lose energy within the sample or emitted back to the vacuum as backscattered electrons. Figure 2.4 is an example of Monte Carlo simulation where 100 electrons with kinetic energy of 15 kV are vertically incident onto the surface of an iron (Fe) sample (Novák, 2008).

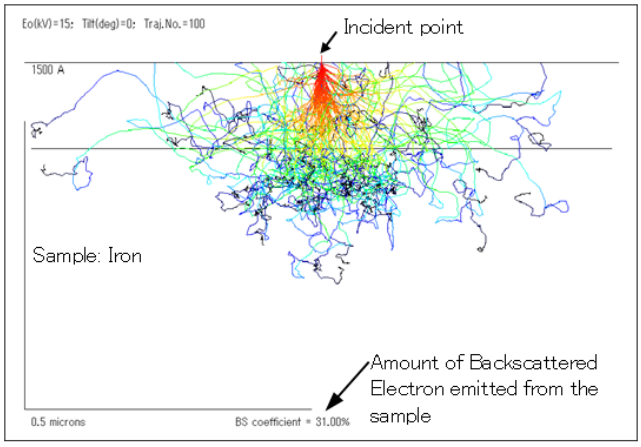

Figure 2. 4 Monto Carlo simulation of an Fe specimen (Novák, 2008).

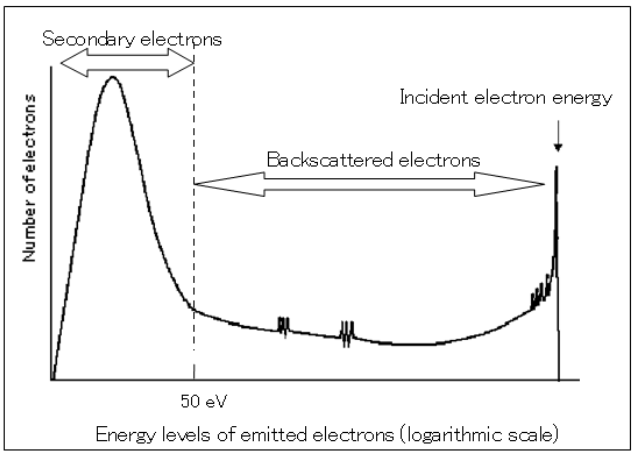

Figure 2. 5 Energy distribution of emitted electrons (Bonet et al., 2010).

The energy level of backscattered electrons is wide-ranging as some electrons are released into the vacuum immediately after the sample has been reached without loss of energy while others lose their energy in varying degrees. The energy distribution of electrons released is shown in Figure 2.5 (Bonet *et al.,* 2010).

The volume of the emission of backscattered electrons is evaluated by the material composition of a sample (by average atomic number). The greater the atomic number, the bigger is the volume of emissions, as illustrated in Figure 2.6 (Goldstein *et al.*, 2018). If the surface area of the sample has differences in the composition, the backscattered electron emission is contrasted by the average atomic number of a component. Therefore, backscattered electron imaging allows to determine the location of high atomic number materials in the specimen before elementary analysis with EDS (Zhou and Wang, 2007).

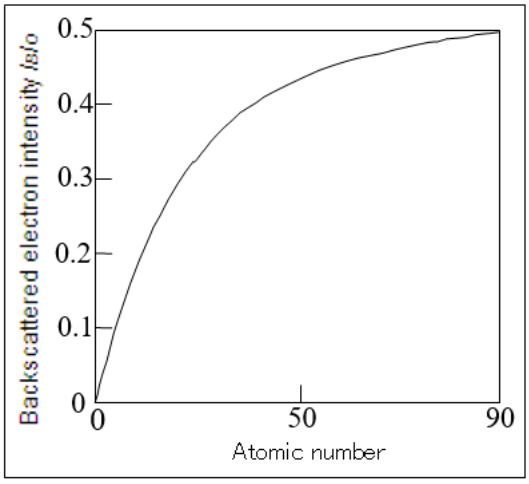

Figure 2. 6 The relation between the atomic number and backscattered electron intensity (emission rate) (Goldstein et al., 2018).

Additionally, emission of the backscattered electron can find out subtle topographical differences which in secondary electron imaging cannot be defined. Therefore, the emission of

the backscattered electron for polished samples can be used to identify delicate variations in depth and to evaluate the hardness of different areas. This effect is greatly improved when the incident electron voltage is decreased (Zhou and Wang, 2007). Furthermore, the emission of backscattered electrons from a solid crystal specimen is dramatically impacted with reference to crystal orientation by the incident angle of electrons. Emission of a multi-crystal specimen of one composition with a different angle of inclination, each of the crystals will produce a different crystal contrast. Therefore, the emission of backscattered electrons is efficient to observe multi-crystal sample grains (Mullerova et al., 2018).

Characteristic X-rays:

When an inner-shell electron is moved by a collision with a primary electron, an outer-shell electron drops into the inner shell in order to re-equalize the orbital charge and ionise the atom (Padua and Wang, 2012). An X-ray photon is released to return the atom to its original energy state. X-ray analysis in a SEM includes detecting radiation for the primary analysis of the sample with certain energy or wavelength. Qualitative and quantitative data can be acquired in the micrometre range with a lateral resolution. The microscope can generate X-ray images in which characteristic X-rays are detected by a certain element and their positions are recorded or "mapped". This enables maps showing how certain elements are distributed through the sample. The maps can be saved together with the corresponding images of SE or BSE (Schatten, 2013).

Auger electrons:

Whenever incidents of radiation (electrons, ions, photons or neutral atoms) interact with an energy exceeding the amount required to remove the inner-shell electron (K, L, M) from the atom, Auger electrons are generated. This scattering period leaves the atom in an excited state with a core hole, that is, a missing inner-shell electron (Buck, Tien and Marcus, 1979).

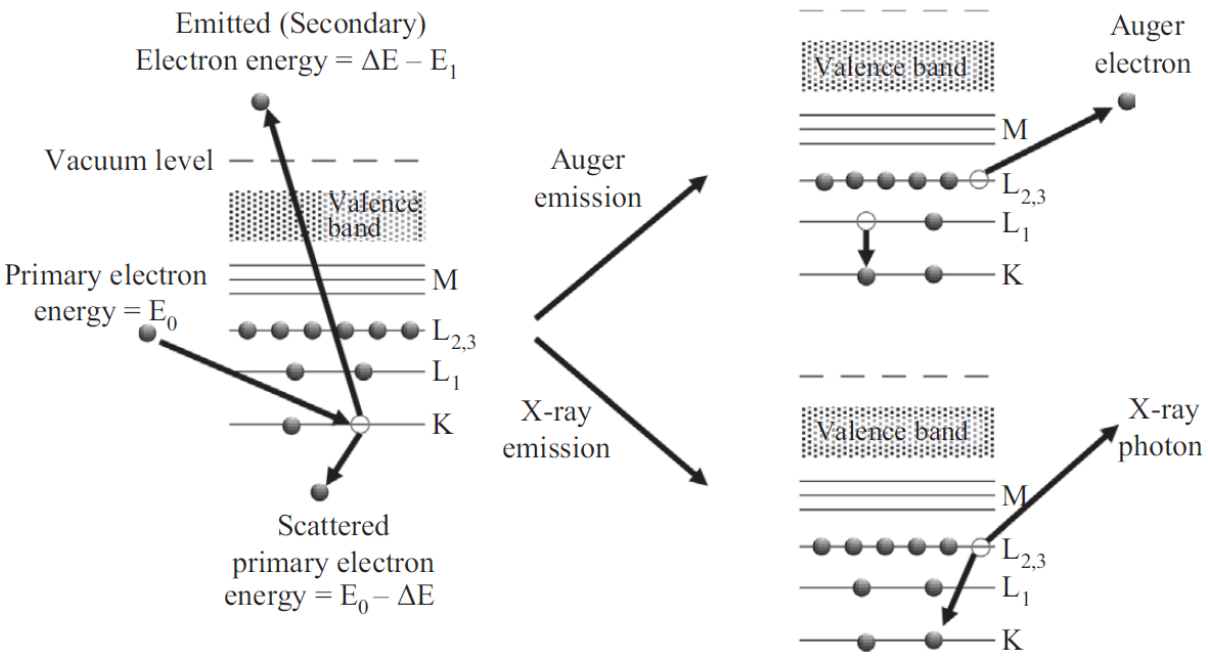

Figure 2. 7 The mechanism used for the release of an electron from Auger or the X-ray photon (Wolstenholme, 2015).

The emission of Auger electron is a consequence of a relaxation process which follows up the excitation, as shown in Figure 2.7 on the left side, and it leaves a hole (electron absence) in a deep-lying energy level, a K level in this case. After the SE emission, the atom is now an ion which is an excited state and relaxes to its ground state. Figure 2.7 (right) indicates two possible processes for this relaxation. One is the Auger electron exclusion. A higher-level electron (e.g., an L-level) fills the hole and a third electron (e.g., another L electron) is expelled. This third electron is the Auger electron. Second process is that the electron in a higher energy state fills the hole with X-ray photon emissions (Wolstenholme, 2015).

The kinetic energy of the emitted electron depends on just three energy levels, and it is independent of the primary beam energy of electron provided that the primary electron beam has enough energy to ionise initially. The Auger process is often a three-electron process when one ignores the primary electron initiating the process (Wolstenholme, 2015).

2.2.2 SEM summarization

2.2.2.1 SEM summary of construction

The SEM contains a column of electron beams, samples stage, signal detectors and signal processing system in order to track and capture images of specimen in real time as shown in figure 2.8 (Padua and Wang, 2012). The beam column, sample stage, and detector are located in a vacuum chamber with control electronics and a high-voltage power supply. The column consists of an electron gun, lenses and apertures, a coil for beam scanning, and a deflector /

acquisition system to collect and process signal information, which is displayed on the monitor as images or graphs (Wolstenholme, 2015).

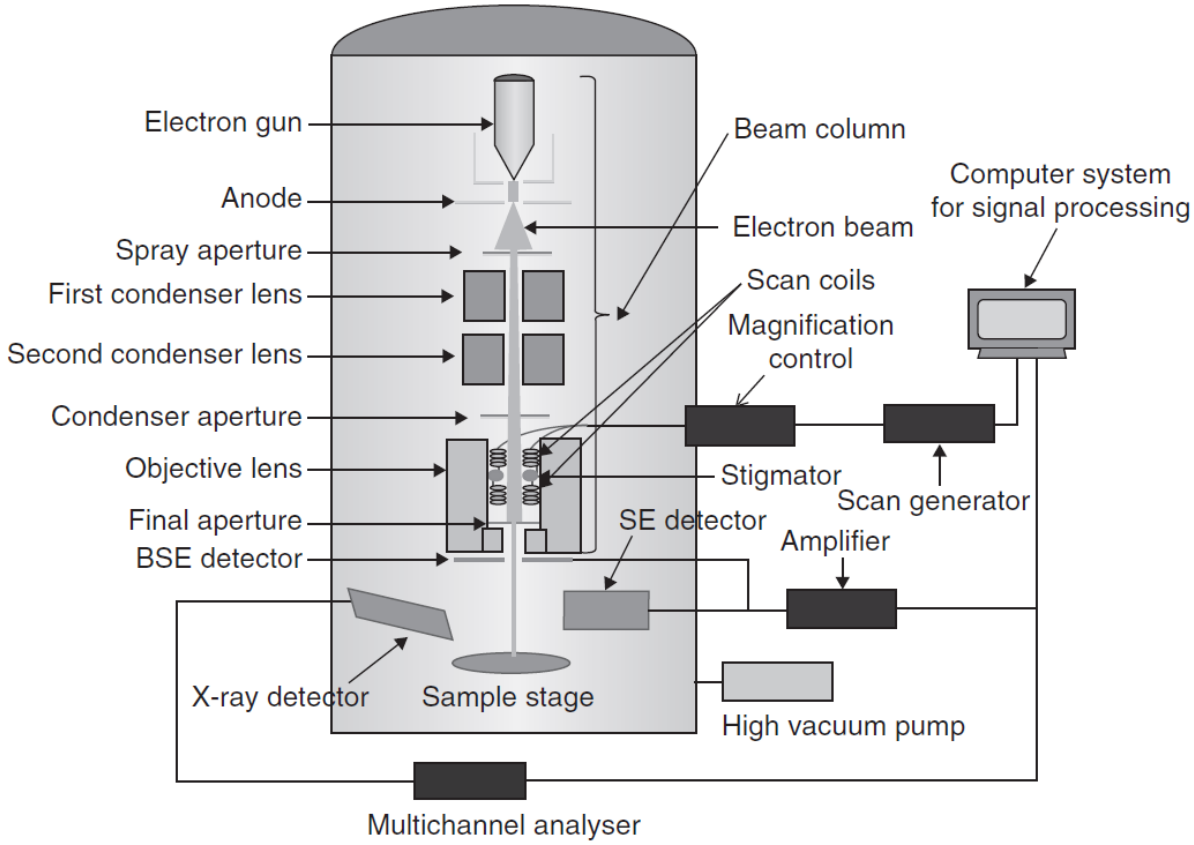

Figure 2. 8 A schematic representation of a typical SEM (Padua and Wang, 2012).

Electron sources:

The SEM needs a stable electron beam to be generated with a high current, small spot size, adjustable energy and low dispersion of energy. SEM systems have two main types of electron source: thermionic and field-emission electron guns. The features of the beams are substantially different. In a thermionic electron gun (Fig. 2.9a) (Padua and Wang, 2012), an electron is drawn out of a hot filament, centred with a negative electrical potential (~500 V) and drifts into the Wehnelt cylinder and then is accelerated into the anode at 0.1-30 keV voltage. The thermionic electron gun is highly suited for X-ray analysis (1 pA to 1000 nA) and it has steady beam current. This type of electron source does not require ultra-high vacuum (Schatten, 2013).

A strong electron field (109 V/m) is utilised for electrons' extraction from extremely sharp single crystal tungsten tip in a field-emission electron gun (FEG) (Fig.2.9b) (Padua and Wang, 2012). Two anodes are needed for a FEG: first one, for the field strength and emissions current at the tip and second one for electrons at the last operating voltages to be accelerated. At room temperature, the cold FEG works. A FEG has a much greater luminosity of the source (current per solid angle) and a lower energy dispersion than a thermionic gun; however, it requires a

high vacuum in the chamber – almost as much as ~10^{-8} Pa. The small beam crossover formed by a FEG permits SEM imaging with a high resolution (Padua and Wang, 2012).

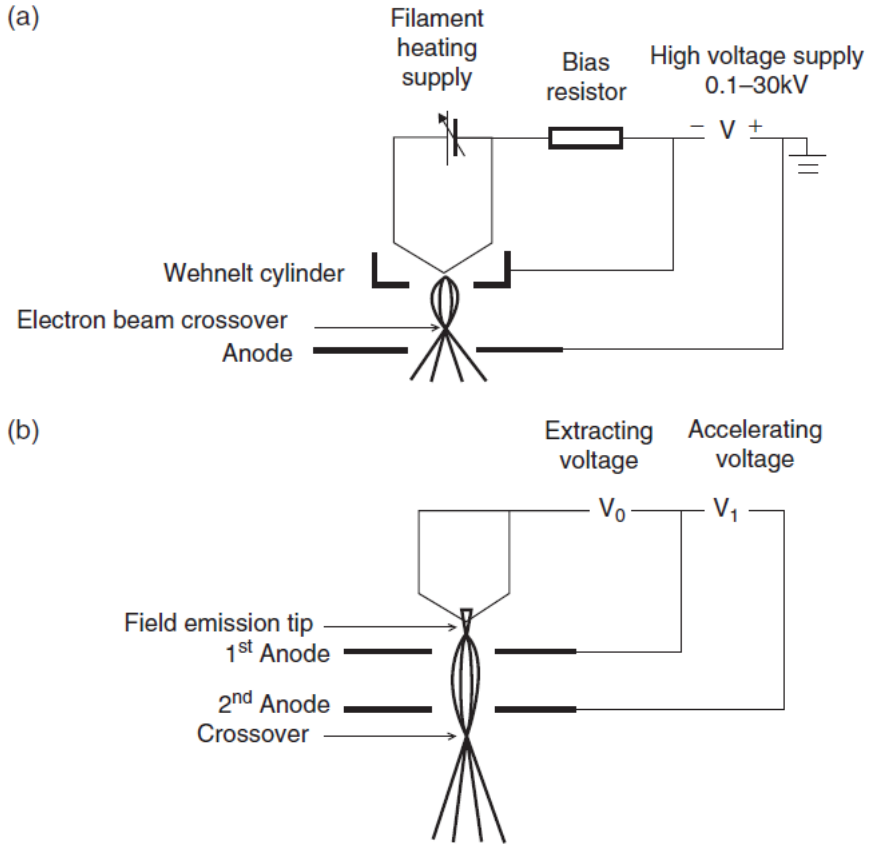

Figure 2. 9 Scheme diagrams of (a) a thermionic electron gun and (b) a field emission electron gun (FEG) (Padua and Wang, 2012).

Lenses and apertures:

To form a high-resolution image, the crossover diameter of the electron beam generated by the electron gun is quite large. Under the electron gun, electromagnetic lenses detach the crossover image (10–20 μm for a thermionic gun) into the final sample size (1 nm–1μm) of the spot. The final spot could be decreased to 1 nm with a field-emission source (Stokes, 2008).

The electron beam is de-magnified and oriented with a collection of electromagnetic lenses. Electromagnetic lenses are composed of a copper wire coil inside a cylindrical soft-iron shell (Padua and Wang, 2012). The coil current induces an axial symmetry of magnetic field. The electrons are radial, circumferential, and spiralling to the centre of the lens, thus concentrating. Improving the strength of the field by incremental change of the current through the coil leads the focus of the electron beam to move upward, lowering the beam spot size (Stokes, 2008).

In the SEM column, there are two types of lenses: condenser and objective lens. The electrons pass first through the condenser lens to widen the crossover diameter of the electron beam formed in a smaller size by the electron gun. The condenser lens has a significant role to determine the final beam size and beam current. Two condenser lenses are generally utilised,

paired together and controlled through a single knob. The last lens in the column is the target lens focusing the electron beam on the surface of the sample through the movement of the crossover of the beam along the optical axis. The lens gap contains scanning coils that provide the beam to raster surface of the sample; stigmator coils that fix the aberration of lenses, named astigmatism; and the target aperture that controls convergence angle of the beam. To obtain high image resolution, the SEM specimen need to be close to the gap since lens aberration is enhanced with focal length, increasing the final probe size (Padua and Wang, 2012).

Spot-size decrement is similarly distributed with lenses in the column for optimum resolution. Decrement is provided through the proper combination of lens demagnification and aperture size. Depending on the system design, various apertures are utilised in the column. To exclude scattered electrons and to check spherical aberrations in the final lens, apertures are utilised. An aperture following the condenser lens restricts angular range of electrons and enable them to pass through the objective lens, while a final aperture in the objective lens defines the semi-angle of the electron 's final convergence (Padua and Wang, 2012).

Electron beam scanning:

The scanning of electron beam is formed through the scan coils which are mounted inside the objective lens. Guided by that of the scan coil, the electron beam travels through x- or y-axis over the sample surface and produces a point-to-point image of the scanning area by use of detectors. The number of signals entering the detector at each point determines the intensity of the screen pixels. The scanning area on the specimen to that of the recorded stage provides the magnification. A variation in the magnification is a variation of the scanned area size (Padua and Wang, 2012).

Lens Aberrations:

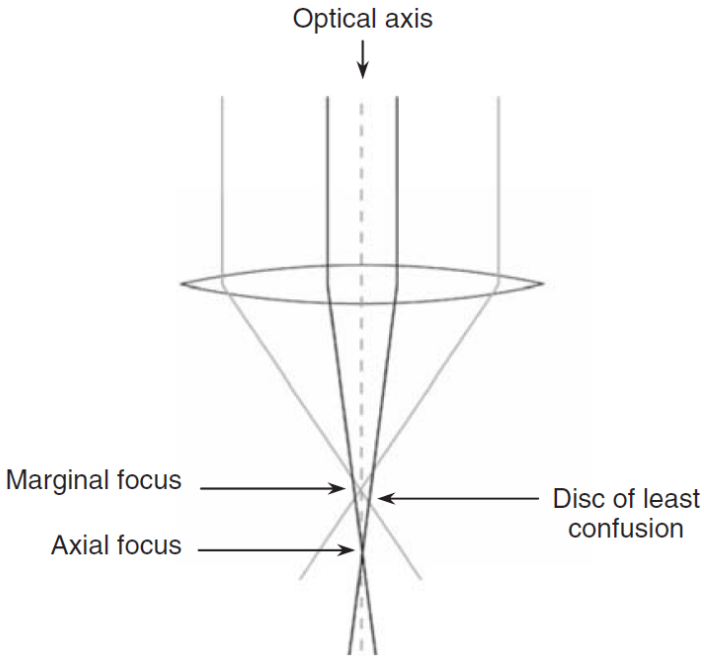

Figure 2. 10 Schematic diagram of the spread of electron beams due to the spherical aberration of the objective lens (Stokes, 2008).

Electromagnetic lenses influence the electron beam focus and are the limits to the highest resolution of a device (Goldstein *et al*., 2018). They allow the electrons to be concentrated in different ways and lead the beam to have a finite minimum diameter instead of being an infinitely sharp point. The least confusion disc is considered to be the minimum diameter of electron beam (Stokes, 2008).

Spherical aberration is a very significant lens defect. Electrons which reach the lens further away from the optical axis are more highly focused than electrons that enter the lens closer to the optical axis. This is demonstrated in Figure 2.10 (Stokes, 2008). The coefficient of spherical aberration C_s frequently indicates the lens quality. The ds minimum beam diameter is a function of C_s and the convergence semi- angle α:

$$ds = 1/2 C_s \alpha^3 \quad (2.1)$$

C_s is proportional with focal length, f; therefore, short f lenses are desirable in order to minimise the effects of spherical aberration and tightly focused primary beam maintenance (Stokes, 2008).

Another type of defect is astigmatism due to asymmetries in the lenses or dirty apertures. In consequence, this means that in perpendicular directions there are two distinct focal lengths. This results in a greater entire beam diameter than it should be. It is illustrated schematically in Figure 2.11 (Stokes, 2008).

Another type of defect is astigmatism due to asymmetries in the lenses or dirty apertures. In consequence, this means that in perpendicular directions there are two distinct focal lengths.

This results in a greater entire beam diameter than it should be. It is illustrated schematically in Figure 2.11 (Stokes, 2008).

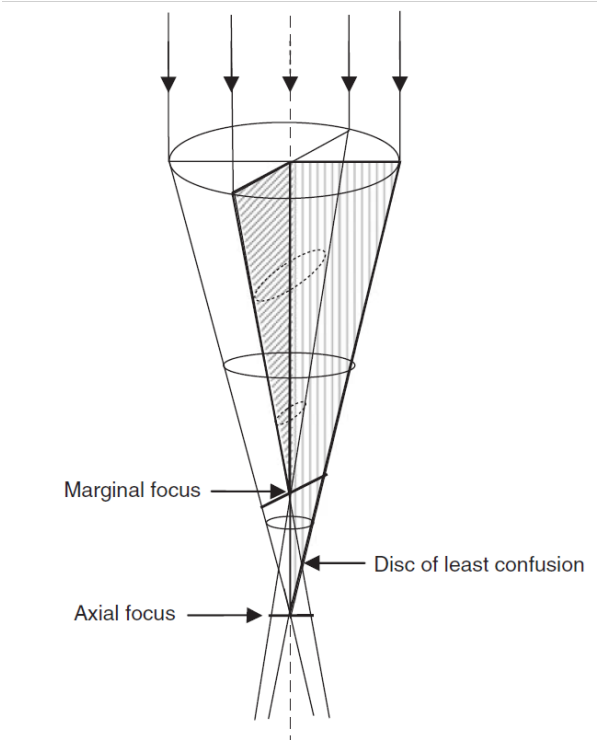

Figure 2. 11 Outline that show astigmatism results in an increased area of the beam size caused by variations in focus on vertical and horizontal planes. Applying weak magnetic field in the lens can easily correct astigmatism (Stokes, 2008).

Astigmatism could be observed by moving the focus above and below the focal plane. There is a smearing of the image that changes in (x – y) direction. Stigmators, which add the counter-field in the x- and y- directions, may reshape the beam to a circular section in these planes, reducing the beam diameter and increasing the resolution (Goldstein *et al*., 2018).
When working at magnification above about 10 000x, the astigmatism is checked and corrected periodically as a routine (focus, stigmata, focus) in order to produce the best possible results. The final beam diameter d_p is then eventually defined with condenser lens strength, aperture size(s), a combination of source size and different aberrations (Goldstein *et al*., 2018).

Vacuum:

In order to prevent contamination of electron sources and scattering of gas molecules through the electron transport, a high-vacuum environment is required. The high vacuum in the entire column depends on the source of the electron. The materials put in the vacuum chamber should be vacuum-friendly, which does not allow for volatile components. There are many organic materials, foams, emulsions, water oils that cannot be in the vacuum chamber to be imaged directly. Preparations such as chemical fixing, dehydration, freeze drying, and critical point drying are needed to eliminate potentially volatile substances. The structural or chemical nature

of the material to be analysed should not change by an appropriate preparation process (Stokes, 2008).

Conductive coatings:

The bombardment of the specimens with relatively high-energy electrons rapidly leads to charging up of the specimen if is not electrically conductive. Insulating specimens are generally sputter-coated with a conductive material like gold platinum or palladium. The electrically conductive layer does not conduct an insulating sample, but it offers only a ground plane for the electrical field. If this conductive coating is thick, it can lead to hiding some properties of the sample (Padua and Wang, 2012).

2.2.3 X-ray diffraction (XRD)

X-ray diffraction is a key tool used in order to determine phase parameters, orientation, crystallite size and other structural parameters by comparing them to data from known structures. It also helps to determine the (crystallographic) structure of novel or unknown crystalline materials (e.g. cell parameters, space group and atomic coordinates) (Dinnebier and Billinge, 2008).

X-radiation ("X-rays") is wavelength electromagnetic radiation of approximately 0.1Å to 100Å, usually comparable to interatomic crystal distances. This is useful since crystal structures allow x-rays to be diffracted (Dinnebier and Billinge, 2008). Diffraction takes place as light is scattered via a periodic array with long-range order, as a result of this, a constructive interference is produced. First of all, every atom can be seen as a consistent scattering point. The frequency by which an atom scatters light is proportional with the number of electrons across the atom. Moreover, atoms in a crystal are distributed regularly and therefore can diffract light (Mittemeijer, 2013).

The scattering of X-rays induces diffraction template that includes atomic information about the crystal arrangement. Amorphous materials such as glass have no periodic arrays, and the diffraction pattern is not formed (Mittemeijer, 2013).

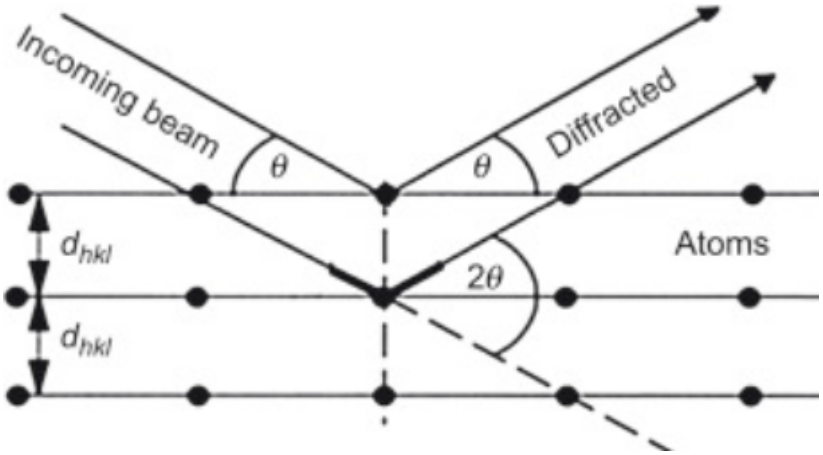

Figure 2. 12 X-rays diffraction by the regularly spaced atoms of a crystal (Pickover, 2011).

There are two plane waves at X-ray wavelengths, each one reflecting off a different plane of atoms within a crystal's lattice, as demonstrated in Figure 2.12 (Pickover, 2011). The distance between these parallel planes of atoms determines the location of diffraction peaks. The Bragg equation defines this condition (Balyan, 2017).

Bragg's Law

$$\lambda = 2d_{hkl} \sin\theta \tag{2.2}$$

The law of Bragg calculates the angle at which a diffraction peak is created by constructive interference from X-rays scattered through parallel planes of atoms. In the equation, the X-ray wavelength λ is fixed for most diffractometers. A family of planes, therefore, only generates a diffraction peak at a certain angle 2θ. d_{hkl} is the vector from the unit cell's origin that intersects the crystallographic plane, given by Miller indexes (hkl), at a 90°angle and the magnitude of vector d_{hkl} is the distance between the parallel planes of atoms in the family (hkl). Lastly, d_{hkl} is a geometrical function of unit cell size and shape (Dinnebier and Billinge, 2008).

(a) (b)

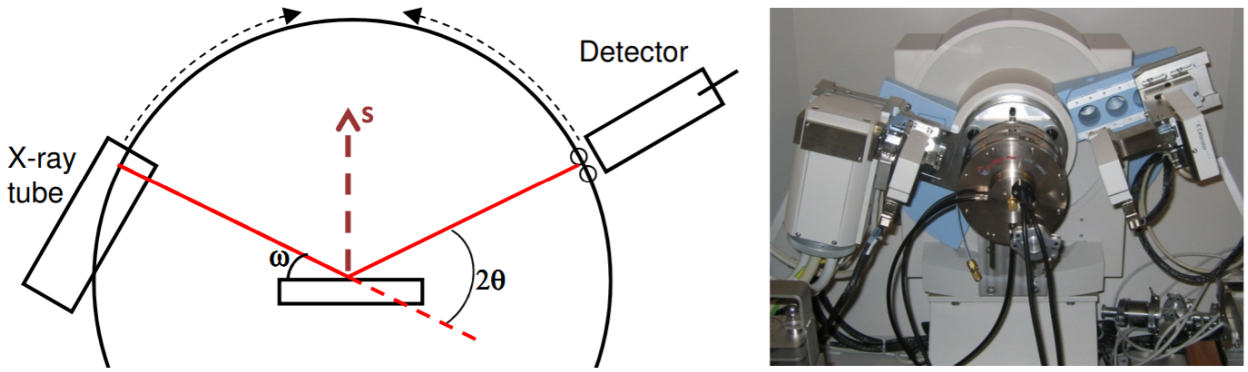

Figure 2. 13 (a) The BraggBrentano geometry and (b) the PANalytical X'Pert Pro Multipurpose Diffractometer (MPD).

In this thesis, X-ray diffraction (XRD) was carried out using PanalyticalX'pert Pro Multipurpose diffractometer to investigate the crystal and amorphous morphology as shown in Figure 2.13b). The geometry of our powder diffractometers is typically BraggBrentano (see Figure 2.13a). The incident angle, ω, is determined between the X-ray source and the sample and the diffraction angle, 2θ, is specified between the incident beam and the detector. The incident angle ω is always ½ of the detector angle 2θ. Lastly, in the Bragg-Brentano geometry, the diffraction vector (s) is always normal to the surface of the sample.

2.2.4 Analysis of the surface area and pore size

Adsorption:

The adsorption is defined as the increased density of fluids near the interface if a solid surface is in contact with a gas or liquid. It is important and widely used due to its use in the determination of surface areas, pore volumes and pore size distributions of porous materials, catalysts and adsorbents in particular.

The term "adsorption" refers to a process in which the molecules aggregate into the interfacial layer, and desorption indicates the opposite. The solid material on which adsorption takes place is the “adsorbent”. The adsorbed substance is described as the "adsorbate," but when considered as the bulk fluid, it is called the "adsorptive." The process of penetration into the bulk solid or liquid phase is termed "absorption" by the adsorbate molecules. The relationship between the adsorbed species and equilibrium pressure or concentration at a constant temperature is also called adsorption isotherm.

Adsorption can be caused by physical or chemical interactions between the adsorbate and the adsorbent and is referred as physisorption or chemisorption, respectively. Adsorption is followed by a reduction in free energy and entropy of the adsorption system, which is an exothermic process.

The most important distinctive features between physisorption and chemisorption as explained by Rouquerol et al (2014):

- Physisorption is a general, a relatively low-specific process.
- The chemisorbed molecules are associated with reactive surface parts, which necessarily forms a monolayer adsorption while physisorption usually forms multilayers at a relatively high pressure.
- A physiosorbed molecule maintains its existence and on desorption returns to the fluid phase in its original form (it is a reversible process).

- Chemisorption energy is comparable to chemical reactions and has the same magnitude of the energy change. Physisorption is still exothermic, but in general, the energy involved is not much greater than the condensation energy of the adsorptive.
- Chemisorption frequently requires an activation energy and often there is not enough thermal energy at low temperatures to achieve thermodynamic balance.

Types of adsorption isotherms:

Physisorption Isotherms: The quantity of gas adsorbed, n^a, m^s of solid, depends on balance of pressure, p, temperature, T and the environment of the gas-solid system. One can write for a certain gas adsorbed on a particular solid at a constant temperature:

$$\frac{n^a}{m^s} = f(p)_T \qquad (2.3)$$

$$\frac{n^a}{m^s} = f\left(\frac{p}{p^0}\right)_T \qquad (2.4)$$

If the gas has its critical temperature below, equation (2.4) is applied. Where po is the saturation pressure of adsorption at T.

Equations (2.3) and (2.4) are the relationship between the quantities adsorbed by the solid mass unit and the equilibrium pressure (or relative pressure) at a specified temperature. These data are typically illustrated with a graph.

Adsorption isotherms have various characteristic forms of graphs, which is important because these graphs provide useful initial information on the adsorbent's pores structure.

The most of vapour isotherms can be classified into nine classes which are shown in Figure 2.14 according to an expanded IUPAC classification (Rouquerol *et al.,* 2014).

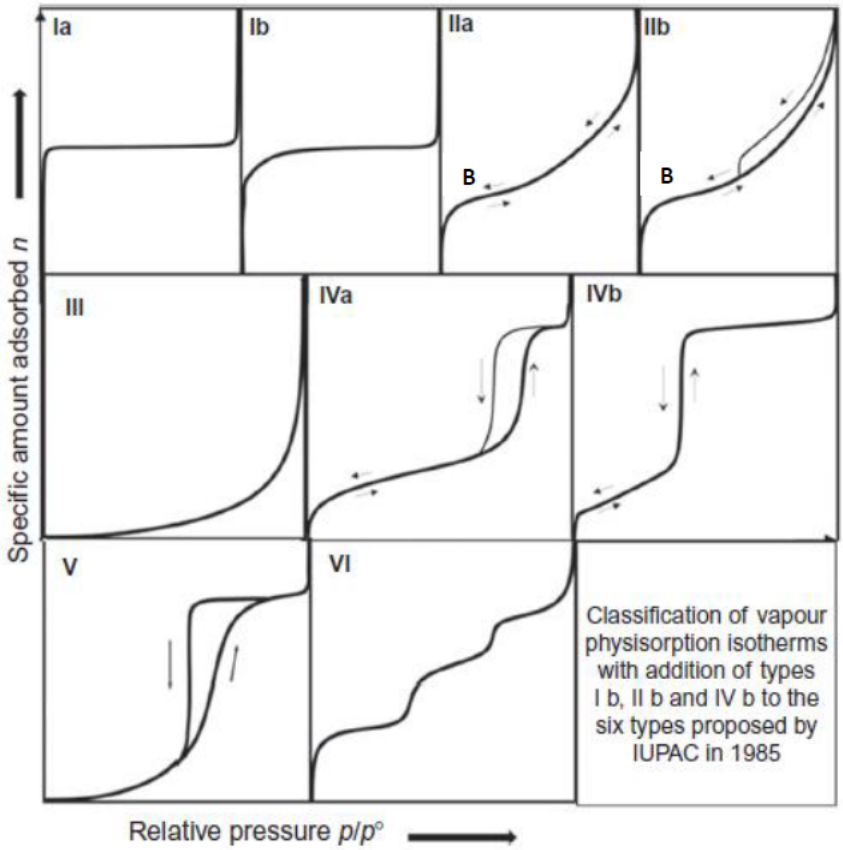

Figure 2. 14 Classification of vapour adsorption isotherms (Rouquerol et al., 2014).

Types I, II, III, IV and V were identical with what Brunauer, Deming, Deming and Teller had originally suggested (1940).

The isotherms type I(a) and I(b) are reversible and concave to the relative pressure P/P_0 axis. At low relative pressure they rise sharply and reach the plateau, which means that, with a relative pressure approached to 1, the amount adsorbed by unit solid mass approaches a limiting value. Type I(a) is for filling narrow micropores, and Type I(b) is for revealing broader micropores.

Type II isotherm shall be concave, nearly linear and ultimately convex to the relative pressure axis. The form is typical of a non-porous or macro-porous adsorbent that allows unregulated multi-molecular adsorption at relatively high pressure. The adsorbed layer becomes liquid or solid bulk when the balance pressure reaches the saturation vapour pressure. Point B is frequently a final stage to the monomolecular layer and the start of the formation of the multimolecular layer. The value at point B of the ordinate provides an approximation of the amount of adsorbate needed to cover a completing monolayer of the unit mass of the solid surface. The desorption-adsorption isotherm is completely reversible in Type II(a), while in Type II(b) the inter-capillary condensation creates a narrow hysteresis loop (Sing, 1985; Thommes *et al.*, 2015).

Type III isotherm is uncommon. It is reversible, but convex to the P/P_0 axis, so there is no point B. These isotherms show that the attractive forces between adsorbent and adsorbate are weak on non-porous or macro-porous adsorbent (Sing, 1985; Thommes *et al*., 2015).

Type IV isotherms (a and b) are common for mesoporous adsorbents. The first part is similar to type II isotherm, at high relative pressures they are balanced with a sufficient saturation plateau but may be shorter or reduced to an inflection point. Type IV(a) is more common than Type IV(b) and includes a hysteresis loop that is associated with capillary condensation filling and emptying of mesopores, whereas type IV(b) isotherms are entirely reversible.

The type V isotherm demonstrates that adsorbat-adsorbent interactions on a microporous or mesoporous solid are weak. It is in the beginning of convex on the relative pressure axis and is stable at high relative pressure, as a type IV isotherm. Generally, this isotherm has a hysteresis loop associated with pore filling and emptying (Thommes *et al*., 2015).

Type VI is associated with layer-by-layer adsorption and has "steps" the sharpness of which depend upon the system and the temperature. It is not a common type of isotherm (Sing, 1985).

Chemisorption Isotherms: Usually, these isotherms are comparable to Type I(a) of physisorption isotherms. A chemically bound monolayer has been completed on the plateau. Such isotherms are commonly referred to as Langmuir isotherms. In table 2, main differences between physisorption and chemisorption isotherms are shown.

Table 2 Comparison between Physisorption and Chemisorption Isotherms

Physisorption	Chemisorption
1. Low adsorption heat generally about 20-40 kJ mol^{-1}.	High adsorption heat between 40 and 400 kJ mol^{-1}.
2. Van der Waal forces	Chemical bond forces
3. It normally occurs at low temperature and declines with a temperature rise.	It happens at high temperature.
4. It is reversible.	It is irreversible.
5. It has to do with facilitating gas liquefaction.	The level of adsorption is typically not correlated with gas liquefaction.
6. It is not very specific	It is highly specific
7. This consists of multi - molecular layers.	It consists of mono-molecular layers.
8. No activation energy is needed.	It needs the energy of activation

2.2.4.1 Langmuir Isotherm

An asymptotic method to monolayer surface coverage is predicted by Langmuir adsorption model as adsorbate partial pressure approaches saturation; this is the Type-I isotherm.

Irving Langmuir suggested the Langmuir adsorption model in 1932 and this isotherm model 's key principles are as follows (Langmuir, 1932):

- Adsorption takes place at specific binding positions found on the adsorbent surface.
- All adsorption sites on the adsorbent surface are the same.
- The adsorbent surface is surrounded by a monolayer of adsorbed molecules.
- No interaction between the adsorbed molecules on the adsorbent surface.
- Langmuir equation is determined by adsorption and desorption rates (Langmuir, 1932): If S_0 are available adsorbent surface locations, S is the amount that is occupied, $S_1 = S_0$-S is vacant locations, and C is the solution concentration, then

$$\text{rate of adsorption} = k_1 S_1 C$$

$$= k_1 [S_0 - S] C \tag{2.5}$$

Desorption rate is proportional to the number of sites occupied S:

$$\text{rate of desorption} = k_2 S \tag{2.6}$$

k_1 and k_2, are constant in adsorption and desorption, respectively.

At equilibrium, the rate of adsorption = rate of desorption, or Equation (2.5) = Equation (2.6),

or $$k_1[S_0-S]C = k_2S \tag{2.7}$$

$$k_1S_0C = [k_2+k_1C]S$$

$$S=\frac{k_1S_0C}{k_2+k_1C}$$

$$S = \frac{S_0\,C}{k_2/_{k_1}+C} \tag{2.8}$$

If $So = K_{ads}$ and $k = (k_2/k_1)$ the

$$S= \frac{K_{ads}\,C}{k+C} \tag{2.9}$$

K_{ads} and k are constants with values depending on the nature of the adsorbent and the adsorbate. There are three problems in relation to the equation (2.9). Firstly, how to connect equation with the assumption of the monolayer is not clear. Secondly, adsorption is an irreversible process, so a different mechanism of reaction is required, not that the rate of adsorption is equal to desorption rate (Patiha et al., 2016). Thirdly, the curve (of S versus C) of equation (2.9) is a hyperbolic equation. The value of K_{ads} and k is consequently hard to evaluate directly from the equation (2.9). Nevertheless, it is transformed into the linear form by taking the reciprocal value of both sides of the equation (2.9):

$$\frac{1}{S} = \frac{1}{K_{ads}} + \frac{1}{K_{ads}}\left(\frac{1}{C}\right) \quad (2.10)$$

K_{ads} value is determined from the intercept and *k* from the slope of the curve of (1/S) to (1/C). If C is higher than C+k ≈ C, and equation (2.9) becomes

$$S = K_{ads} \quad (2.11)$$

The reciprocal of equation (2.11) is

$$\frac{1}{S} = \frac{1}{K_{ads}} \quad (2.12)$$

The equation (2.11) inserted into the equation (2.10) provides

$$\frac{1}{K_{ads}} = \frac{1}{K_{ads}} + \frac{1}{K_{ads}}\left(\frac{1}{C}\right) \quad \text{or} \quad k = 0 \quad (2.13)$$

This means that equation (2.10) is not valid when C is comparatively larger than k. If C is smaller than k, then C+k ≈ k, and then the equation (2.9) is turned into

$$S = \frac{K_{ads}\, C}{k} \quad (2.14)$$

The reciprocal of equation (2.14) is

$$\frac{1}{S} = \frac{k}{K_{ads}}\left(\frac{1}{C}\right) \quad (2.15)$$

differing also from equation (2.10)

$S_0 = K_{ads}$ on assumption, if the whole surface is covered (or $S = S_0$), $S = K_{ads}$ than equation (2.14) [or equation (2.15)] becomes

$$k = \mathrm{C} \quad (2.16)$$

This means that the equation (2.10) is also not valid when C is relatively smaller than *k*. It can therefore be inferred that the equation (2.10) is unclear in principle and thus it cannot be used both for K_{ads} and *k* determination.

2.2.4.2 The Brunauer, Emmett and Teller (BET) theory

All other types mentioned in section 2.2.4 with the exception of type I (Langmuir) isotherms mean that the amount of adsorption is not within a limit that corresponds to completion of a monolayer. The development of multilayers, however, is implied in the theory offered by Brunauer, Emmett and Teller's (BET) (1938), who assumed that, in agreement with Langmuir, the rate of adsorption on a bare surface equated the evaporation rate from the first layer of adsorbate (Thomas and Crittenden, 1998).

Brunauer et al. (1938) were able to extend the Langmuir model to multilayer adsorption with the addition of several assumptions and obtain an isotherm equation (BET equation) which has

a character of type II. In the original BET method, the Langmuir kinetic theory of monolayer molecular adsorption was extended to form an infinite number of adsorbed layers at the saturation pressure, po.

According to the BET model, the adsorbed molecules in one layer, can serve as an adsorption site for molecules in the next layer and, the fractions of the surface are (θ_0, θ_1, θ_2, ..., and θ_i) surrounded by 0, 1,2, ... i layers of adsorbed molecules at any pressure below saturation vapour pressure po, (where θ_0 represents the fraction of the bare surface). The adsorbed layer is therefore not intended to be of uniform thickness, but to consist of random molecular stacks.

If the fractions of the bare and covered surface, θ_0 and θ_1, are assumed to remain constant at balance at the pressure p, the rate of condensation on the bare surface may be compared with an evaporation rate from the first layer:

$$a_1 p\theta_0 = b_1 \theta_1 \exp\left(-\frac{E_1}{RT}\right) \tag{2.17}$$

in the equation (2.17) a_1 and b_1 are adsorption and desorption constants, respectively, and E_1 is the positive value of the so-called energy of adsorption for the first layer. a_1, b_1 and E_1 are expected to depend on the number of adsorbed molecules that already exist in the first layer, i.e. no allowance is made for lateral adsorbate adsorbed interactions, as with the Langmuir model.

Similarly, the surface fractions which are at equilibrium pressure p, θ_2, θ_3, ... ,θ_i must be constant too, therefore:

$$a_2 p\theta_1 = b_2\theta_2 \exp\left(-\frac{E_2}{RT}\right) \tag{2.18}$$

$$a_3 p\theta_2 = b_3\theta_3 exp\left(-\frac{E_3}{RT}\right) \tag{2.19}$$

$$\vdots \qquad \vdots$$

$$\vdots \qquad \vdots$$

$$\vdots \qquad \vdots$$

$$a_i p\theta_{i-1} = b_i\theta_i \exp\left(-\frac{E_i}{RT}\right) \tag{2.20}$$

where θ_{i-1} and θ_i represent the surface fractions of i-1 and i layers respectively; a_i and b_i are constants of adsorption and desorption, and E_i represents the energy of adsorption of the i-th layer.

The sum of the surface fractions is equal to unity:

$$\theta_0 + \theta_1 + \cdots + \theta_i + \cdots = 1 \tag{2.21}$$

In addition, the total amount adsorbed may be indicated as:

$$n = n_m[1\theta_1 + 2\theta_2 + \cdots i\theta_i + \cdots] \tag{2.22}$$

In general, each adsorbed layer has a different set of values a_i, b_i and E_i but two main assumptions depend on the derivation of the BET isotherm equation:

- The adsorbing energy E_i has the same meaning as liquefying energy, E_L, for the second and higher layers,

  Liquefying energy, E_L, of the adsorptive i.e. $E_2 = E_i = E_L$;

- The multilayer has infinite thickness at $p/p^0 = 1$ ($i = \infty$).

Let:

$$\frac{b_2}{a_2} = \frac{b_3}{a_3} = \cdots \frac{b_i}{a_i} = g \tag{2.23}$$

where g is constant, since all the layers (except the first) have the same properties. We can now express $\theta_1, \theta_2, \ldots, \theta_i$ in terms of θ_0:

$$\theta_1 = y\theta_0, \quad \text{where } y = \frac{a_1}{b_1} p \exp\left(\frac{E_1}{RT}\right) \tag{2.24}$$

$$\theta_2 = x\theta_1, \quad \text{where } x = \frac{p}{g} \exp\left(\frac{E_L}{RT}\right) \tag{2.25}$$

$$\theta_3 = x\theta_2 = x^2\theta_1 \tag{2.26}$$

$$\vdots \qquad \vdots \qquad \vdots$$

$$\theta_i = x^{i-1}\theta_1 = yx^{i-1}\theta_0 \tag{2.27}$$

A constant C can be defined as:

$$C = \frac{y}{x} = \frac{a_1}{b_1} g \exp\left(\frac{E_1 - E_L}{RT}\right) \tag{2.28}$$

then:

$$\theta_i = C x^i \theta_0 \tag{2.29}$$

We can therefore write:

$$\frac{\boldsymbol{n}}{\boldsymbol{n}_{\mathrm{m}}} = \sum_{i=1}^{\infty} i\,\theta^i = C\sum_{i=1}^{\infty} i\,x^i \cdot \theta_0 \tag{2.30}$$

Considering the sum of an infinite geometric development:

$$\sum_{i=1}^{\infty} x^i = \frac{x}{1-x} \tag{2.31}$$

and of the value of the term

$$\sum_{i=1}^{\infty} i\,x^i = \frac{x}{(1-x)^2} \tag{2.32}$$

and since

$$\theta = 1 - \sum_{1}^{\infty} \theta_i$$

it can be obtained from equations (2.29) and (2.30):

$$\frac{\boldsymbol{n}}{\boldsymbol{n}_{\mathrm{m}}} = \frac{Cx}{(1-x)(1-x+Cx)} \tag{2.33}$$

Once the adsorbed layer is believed to be of infinite thickness in saturation vapour pressure p^o, it is accompanied by the following x=1 and the $x = p / p^o$ (from the equations 2.25), so that

$$\frac{\boldsymbol{n}}{\boldsymbol{n}_{\mathrm{m}}} = \frac{C(p/p^o)}{(1-p/p^o)(1-p/p^o+C(p/p^o)} \tag{2.34}$$

When n/n_m is plotted against p/p^o at constant C, equation (2.34) gives a curve of Type II shape, as long as C >2. The form of the knee (i.e. close $n / n_m = 1$) specifically depends on the value of C. It is sharper as C is increased. If 0<C<2, equation (2.34) gives a curve with no inflexion point with the general shape of a Type III isotherm.

In the usual linear form, the equation (2.34) can be written:

$$\frac{p}{\boldsymbol{n}(p^o - p)} = \frac{1}{\boldsymbol{n}_{\mathrm{m}} C} + \frac{C-1}{\boldsymbol{n}_{\mathrm{m}} C}\cdot\frac{p}{p^o} \tag{2.35}$$

This 'linear transformed BET equation' enables the basis for the BET plot of experimental isotherm data in the form of p/[n(p° - p)] versus p/p°. The surface area, SA_{BET}, and the value of C (usually written C_{BET}) are provided in terms of the slope, S_{BET}, and the intercept, I_{BET}, by the following:

$$SA_{BET} = \frac{A_m}{S_{BET} + I_{BET}} \quad \text{and} \quad C_{BET} = 1 + \frac{S_{BET}}{I_{BET}} \tag{2.36}$$

where A_m is the area which molecule occupies on the surface. Figure 2.15 illustrates the basic method utilised in the BET Theory. The monolayer volume, V_m, from the BET plot is typically used to evaluate the surface areas of catalysts, given that the value of C is acceptable, and the hypothesis of the model apply (Thomas and Schaetzel, 2012).

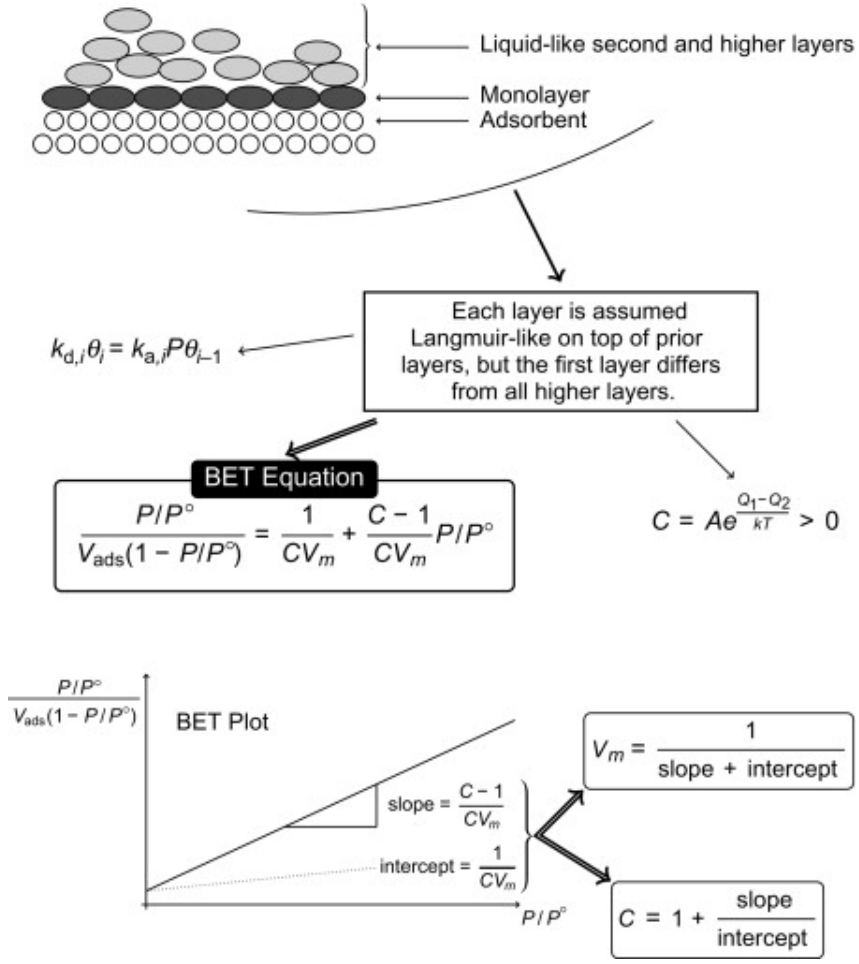

Figure 2. 15 Scheme description and expectations in BET adsorption isotherm (Thomas and Schaetzel, 2012).

2.2.4.3 Barret, Joyner and Halenda (BJH) method

The physical gas adsorption of the molecules of nitrogen on a solid surface is well known to specify pore size distribution. Different gases such as N_2, Ar and CO_2 are often used as adsorptive depending on the adsorbent material 's nature. Utilising, N_2 adsorption at 77 K over

a variety of relative pressures *(p / p_0)* gives knowledge on size distributions in the micro-, meso- and macro-porosity range (approximately 0.5–200 nm) (Groen *et al.,* 2003). Barrett *et al.* (1951) proposed a method which is most widely utilised for calculations of pore size distribution, pore volume and area over the mesopore, relatively roughly porous materials and part of the macropore range. This method is established based on the Wheeler theory which can be summarised by the equation (Ridderbos, 1997):

$$Vs\text{-}V = \pi \int_{r_{Pn}}^{\infty} (r - t)^2 L(r) dr \tag{2.37}$$

where *Vs* and *V* are the gas adsorbed volume at saturation pressure P_o and pressure *P*, respectively. *L(r)dr* is the total length of pores whose radii fall between *r* and *r* + *dr*. The critical radius is r_{pn} , which means the radius of the largest pore is still completely filled with liquid adsorbate at any particular pressure and t is the multilayer thickness which is usually formed at pressure *P*.

Barrett *et al.* (1951) supposed that the system includes open-ended cylindrical pores (shown in Figure 2.16) which are changed by the relative pressure (P/P_0), and all pores of equal radius react in a similar way. If *(P/P_0)* is close to the saturation pressure, the liquid fills all the pores and evaporations take places through the lowering *(P/P_0)*. Under equilibrium, the biggest pore (illustrated in Figure 2.16) of radius r_{p1} has a thickness layer r_k adsorbed. For this reason, the connection between the pore volume V_{P1} and the inner capillary volume V_k can be written as:

$$V_{P1} = \frac{V_{k1}\, r_{p1}^2}{r_{k1}^2} \tag{2.38}$$

However, this equation is not useful, because V_{k1} is unknown.

In order to achieve valuable knowledge, $(P/P_0)_1$ needs to be lowered to a smaller value $(P/P_0)_2$. This allows a measurable volume of adsorbed gas ΔV_1 in the desorption. Relative pressure reduction does not only contribute to emptying of the largest pores of its capillary condensate, but also reduces thickness through the amount Δt_1 in the physically adsorbed layer. As a result of the decline in relative pressure and the related desorption, the equation can be rewritten as:

$$V_{P1} = R_1 \Delta V_1 \tag{2.39}$$

where $R_1 = \frac{r_{p1}^2}{(r_{k1} + \Delta t_1)^2}$

On the other hand, the problem rises if one lowers the relative pressure from $(P/P_0)_2$ to $(P/P_0)_3$ on the second pore. If this occurs, the volume of liquid desorbed not only includes that from the second pore but also from the first pore, that is left behind from a second thinning of the physically absorbed layer. The volume emitted by this thinning is denoted as $V_{\Delta t_2}$ then,

$$V_{P2} = R_2 (\Delta V_2 - V_{\Delta t_2}) \tag{2.40}$$

Where $R_2 = r_{p1}^2/(r_{k2}+\Delta t_2)^2$, and $V_{\Delta t_2}$ is the volume of second thinning.

From figure 2.15, one can write:

$$V_{\Delta t_2} = \pi L_1 \left(r_{k_1} + \Delta t_1 + \Delta t_2\right)^2 - \pi L_1 (r_{k1} + \Delta t_1)^2 \tag{2.41}$$

where L_1 is the pore length of the first pore.

Although, a calculation of $V_{\Delta t_2}$ from equation (2.41) is inconvenient as larger number of pores become involved.

So, another equation for $V_{\Delta t_2}$ is

$$V_{\Delta t_2} = \Delta t_2 A_{c_1} \tag{2.42}$$

where A_{c_1} is the average area from which the physically adsorbed gas is desorbed.

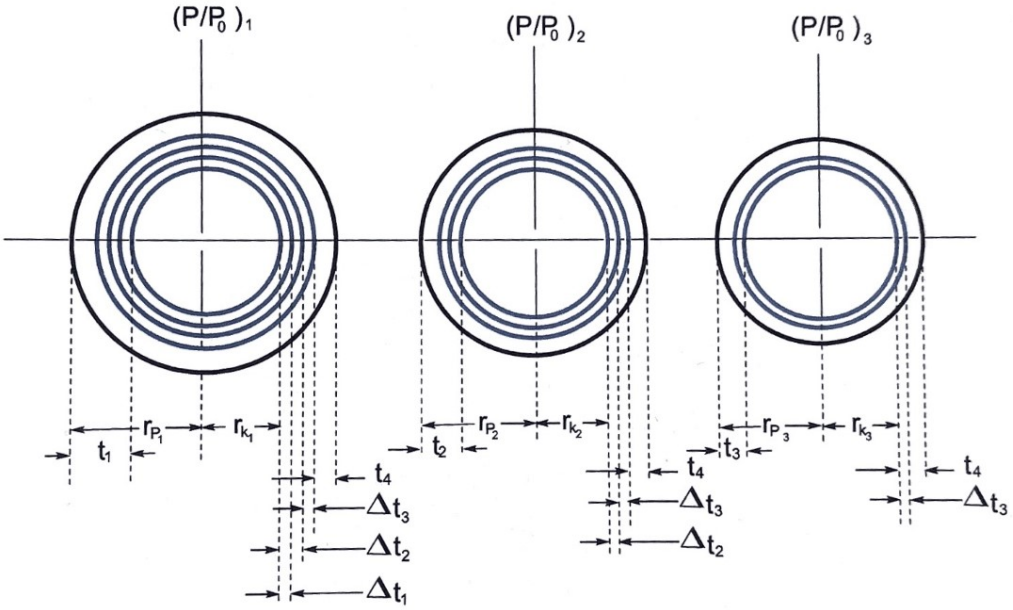

Figure 2. 16 Schematic description of the desorption mechanism with three distinct pores (Barrett, Joyner and Halenda, 1951).

Equation (2.42) can be extended to describe each step of a stepwise desorption by writing it in the form

$$V_{\Delta t_n} = \Delta t_n \sum_{j=1}^{n-1} A_{c_j} \tag{2.42a}$$

The summary in equation (2.42a) can be found clearly as the sum of the average area unfilled pores down to; however, it does not consist the pore that was discharged of capillary condensate in *nth* desorption.

Generalizing equation (2.40) and substituting (2.42a), the porous model is regarded with writing an exact expression form

$$V_{P_n} = R_n \Delta V_n - R_n \Delta t_n \sum_{j=1}^{n-1} A_{c_j} \quad (2.43)$$

Equation (2.43) is not satisfactory due to the unknown values of Ac or $\sum A_c$ during desorption because emptying pores are not stable with the decline in P/P_0.

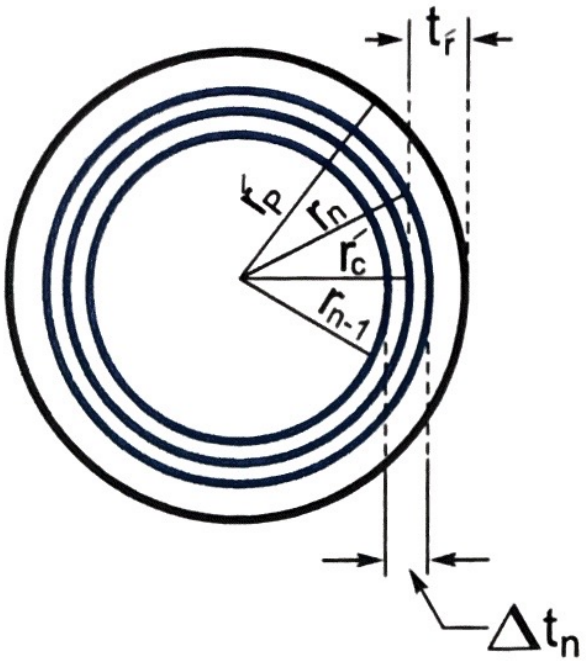

Figure 2. 17 Relation between $V_{\Delta t}$ and r_p at nth desorption step (Barrett et al., 1951).

Figure 2.17 demonstrates the variations in physical thickness of physically adsorbed layer (Δt_n) of an initially emptied pore radius $\acute{r}_p$ in the nth stage of desorption. Before desorption, the capillary radius is r_{n-1} and after desorption r_n and $\acute{r}_c$ are their average value. As the capillary is surrounded by the pore, the average region of the capillary produce thickness Δt_n which is equal to $A_p X(\acute{r}_c/\acute{r}_p)$ during the desorption. When $t_{\acute{f}}$ is the thickness of adsorbed molecular layer, then $\acute{r}_c=\acute{r}_p-t_{\acute{f}}$ can replace A_c in equation (2.43) and therefore it becomes:

$$V_{P_n} = R_n \Delta V_n - R_n \Delta t_n \sum_{j=1}^{n-1} c_j A_{P_j} \quad (2.44)$$

Where $c=(\acute{r}_p-t_{\acute{f}})/\acute{r}_p$.

For an estimate of pore size distributions, equation (2.44) is the base. This technique implies that pores are cylindrical and that the adsorbent is retention in pores of the adsorbent in accordance with the gas phase via two processes either the physical adsorption on the pore walls or capillary condensation in the inner capillary volume. This approach can be used for explaining adsorption or desorption isotherms (Gregg and Sing, 1982).

It must be understood that r_k is calculated with the Kelvin equation (Barrett et al., 1951).

$$Log\ (P/P_o) = \frac{-2\sigma V}{8.316\ x10^7\ x2.303 T r_k} = \frac{-4.14}{r_k} \quad (2.45)$$

where σ is the surface tension of liquid nitrogen, V is molar volume of liquid nitrogen, r_k is the capillary radius in centimetres and T is the absolute temperature.

The surface area, pore size distribution and N_2 adsorption-desorption curves are presented in chapter 5 and 6, they were calculated through BET and BJH methods. Nitrogen adsorption – desorption analysis has been done via SURFER (Thermo Scientific) which is illustrated in figure 2.18 is used to do the analysis.

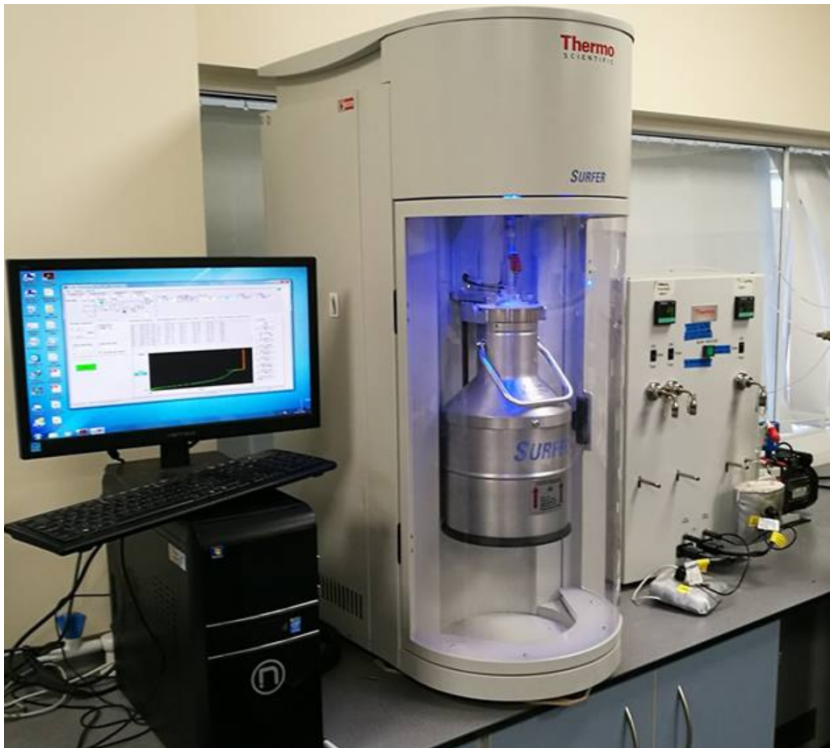

Figure 2. 18 SUFFER's (Thermo Scientific) main parts are Surfer's cabinet and external degasser unit.

All of the samples were degassed and processed in a vacuum and were heated. The degassing process took place in two steps. The first step was completed on an empty glass burette at 120 °C for 15 minutes. The burette mass was registered as m_1. The analysed materials' weight was between 100 and 200 mg. Then, weighted aerogels were put in the burette. The second step of degassing was carried out at 200 °C for 8 hours. Afterward, the material mass and burette were registered as m_2. The net mass of aerogels (m) was calculated by subtraction of m_2 from m_1. The mass m was written to the software of the instrument. Subsequently, the degassed burette was plugged in the analyser and the nitrogen drawer, which was filled with liquid nitrogen, and the burette was automatically submerged for cooling the materials to 77 K during the analysis.

2.2.5 Compression Test

The mechanical properties of materials affect their behaviour upon their exposure to different external forces. Elasticity tends to return to the original form of solid objects and materials, after deformation caused by external forces (load) is removed. Figure 2.19 shows the materials' behaviour under loading in the elastic area of the stress-strain curve based on Hooke's law.

$$\sigma = E\varepsilon \tag{2.46}$$

where σ is the stress, E is Young's modulus and ε is the strain.

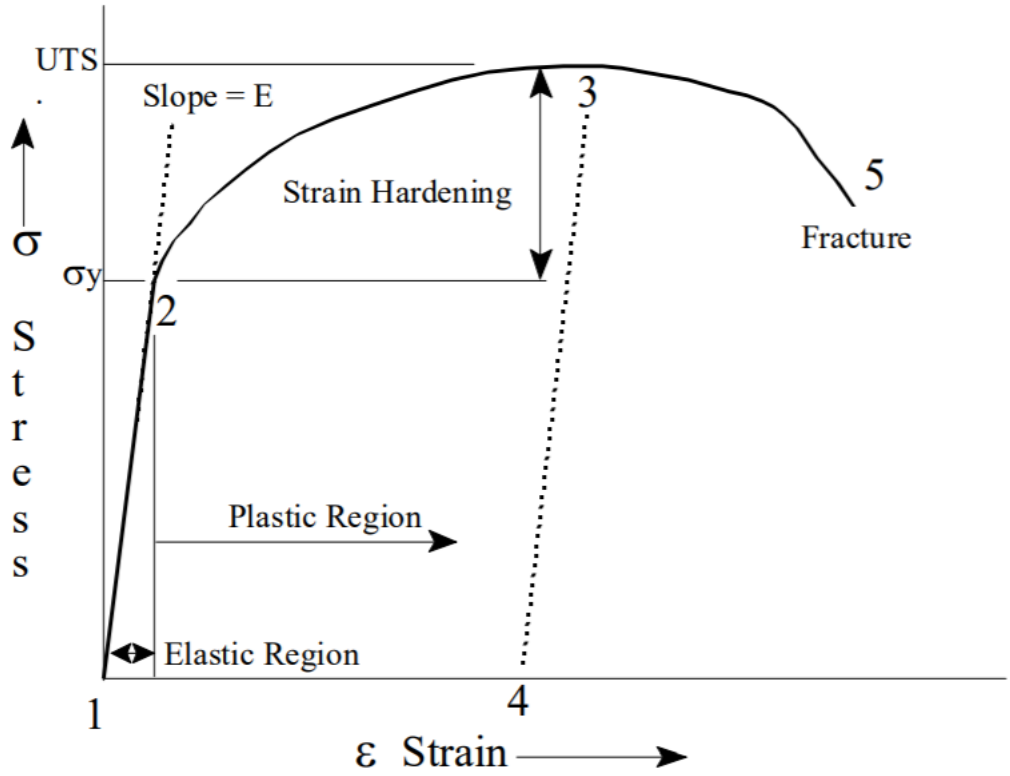

Figure 2. 19 The stress – strain diagram in a tensile test (Pelleg, 2013).

Typical tensile stress-strain curve, which is achieved from subjecting to a continuously increasing tensile uniaxial load on a sample is illustrated in Figure 2.19. When the sample is not loaded anywhere between points 1 and 2, it will revert to its initial form like a rubber band. This type of behaviour is called Elastic and the area between points 1 and 2 is the Elastic Region. The Yield Strength (σ_y) is known as point 2. When it is passed, the sample will no longer return to its original length, but it will show some permanent deformation. This place beyond to point 2 is the Plastic Region.

When the sample is strained beyond Point 3, the stress diminishes as non-uniform deformation and necking take places. The material will ultimately reach Point 5 at which it fractures.

Tensile strength (TS) or Ultimate Tensile strength (UTS) are the highest stress value on the diagram. It is the most stress that the sample can withstand without breaking.

The other type of stress is the compressive stress which is shown in Figure 2.20. In general, the use of a compressive stress in a sample decreases with its size. Ductile materials show similar compression and tensile test results when fragile materials are of greater strength and strain in the compression test prior to the fracture compared to the tension test.

Necking is the distinctness between the stress – strain diagram in a compression and the tensile test. However, in a tension test, a maximum, the UTS, is obtained accompanied by a reduce in stress until fracture, and during the compression, the stress continues to increase until fracture sets in. Obviously, the absence of necking in compression testing is correlated with this behaviour. Instead of tension test, compression testing is preferred to analyse the mechanical properties of nonstandard samples as the shape of the material is easier to prepare for a compression test. On the other hand, to achieve correct results, the ratio of material length, h, to its diameter, d, must be less than two-three, i.e., h/d < 2.0–3.0 from nonstandard materials (Pelleg, 2013).

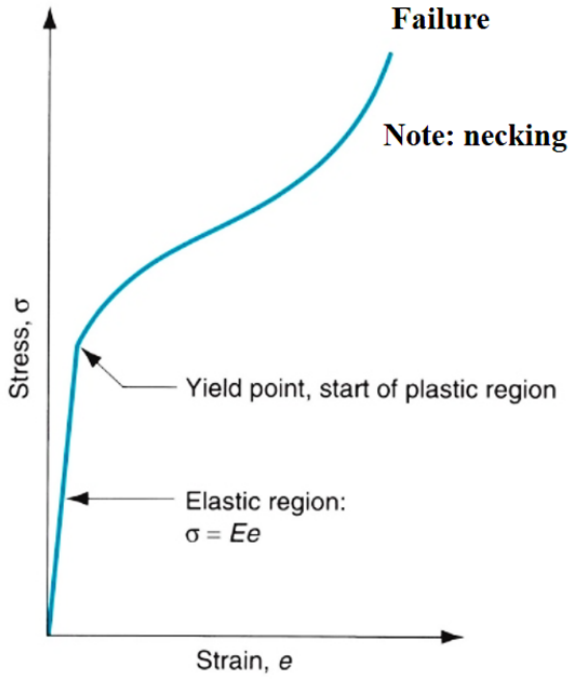

Figure 2. 20 Stress-strain behaviour in a compression test (Pelleg, 2013).

In chapter 4, uniaxial compression tests were applied with ASTM D695 by using a universal test machine (Tinius Olsen H25KS). Monolithic and graphene oxide doped silica aerogels were cut in disk shapes. The displacement's speed was checked by 0.5 mm/min and the load cell was 5000 N for the loading-displacement evaluations.

2.2.6 Fourier transform infrared spectroscopy (FTIR)

FTIR technique is utilised to identify organic, inorganic, and polymeric materials using infrared light. The characteristic pattern of absorption bands explicitly demonstrates an alteration in the

sample composition. Moreover, FTIR is beneficial for uncertain samples' identification and characterisation, specifying contamination in a sample, determining additives, decomposition and oxidation identification.

Figure 2.21 displays a schematic description of FTIR. A standard FTIR spectrometer contains a source, sample cell, detector, amplifier, A/D convertor, and a computer. A / D converter and amplification amplify and transform the input to a digital signal, the signal is then sent to the computer where the Fourier transform takes place (Berthomieu and Hienerwadel, 2009).

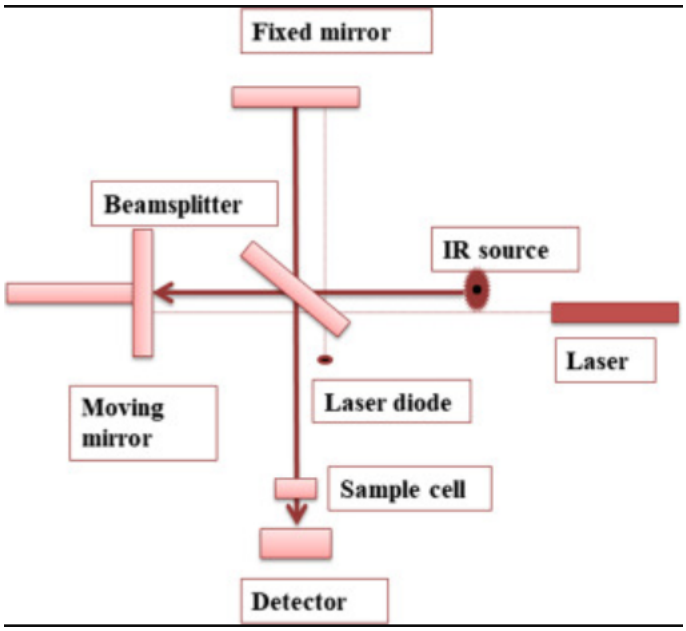

Figure 2. 21 Schematic diagram of FTIR (Titus, Samuel and Roopan, 2019).

Infrared radiation of approximately 10,000–100 cm−1, absorbing part of the radiation and some getting passed through, is delivered to the sample. The absorbed radiation is transferred to vibrational or rotational energies of the material. The corresponding signal at the detector is typically a spectrum from 4000 to 400 cm^{-1} representing the molecular fingerprint of the materials. Any molecule has a distinctive fingerprint, making FTIR an important method for chemical specification (Titus, Samuel and Roopan, 2019).

Figure 2. 22 (1) The in-situ electrochemical FTIR cell; (2) BioRad FTS 6000 Spectrometer; [(3) 325nm Laser]; (4) Heated block controller; (5) Control PC; (6) Heating/ cooling unit; (7) Cooling/heating tubes to cell.

FTIR spectrophotometer which is displayed in Figure 2.22 was carried out to investigate the chemical composition of the synthesized water-glass silica aerogels in chapter 3. A tiny sample piece was positioned among a high refractive crystal index and a clamp made of a metal tip. The infrared radiation was sent to the specimen via the crystal at a given angle for total reflection. Only few wavelengths of light such as 0.5 to 2.0 microns were able to penetrate into the specimen. The reflected beam was directed to the detector, which resulted in the material's infrared spectrum.

2.2.7 Raman spectroscopy

Raman is a type of vibrational molecular spectroscopy that is based on the interaction of light with matter. Light is electromagnetic radiation made up of many particles known as photons. When light occurs on a specimen, photons may be absorbed, scattered, and reflected when interacting with the specimen or without any contact will move through the sample. The spectroscopy of Raman is based on light scattering (Holze, 2005).

The spectrum of Raman is comprised of a number of Raman peaks, each of which corresponds to various molecular vibrations (e.g. stretch, bend, wave, rock, twist, etc.) of chemical bonds within the specimen, the frequencies of which vary for each molecule. Every molecule has its own molecular vibration set, so Raman's spectrum produces a unique chemical fingerprint (Holze, 2005).

FTIR and Raman spectroscopy are complementary techniques and provide substantially the same chemical information. However, FTIR spectroscopy is focused on changes in the dipole moment of vibrating molecules, whereas Raman spectroscopy is focused on changes in the polarizability of vibrating molecules upon interaction with light. In fact, Raman spectroscopy is essentially more sensitive to molecular asymmetric bonds, while FTIR spectroscopy is sensitive to symmetric molecular bonds (Holze, 2005).

2.3 Conclusion

In this chapter, the synthesis of monolithic and GO doped silica aerogels are explained. Moreover, the principles of operation of the techniques which are used to characterise produced aerogels are explained. Lastly, all used techniques for example, SEM, XRD, BET, BJH, compression test, FTIR and Raman spectroscopy are detailed.

References

Balyan, M., 2017. X-ray nonlinear Bragg diffraction. *Journal of Nanophotonics*, 11(1), p.016003.

Barrett, E., Joyner, L. and Halenda, P., 1951. The Determination of Pore Volume and Area Distributions in Porous Substances. I. Computations from Nitrogen Isotherms. *Journal of the American Chemical Society*, 73(1), pp.373-380.

Berthomieu, C. and Hienerwadel, R., 2009. Fourier transform infrared (FTIR) spectroscopy. *Photosynthesis Research*, 101(2-3), pp.157-170.

Bonet, C., El-Gomati, M., Matthew, J. and Tear, S., 2010. Monte Carlo modelling of the low-loss electron signal in scanning electron microscopy and comparison with the BSE signal. *Journal of Physics: Conference Series*, 209, p.012070.

Brunauer, S., Deming, L., Deming, W. and Teller, E., 1940. On a Theory of the van der Waals Adsorption of Gases. *Journal of the American Chemical Society*, 62(7), pp.1723-1732.

Buck, O., Tien, J. and Marcus, H., 1979. *Electron and Positron Spectroscopies In Materials Science And Engineering*. New York: Academic Press.

Dinnebier, R. and Billinge, S., 2008. *Powder Diffraction*. Cambridge: Royal Society of Chemistry.

Goldstein, J., Newbury, D., Michael, J., Ritchie, N., Scott, J. and Joy, D., 2018. *Scanning Electron Microscopy And X-Ray Microanalysis*. New York, NY: Springer New York.

Gregg, S. and Sing, K., 1982. *Adsorption, Surface Area, And Porosity*. London: Academic Press.

Groen, J., Peffer, L. and Pérez-Ramírez, J., 2003. Pore size determination in modified micro- and mesoporous materials. Pitfalls and limitations in gas adsorption data analysis. *Microporous and Mesoporous Materials*, 60(1-3), pp.1-17.

Han, X. and Siller, L. (2015) 'Aerogel synthesis', P221149GB/DW (WO2016132117 A1).

Han, X., Hassan, K., Harvey, A., Kulijer, D., Oila, A., Hunt, M. and Šiller, L., 2018. Bioinspired Synthesis of Monolithic and Layered Aerogels. *Advanced Materials*, 30(23), p.1706294.

Hummers, W. and Offeman, R., 1958. Preparation of Graphitic Oxide. *Journal of the American Chemical Society*, 80(6), pp.1339-1339.

Langmuir, I., 1932. VAPOR PRESSURES, EVAPORATION, CONDENSATION AND ADSORPTION. *Journal of the American Chemical Society*, 54(7), pp.2798-2832.

Lyman, C., 2013. Short Courses for Scanning Electron Microscopy and X-ray Microanalysis. *Microscopy and Microanalysis*, 19(S2), pp.294-295.

Mittemeijer, E., 2013. Modern Diffraction Methods. Weinheim: Wiley-VCH Verlag.

Mullerova, I. and Konvalina, I., 2009. Collection of secondary electrons in scanning electron microscopes. *Journal of Microscopy*, 236(3), pp.203-210.

Mullerova, I., Frank, L., Konvalina, I. and Mikmekova, E., 2018. Role of the Angular Distribution of Backscattered Electrons in Low Energy Scanning Electron Microscope. *Microscopy and Microanalysis*, 24(S1), pp.638-639.

Novák, M., 2008. Monte Carlo simulation of energy loss of electrons backscattered from solid surfaces. *Surface Science*, 602(7), pp.1458-1465.

Padua, G. and Wang, Q., 2012. *Nanotechnology Research Methods For Foods And Bioproducts*. Ames, Iowa: Wiley-Blackwell.

Patiha, Heraldy, E., Hidayat, Y. and Firdaus, M., 2016. The langmuir isotherm adsorption equation: The monolayer approach. *IOP Conference Series: Materials Science and Engineering*, 107, p.012067.

Pelleg, J., 2013. *Mechanical Properties Of Materials*. Dordrecht: Springer.

Pickover, C., 2011. The Physics Book. New York: Sterling Pub.

Ridderbos, T., 1997. The Wheeler-Feynman absorber theory: A reinterpretation? *Foundations of Physics Letters*, 10(5), pp.473-486.

Rouquerol, F., Rouquerol, J., Sing, K.S.W., Llewellyn, P., Maurin, G., 2014. *Adsorption by Powders and Porous Solids. Principles, Methodology and Applications*. Second Edition. Elsevier Science.

Schatten, H., 2013. *Scanning Electron Microscopy For The Life Sciences*. Cambridge: Cambridge University Press.

Sing, K., 1985. Reporting physisorption data for gas/solid systems with special reference to the determination of surface area and porosity (Recommendations 1984). *Pure and Applied Chemistry*, 57(4), pp.603-619.

Stokes, D., 2008. *Principles And Practice Of Variable Pressure/Environmental Scanning Electron Microscopy (VP-ESEM)*. Oxford: Wiley-Blackwell.

Thomas, W. and Crittenden, B., 1998. *Adsorption Technology and Design.* Oxford: Butterworth-Heinemann.

Thommes, M., Kaneko, K., Neimark, A., Olivier, J., Rodriguez-Reinoso, F., Rouquerol, J. and Sing, K., 2015. Physisorption of gases, with special reference to the evaluation of surface area and pore size distribution (IUPAC Technical Report). Pure and Applied Chemistry, 87(9-10), pp.1051-1069.

Titus, D., Samuel, E. and Roopan, S., 2019. *Green Synthesis, Characterization And Applications Of Nanoparticles*. 1st ed. Elsevier Amsterdam, Netherlands: pp.303-319.

Wang, J., Salihi, E. and Šiller, L., 2017. Green reduction of graphene oxide using alanine. *Materials Science and Engineering: C*, 72, pp.1-6.

Wolstenholme, J., 2015. *Auger Electron Spectroscopy*. New York: Momentum Press.

Zhou, W. and Wang, Z., 2007. *Scanning Microscopy For Nanotechnology*. New York: Springer.

Chapter 3 Synthesis and characterization of water glass-based silica aerogels with graphene oxide

In order to enhance the mechanical properties of silica aerogels, the graphene oxide was added to into SiO_2 matrix as nanofiller to produce SiO_2-GO composite aerogels on the basis of sol-gel technology by using novel ambient pressure drying technique. Furthermore, this chapter investigates the production of silica and composite aerogels and how using GO affects the surface area, pore distribution and pore volume. XRD, SEM, FTIR, BET, BJH and uniaxial compression tests were used to characterize the synthesized monolithic and composite aerogels.

3.1 Synthesis of monolithic and composite silica aerogels

As mentioned in Chapter 2, aerogels are produced through the sol gel method. Hydrochloric acid (5 M) was added to the water glass, which has a ph of 12 based on the previous work (Kim *et al.,* 2020), as a catalyst to neutralise the sodium silicate so that hydrolysis occurred. Gelation was completed within 8 minutes, then it was soaked in deionised water for 24 hours for aging. After that, water was exchanged with sodium bicarbonate solution (4.4 gram for each 100 ml water). The gel was processed with a mixture of 6 ml TMCS and 100 ml ethanol for one day (Han *et al.,* 2018), soaked in ethanol for one day to remove unreacted TMCS and residual HCl and then washed with distilled water to remove salt which is generated during the reaction between TMCS and sodium bicarbonate. Lastly, the gel was soaked in ethanol for one more day and dried at 60 ºC for 24 hours to produce monolithic silica aerogels (see Figure 3.1).

The silica aerogel monoliths mixed with GO were generated by dispersing the GO suspension (distilled water + GO) in mixed solution, then the gel was formed by using hydrochloric acid as a catalysis. The residual processes to synthesize final Si-GO composite aerogels were same as the generation of monolithic pure silica aerogel.

Besides these aerogels, sodium silica aerogel was synthesized without novel APD method to demonstrate how the novel APD technique affect the surface area, pore distribution and pore volume. Firstly, 6 ml water glass and 30 ml distilled water was mixed. Secondly, the addition HCI (5 M) turned the sol into the gel. Then the gel was soaked in distilled water for 1 day for aging. Finally, the gel was dried at 60 ºC for 24 hours without treated with a mixture of TMCS and ethanol to produce monolithic silica aerogel.

Figure 3. 1 Silica aerogels produced from water glass by using novel APD method (Han et al., 2018).

3.2 Results and discussion

In this study, the recently developed APD mechanism that uses sodium bicarbonate solution to decrease capillary pressure has been examined (Han *et al.,* 2018). The wet gel was exposed to combination of sodium bicarbonate solution and TMCS that generates carbon dioxide within the bulk of silica and silica composite gels without surface modification. The carbon dioxide that is trapped in the wet gel opposes the capillary pressure, so that the pore shrinkage and collapse during the drying step is prevented due to the decrease of capillary pressure. The effect of GO on the structural properties of composite aerogels is studied by adding a different amount of GO. The sol-gel method was used to incorporate graphene oxide solution at the stage of gel formation, to ensure homogeneous dispersion of graphene oxide solution within the silica network by ultrasonic agitation. Silica aerogel composite, which includes the highest value of GO (0.2 wt%), required 30 mins to form hydrogel. The composite aerogel with the lowest GO wt% content (0.05) and the monolithic silica aerogel are gelated in 7 min. The delayed gelation time with the higher content of GO in gel could be because of the saturated adsorption of GO sheets in the silica matrix, therefore the hydrolysis and condensation reactions between siloxane chains are inhibited and gelation time retarded. The other reason could be that GO reacts with hydrolyzed silica particles.

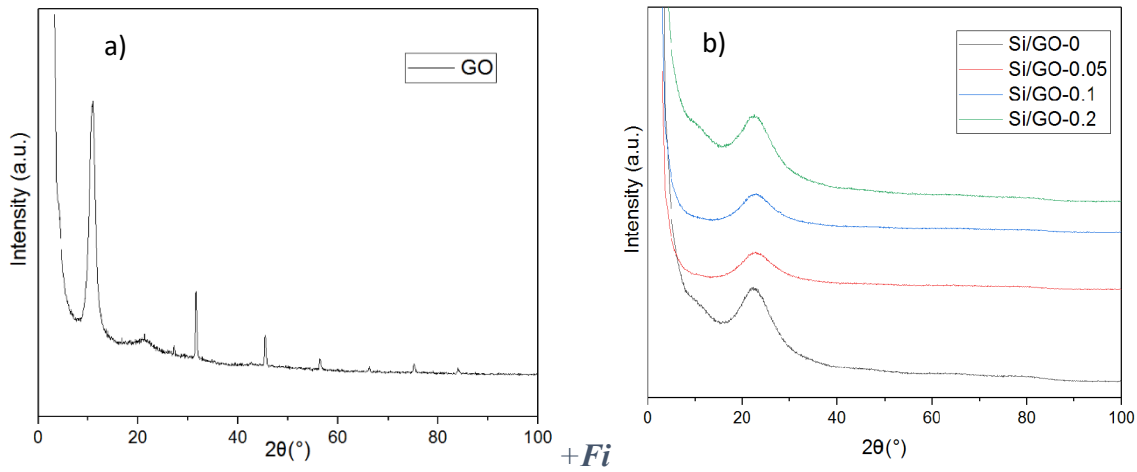

Figure 3. 2 XRD patterns of a) the pristine GO and b) Si-GO composite aerogels.

The XRD data for pure GO and silica aerogels and composites are shown in figure 3.2a and 3.2b, respectively. A sharp diffraction peak at 2θ = 11.3º (see Fig. 2a) is the characteristic peak of pristine GO (Guo *et al.*, 2015; Kuila *et al.,* 2012). At the same time, the characteristic peak has disappeared in Si-GO composite aerogels, see Fig. 2b, and an amorphous diffraction peak at 2θ = 22º is observed which is known characteristic peak of silica aerogel. The characteristic peak of pure GO is missing in composites because of the random distribution of GO within the silica matrix (Petit and Bandosz, 2009).

The surface morphology obtained by SEM of pristine GO and the composite aerogels is shown in figure 3.3. The pristine GO are large and smooth nanosheets with some wrinkles. Many oxygenated functional groups such as hydroxyl groups and carboxyl groups on the surface of the GO (Wang *et al.,* 2015; Yao *et al.,* 2015) could be advantageous for dispersion in the silica aerogel matrix and interaction with the silica matrix. Presence of GO nanosheets does not hinder the integrity of composite aerogels. The prepared composite aerogels have a rough structure and they become coarser as the GO loading increases (see figure 3.3).

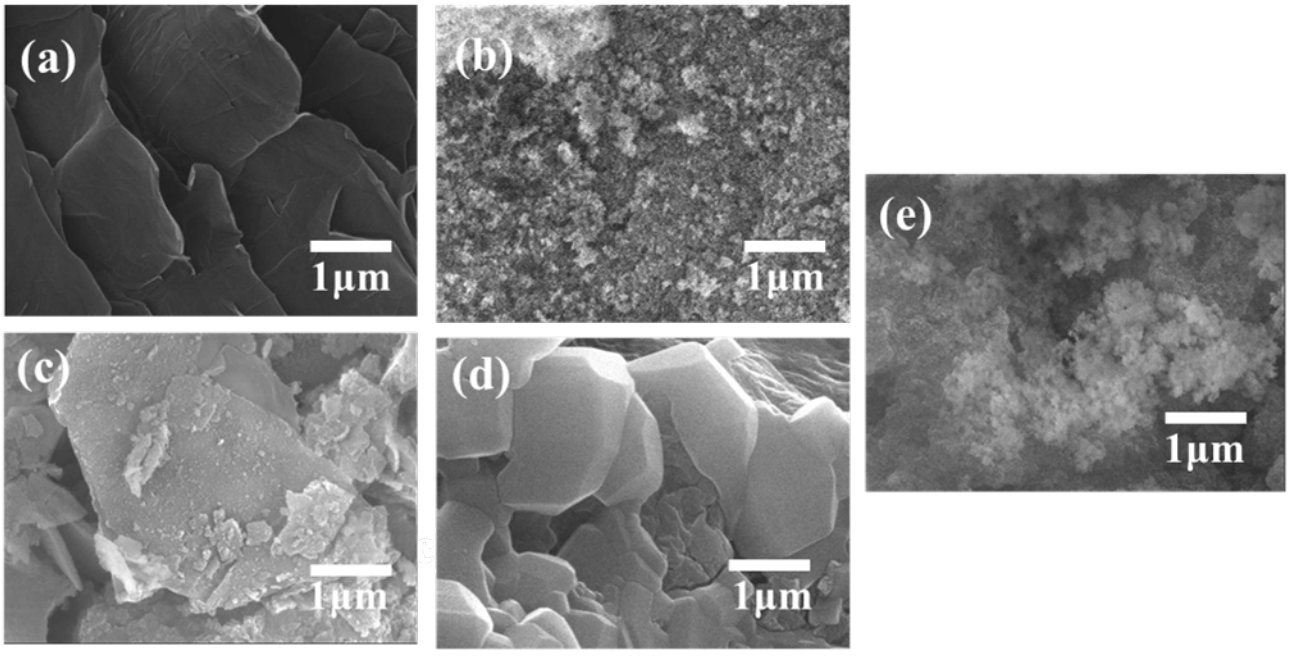

Figure 3. 3 SEM micrograps of (a) GO, (b) pure silica aerogel and Si-GO composite aerogels with different loading of GO (c) 0.5 wt%, (d) 0.1 wt%, (e) 0.2 wt%.

The FTIR spectrum of (a) GO and (b) Si/GO composite aerogels are shown in figure 3.4. The FTIR spectrum of GO showed the characteristic peaks of approximately 3400 and 1740 cm^{-1} corresponding to O-H and C=O stretching frequencies of the -COOH group, respectively (Jaafar *et al.,* 2019). Oxygen containing functional groups which are in the graphene oxide nanosheets do not appear when the GO nanosheets are added into the silica matrix. This can be because of chemical interaction between the silica particles and GO surfaces. In the FTIR spectrum of pure silica aerogels, the peak centred at 1087 cm^{-1}, 807 cm^{-1}, and 473 cm^{-1} are the

main characteristic peaks which are Si-O-Si bands of silica aerogels. Silanol groups are seen at 950 cm^{-1} (Ocaña, Fornés and Serna, 1989). The peak around 3000 cm^{-1} is assigned to alkyl groups due to the remaining non-hydrolyzed ethoxysilane groups or residual slight solvent [35, 36]. With the addition of GO nanosheets, the relative intensity of silanol groups at 1083 cm^{-1} on the silica matrix decrease. This can be due to the interaction with the oxygen-containing groups on the GO nanosheets during the sol gel process, and therefore the relative intensity of Si-O-Si groups in composite aerogels become weaker [26]. However, the relative intensity of silanol groups for Si/GO composite aerogel with 0.2 wt% GO shows slight increase.

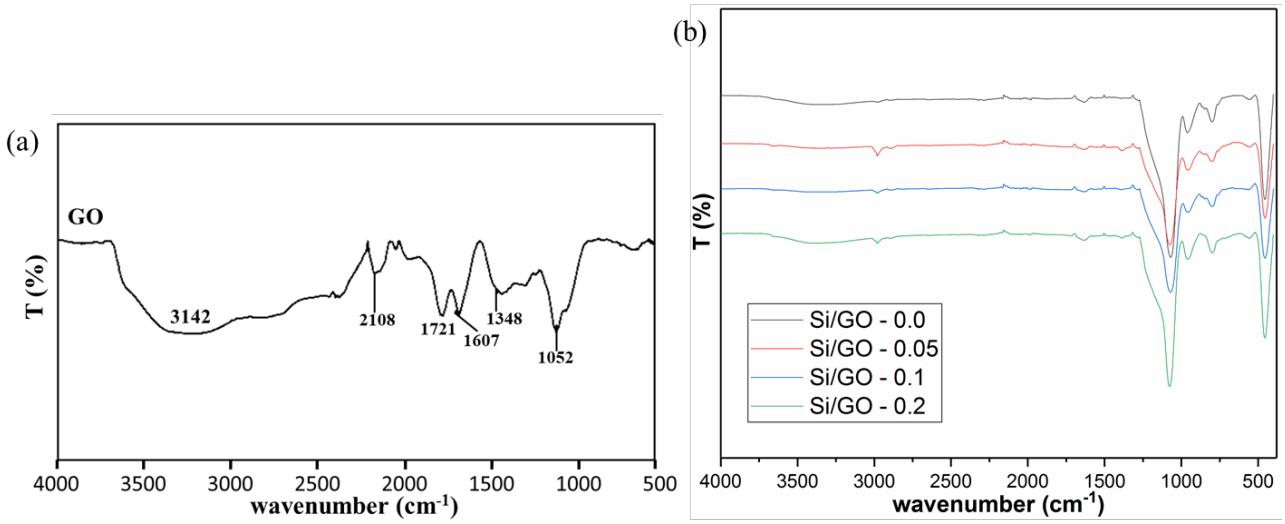

Figure 3. 4 FTIR spectrum of (a) GO and (b) pure silica aerogels and Si/GO composite aerogels.

Table 3 Pore properties of monolithic and composite Si/GO aerogels.

Samples	SiO_2-GO (0.0)	SiO_2-GO (0.05)	SiO_2-GO (0.1)	SiO_2-GO (0.2)
S_{BET} (m^2/g)	550	563	578	541
V_{total} (cm^3/g)	1.08	0.94	0.98	1.05
$R_{average}$(nm)	8.33	6.81	6.45	11.32

Table 3 shows the pore properties of aerogels. The specific surface area of pure silica aerogel (550 m^2/g) is higher than the specific surface area of Si/GO composite aerogels with 0.2 wt% GO due to the slight increase of total pore volume and small size of pores. The specific surface area of Si/GO composite aerogel with 0.1 wt% GO has the highest specific surface area, the reason about that can be relatively small-sized pores and relatively high total pore volume. The total pore volume of silica composite aerogels slightly increases this can be because of the increment of mesopore volume. However, Si/GO composite aerogel with 0.2 wt% GO has the lowest specific surface area, due to the increase in the amount of graphene oxide, which may

not be dispersed well in the silica matrix as a result it could restack or agglomerate and therefore lead to reduction in specific surface area.

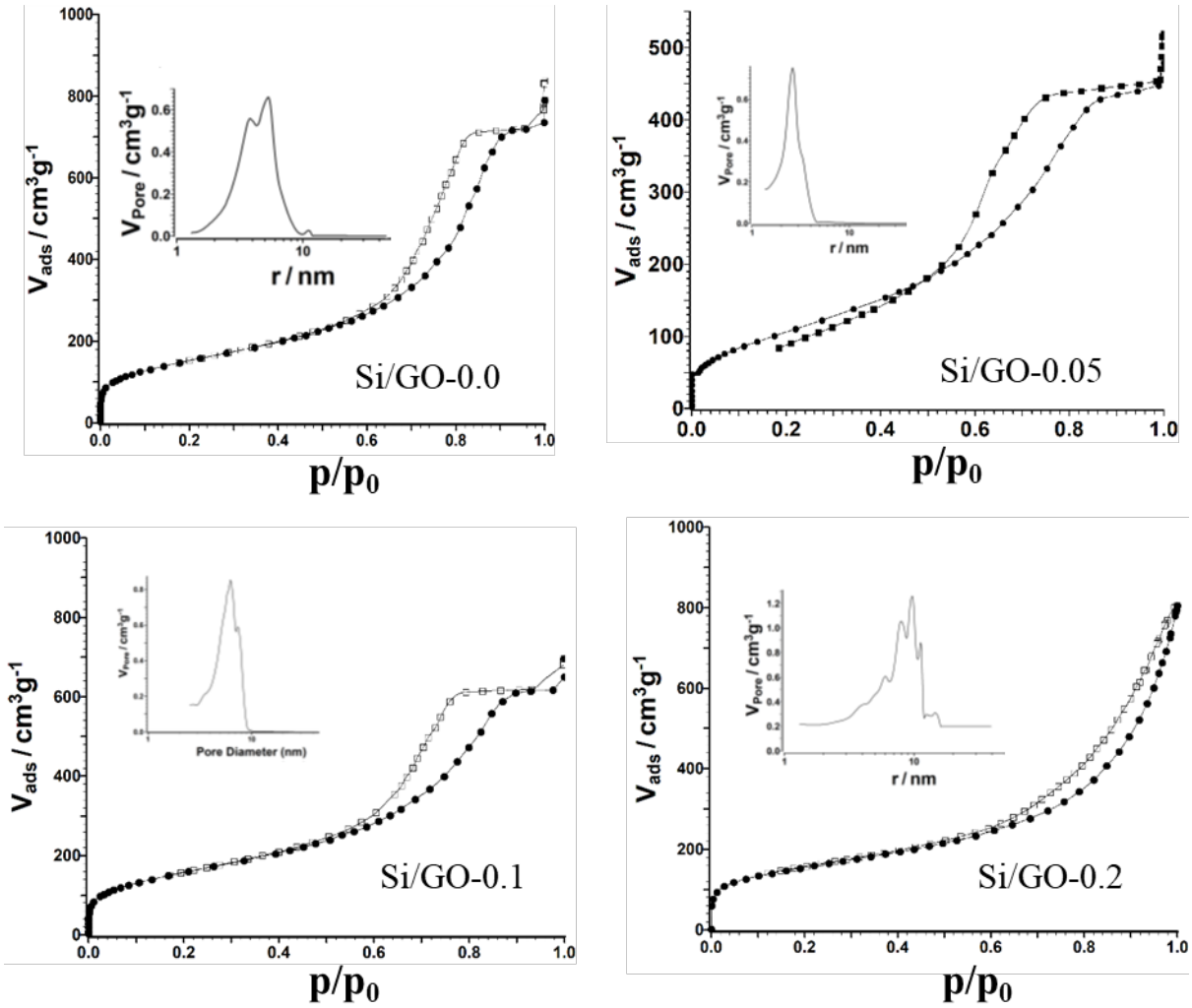

Figure 3. 5 Nitrogen adsorption-desorption isotherms and pore-size distributions of the monolithic and composite Si/GO aerogels.

The nitrogen adsorption – desorption isotherms for monolithic and composite aerogels are shown in figure 3.5. The isotherms of Si/GO composite aerogels are typical IUPAC type IV with hysteresis loops which is H2 type at the high relative pressure range because of the capillary condensation in mesopores (Sing, 1985).

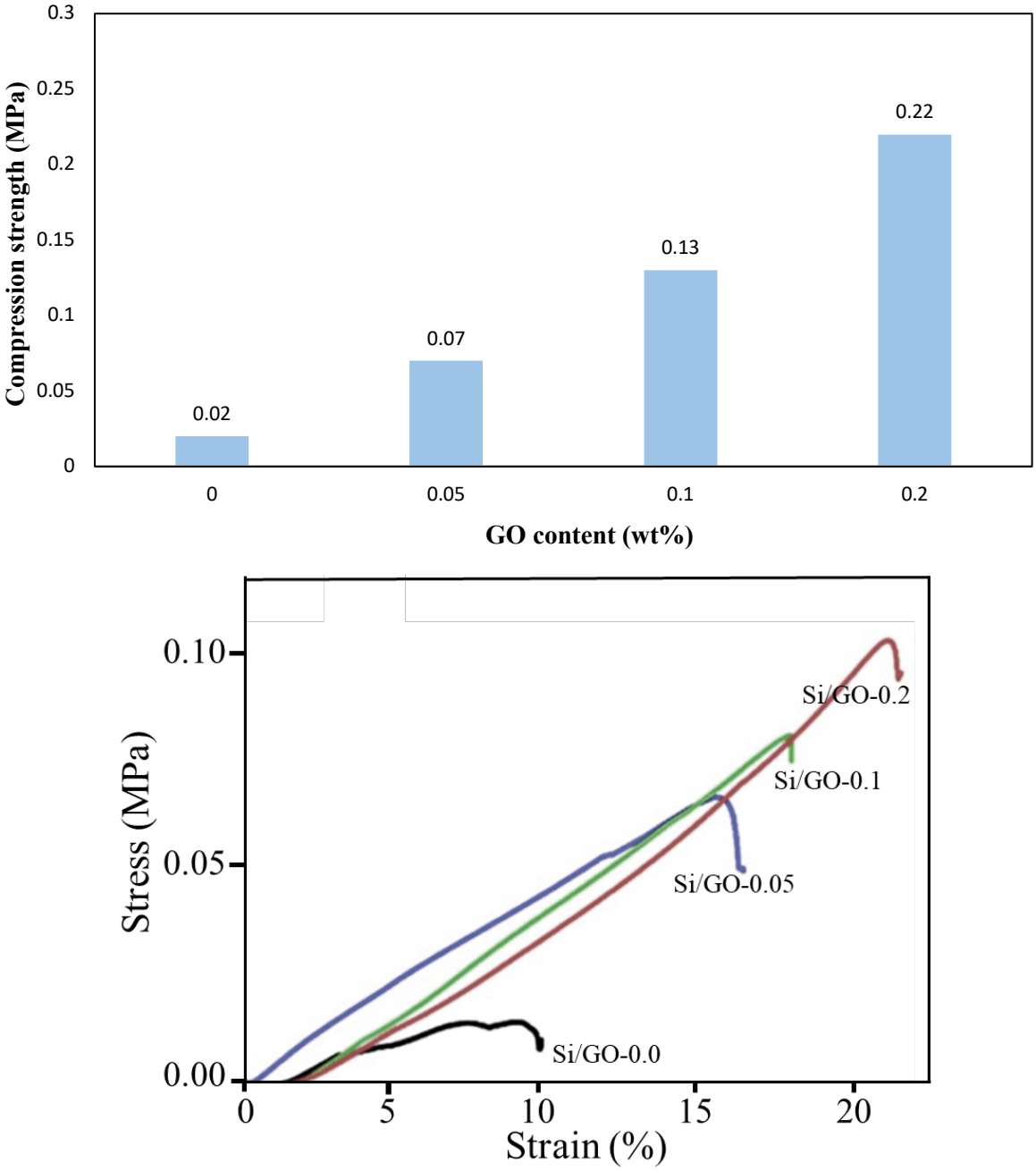

Figure 3. 6 Compressive strength and strain-stress curves of the monolithic and composite Si/GO aerogels

The mechanical strength of aerogels with GO addition is enhanced compared to that of the monolithic silica aerogel. As shown in figure 3.6, the pure silica aerogel showed compressive strength of 0.02 MPa. On the contrary, the GO/silica composite aerogels can resist higher stress. The compressive strength of GO/silica composite aerogels with 0.05 wt%, 0.1 wt%, 0.2 wt% is 0.07 MPa, 0.13 MPa, 0.22 MPa, respectively. That the addition of GO can improve mechanical strength of the composite aerogels is based on two aspects: firstly, the existence of GO can avoid further expansion of small cracks in aerogels because of its high mechanical strength.

Secondly, the GO nanosheets can prevent the crack to further propagate, which can deplete parts of fracture energy. This is convenient for the enhancement of mechanical strength. Lei et al. (2017) reported that the silica aerogel monoliths mixed with GO were fabricated by using supercritical drying method. The compressive modulus of Si/GO composite aerogels with 0.4 wt%, 1.0 wt%, 5.0 wt% of GO is 0.356 MPa, 0.361 MPa, 0.394 MPa, respectively (Lei *et al.,* 2017). The compressive strength of composite aerogels is higher than that of aerogels in our study. One of the reasons of the higher compressive strength can be usage of TEOS as a silica precursor, because TEOS provides the control of porosity, as a result of that stiffer structure can be obtained (Shahzamani *et al.,* 2016). The other reason can be supercritical drying method facilitates a much more uniform structure, so that produced aerogel exhibits better mechanical properties (Obrey, Wilson and Loy, 2011). Furthermore, the amounts of GO (0.4 wt%, 1.0 wt%, 5.0 wt%) have been used in the study of Lei et al. (2017) are higher than the amounts of GO (0.05 wt%, 0.1 wt%, 0.2 wt%) in our study. However, novel APD method (Han *et al.,* 2018) and waterglass as a silica precursor are much cheaper than supercritical drying method and TEOS as a silica precursor. In addition, with novel APD method and water glass as a silica precursor, Si/GO aerogels can be produced at large scale.

3.3 Conclusion

Monolithic and composite silica aerogels mixed with GO were successfully synthesized by using water glass as a precursor and sodium bicarbonate solution with TMCS. SiO2-GO composite aerogel with 0.1 wt% GO has the biggest surface area which is 578 m2/g, with an average pore diameter of 6.45 nm, and a pore volume of 0.98 cm3/g. The strong interaction between GO and silica matrix provides mechanical strength enhancements. The mechanical strength of aerogels is increased, and the aerogel composite displays toughness instead of traditional fragility.

References

Guo, K., Hu, Z., Song, H., Du, X., Zhong, L. and Chen, X., 2015. Low-density graphene/carbon composite aerogels prepared at ambient pressure with high mechanical strength and low thermal conductivity. *RSC Advances*, 5(7), pp.5197-5204.

Han, X., Hassan, K., Harvey, A., Kulijer, D., Oila, A., Hunt, M. and Šiller, L., 2018. Bioinspired Synthesis of Monolithic and Layered Aerogels. *Advanced Materials*, 30(23), p.1706294.

Jaafar, E., Kashif, M., Sahari, S. and Ngaini, Z., 2019. Effects of reduction temperatures on morphological, optical, and electrical properties of reduced graphene oxide (rGO) thin films. *Materials Today: Proceedings*, 16, pp.1702-1707.

Kuila, T., Bose, S., Khanra, P., Mishra, A., Kim, N. and Lee, J., 2012. A green approach for the reduction of graphene oxide by wild carrot root. *Carbon*, 50(3), pp.914-921.

Lei, Y., Hu, Z., Cao, B., Chen, X. and Song, H., 2017. Enhancements of thermal insulation and mechanical property of silica aerogel monoliths by mixing graphene oxide. *Materials Chemistry and Physics*, 187, pp.183-190.

Obrey, K., Wilson, K. and Loy, D., 2011. Enhancing mechanical properties of silica aerogels. *Journal of Non-Crystalline Solids*, 357(19-20), pp.3435-3441.

Ocaña, M., Fornés, V. and Serna, C., 1989. The variability of the infrared powder spectrum of amorphous SiO2. *Journal of Non-Crystalline Solids*, 107(2-3), pp.187-192.

Orel, B., Ješe, R., Vilčnik, A. and Štangar, U., 2005. Hydrolysis and Solvolysis of Methyltriethoxysilane Catalyzed with HCl or Trifluoroacetic Acid: IR Spectroscopic and Surface Energy Studies. *Journal of Sol-Gel Science and Technology*, 34(3), pp.251-265.

Petit, C. and Bandosz, T., 2009. Graphite Oxide/Polyoxometalate Nanocomposites as Adsorbents of Ammonia. *The Journal of Physical Chemistry C*, 113(9), pp.3800-3809.

Shahzamani, M., Bagheri, R. and Masoomi, M., 2016. Synthesis of silica-polybutadiene hybrid aerogels: The effects of reaction conditions on physical and mechanical properties. *Journal of Non-Crystalline Solids*, 452, pp.325-335.

Sing, K., 1985. Reporting physisorption data for gas/solid systems with special reference to the determination of surface area and porosity (Recommendations 1984). *Pure and Applied Chemistry*, 57(4), pp.603-619.

Wang, Z., Shen, X., Akbari Garakani, M., Lin, X., Wu, Y., Liu, X., Sun, X. and Kim, J., 2015. Graphene Aerogel/Epoxy Composites with Exceptional Anisotropic Structure and Properties. *ACS Applied Materials & Interfaces*, 7(9), pp.5538-5549.

Yao, X., Yu, W., Xu, X., Chen, F. and Fu, Q., 2015. Amphiphilic, ultralight, and multifunctional graphene/nanofibrillated cellulose aerogel achieved by cation-induced gelation and chemical reduction. *Nanoscale*, 7(9), pp.3959-3964.

Zhong, L., Chen, X., Song, H., Guo, K. and Hu, Z., 2015. Highly flexible silica aerogels derived from methyltriethoxysilane and polydimethylsiloxane. *New Journal of Chemistry*, 39(10), pp.7832-7838.

Chapter 4 Preparation of reduced graphene oxide (rGO) aerogels doped with different metal and metalloid oxide nanoparticles to use as anode materials for lithium ion batteries

This chapter details how to synthesize different metal oxide nanoparticles such as GeO_2, $CoFe_2O_4$, and Fe_3O_4. Then these metal oxide nanoparticles are used as additives to obtain reduced graphene oxide (rGO) composite aerogels for the investigation of physical properties such as surface area, morphology, the chemical composition, and electrochemical measurements as an anode material for LIBs.

4.1 The principle of lithium ion (Li-ion) batteries

Li-ion cell operating theory is described as: Li-ions move between anode and cathode. Intercalation of Li-ion in batteries can happen only during the charging and discharging process. As other batteries, a lithium-ion battery has a positive electrode, a negative electrode, a separator and electrolytes. During discharge, the positive lithium ion passes from the negative electrode and reaches the positive electrode through the electrolyte solution (made of organic solvent in solid or liquid form such as lithium hexafluorophosphate ($LiPF_6$) salt dissolved in organic carbonates). During charging, the complete opposite of the process above takes place, which is why the process is regarded as a reversible. The main purpose of the separator is to avoid a physical contact between the anode and cathode while facilitating ion transport in the cell (Makhov and Ivanishchev, 2020). A short illustration of a lithium ion battery cell is illustrated in Figure 4.1 (Gao *et al.,* 2016).

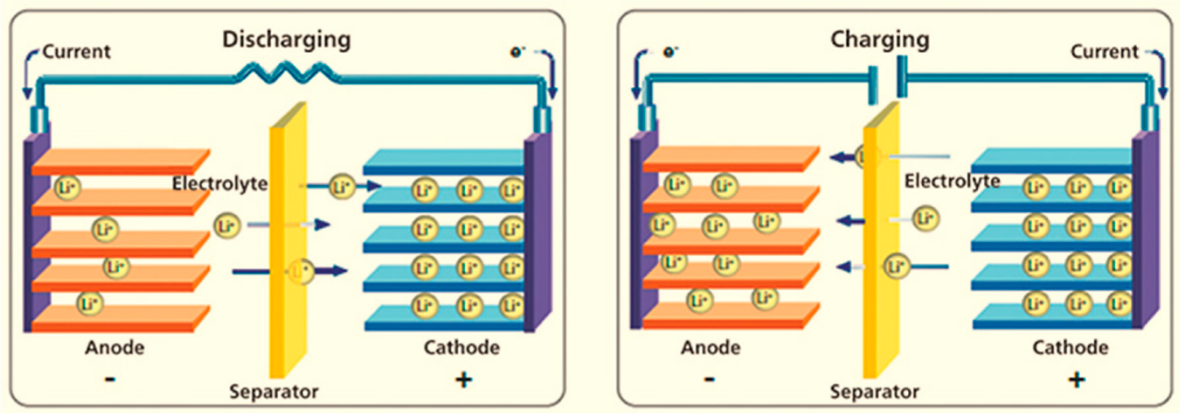

Figure 4. 1 The scheme of a lithium ion battery cell (Gao et al., 2016).

Li-ion cells need to have thermodynamically stable configuration in such a way that Goodenough and Kim (2010) describe it in an open-circuit energy diagram of an aqueous electrolyte systems. Figure 4.2 displays their research in a diagram. They determine parameters μA and μC as anode and cathode electrochemical potentials, respectively. If the passivation

layer provides no limit to electron transfer from the anode to the electrolyte, the electrolyte is decreased by μA above the lowest unoccupied molecular orbital (LUMO). When a passivation layer does not hinder electron transfer from the electrolyte to the highest occupied molecular orbital (HOMO) to the cathode, the electrolyte oxidizes μC below the HOMO. μA and μC should be within the window of the electrolyte for thermodynamic stability. This forces the open circuit voltage (OCV or VOC) of battery cell to be smaller than E_g (Pecher *et al.,* 2016):

$$eVOC = \mu A - \mu C \leq E_g \quad (3.1)$$

where E_g is the energy difference of the electrolyte window and *e* is the magnitude of the electron charge. Li-ion cell has to be constructed in such way that (Goodenough and Kim, 2010): (1) an anode's electrochemical potential μA should match the electrolyte LUMO and a cathode's electrochemical potential μC needs to match to the HOMO of the electrolyte; (2) due to the change of the volume of the elctrode during the charge/discharge cycle, a stable passivating solid electrolyte interphase (SEI) layer needs to self-heal itself; (3) the SEI layer should also enable a rapid Li ion transfer between the electrode and the electrolyte without restricting electron transfer between the charge and the existing collector (Goodenough and Kim, 2010).

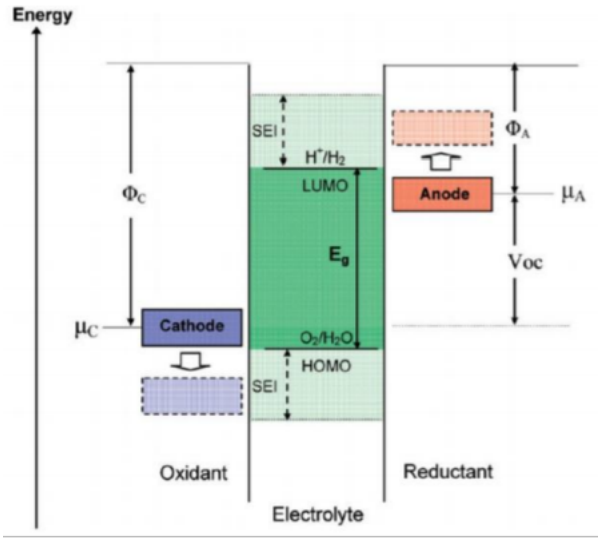

Figure 4. 2 Open-circuit energy diagram of an aqueous electrolyte systems (Goodenough and Kim, 2010).

As OCV is the difference between the Li ion chemical potentials of anode and cathode, or theoretically between their Fermi electron energy levels, a higher OCV is achieved by reducing the (de)lithiation potential of the anode. Given that Li metal has the most negative standard electrode potential among the metals, it can be utilised as the anode with the lowest potential for Li batteries. Nevertheless, if the output voltage of the anode is lower than 1V versus Li metal anode (Goodenough, 2014), the Fermi energy level of the anode is lower than LUMO of organic

electrolytic solutions. This decomposes the electrolytes and causes formation of a solid electrolyte interphase (SEI) layers.

4.1.1 Anode active materials for LIBs

An ideal LIB anode material can be described as (Qi *et al.,* 2017);

- Containing elements or compounds with low atomic or formula weights, being able to accommodate large amounts of Li, being cyclable, and having stable, and reversible gravimetric (mAh/g) and volumetric (mAh/cm^3) capacities. Although carbon in form of graphite contains a low atomic weight and low density, its reversible capacity is limited. Efforts to increase Li content to LiC_6 and to reversibly cycle it did not succeed (Qi *et al.,* 2017).
- Seeing potential similar to Li metal potential and not seeing major shift in potential with adjustments in Li content. This is because, when combined with a 4 V cathode, the overall working voltage of the LIB will not be much lower than 4 V.
- Anode should not be soluble in electrolyte solvents and chemically interact with salt or electrolyte solvents because the SEI protects the LiC_6, which is a strong reducing agent, from coming into direct contact with the solvents of the electrolyte and thereby suppresses the unwanted side reactions.
- Anode should show good electronic and Li ionic conductivity,
- Anode should be cheap and environmentally friendly (Reddy *et al.,* 2013)

In addition to this, when improving new anode materials, structure, composition, and morphology of anode materials should be in consideration which can be classified as insertion, alloying and conversion materials (Fang *et al.,* 2019).

The insertion process of anode materials occurs with the intercalation of Li^+ at vacancies in the structure of electrode materials without damaging the crystal structure. Nevertheless, there may be minor modifications which is called as a topotactic reaction in the crystal structure. Three conditions are required for this reaction. Firstly, the material needs to be crystalline and the host structure needs to have empty sites. The empty sites may be in the form of isolated vacancies, 1D channels, 2D layers or channels in the 3D network. Secondly, the host structure must comprise a transition metal or rare earth metal. Last, host structure may have unfavourable crystal structure and transition metals in low valency state may result with no Li intercalation. Consequently, semiconducting, or insulating metal oxides, transition metal ions, and 2D or 3D structures are required for Li cycling (Battistel *et al.,* 2020).

For alloying-based anode materials, Li can make alloys with metals/semimetals by offering high capacity (Guo *et al.,* 2019). Nevertheless, Li alloying – dealloying reactions include major changes in the unit cell volume which damage the long-term Li cyclability because of the

electrochemical pulverization of the active material and lack of electrical contact between the particles and the current collector. For this issue to be mitigated, the usage of metal nanosized particles or oxides or other compounds (Liu *et al.,* 2019), the inclusion of electrically active or inactive matrix elements towards Li, initial crystal structure and morphology and lastly choice of the proper voltage range for Li cycling can be adapted (Jin *et al.,* 2019).

Conversion reaction-based process takes place as lithium reacts with transition metal compounds (M_aX_b, M: metal, X: O, S, F, P, N etc.) to form Li_yX. Metals are reduced to their zero-oxidation state and have outstanding capacity values (Du *et al.,* 2018; Zhan *et al.,* 2018). However, various problems regarding the conversion reactions remain poorly understood, involving the voltage hysteresis during charge/discharge processes (Pender *et al.,* 2020). The conversion systems have the large gap between the charge and discharge voltages and this gap has a thermodynamic origin. Researchers recently discovered that the structure of the M−X chemical bonds in the starting material (ionic versus covalent) is based on the material electronic behaviour (Pender *et al.,* 2020).

4.2 Production process of anode for LIBs

Lithium-ion cells are produced with the design of materials and electrochemical couples available specifically to their applications in terms of voltage, state of charge use, lifespan, and safety (Mohamed and Allam, 2020). The selection and cell design of electrochemical couples have a direct impact on energy ratios, power, and available energy (Cha et al., 2018). Therefore, it is important to maintain the mechanical integrity of electrodes over numerous charge and discharge cycles despite the mechanical stress which is introduced through volumetric changes of the active material and the electrical conductivity of electrode while providing a porous structure that is favourable for transporting ion (Song and Choe, 2019). In order to integrate the cells, an optimised manufacturing of electrodes is required. Electrodes are covered as slurries on a current collector foil comprising an active material (rGO and composite aerogels), binders, and conductive additives. In this process it is significant to be aware of the control of colloidal chemistry, adhesion, and solidification to get a formation with a sufficient porosity degree and compaction in the electrode that can affect battery performance (Kraytsberg and Ein-Eli, 2016). The pores are mainly dependent on the size and shape of the materials added such as active material particles and additives. Though mechanical integrity is attributed to the cohesion between particles and the adhesion of particles to the current collector (Baunach *et al.,* 2015; Haselrieder *et al.,* 2015; Westphal *et al.,* 2015), the distribution of carbon black in the film governs the electrical conductivity (Indrikova *et al.,* 2015). As we focus on the anode performance in this chapter, the preparation of slurry, lamination and drying processes for

electrode preparation will be discussed. Usually, anode sheets are produced by mixing, solving and/or dispersing active materials and additives in a solvent, casting a homogeneous wet film on the current collector and removing the solvent through convective drying (Jaiser *et al.,* 2017). The following procedure should be taken into consideration for a well-prepared electrode slurry (Kraytsberg and Ein-Eli, 2016):

- Dispersing the active material (AM)/carbon additive (CA) agglomerates,
- Reducing the size of AM/CA aggregates as much as possible.
- Removing the separation and agglomeration of AM, CA and a binder, and arranging the most favourable composition.
- To avoid the material degradation in the mixing, one need to maintain the most favourable structure and composition of the AM, CA and binder.

The processing stage of slurry has an effect on the morphology and efficiency of the electrodes according to the precursor slurry properties. Besides, this process is able to modify the structure of the electrode components (AM, CA and the binder) (Guo *et al.,* 2020).

In this study, 18 mg (90wt %) active materials which are synthesized reduced graphene oxide and composite aerogels, 1 mg (5wt %) PVDF as a binder, 1 mg (5wt %) carbon black (Super P,TIMCAL) as a conductive agent, and 1200μL NMP (N-methyl-2-pyrolidone, Fluka) for dissolving the PVDF (polyvinylidene fluoride, Aldrich) binder were mixed by vibrant mill (SPEX 8000) for 15 minutes to prepare the slurry. The vibrant milling took place in cylindrical containers called vials which contain balls. The milling balls were stainless steel with 6 mm in diameter. Those mills moved linearly by two-axial translations and their frequency was 20 Hertz. The mixture and balls occupied only 1/3 of the volume, the balls' speed was low to provide an efficient milling.

After the milling process, the resulting mixture was transferred onto a Ti current collector and vacuum-dried at 100º C overnight. The average electrode loading was 10 mg/cm^2.

4.3 Reduced graphene oxide composite aerogels as an anode for lithium ion batteries

Energy crisis is one of the biggest problems, which has received growing attention worldwide and requires solutions to predominantly two subjects: renewable energy resources and researching for effectual secondary energy sources (Gielen *et al.,* 2019; Malik *et al.,* 2019). After the sustainable energy is harvested from wind, water, sunlight, etc., convenient technologies for energy storage are required for available usage. Furthermore, an imminent revolution of electric vehicles (EVs) and hybrid electric vehicles (HEVs) has demanded major challenges for lithium-ion batteries, and it is the most commonly used energy storage appliance at the present time (Aiello, 2020). Although there is a very effective progress in recent years

not only in laboratory but also in real usage, there are still many problems that restrict the promotion of EVs and HEVs, e.g., driving distances, speed, and equipment (Sun *et al.,* 2020). Thereby, LIBs with high energy and power densities have gained an increasing demand. Since the energy density and power density of LIBs are highly dependent on the properties of electrode material, the improvement of electrode materials has been reviewed in recent years to enhance lithium-ion batteries (Zhang *et al.,* 2018; Fang *et al.,* 2019; Wang *et al.,* 2020).

Graphene is a typical 2D material which has a monolayer of sp^2 carbon atoms arranged into a honeycomb crystal structure and has already received great research interest because of its exceptional properties, such as high conductivity (6000 Scm^{-1}), large specific surface area (2630 $m^2\ g^{-1}$), and good mechanical strength (130 GPa) (Lee *et al.,* 2008; Zhang, 2015). These properties make graphene an attractive material for many applications, e.g., lithium ion batteries, supercapacitors, fuel cells, photovoltaic devices, photocatalysis and Raman enhancement (Chen, Song and Xue, 2015). In the field of LIBs, the graphene is not obtained as a pure graphene which contains a monolayer of carbon atoms but from graphene oxide (GO) or other carbon materials in most of the researches (Tiwari *et al.,* 2020; Zhu *et al.,* 2020). However, chemical vapour deposition (CVD) and some mechanical methods can be used to obtain pure graphene with perfect crystallinity, but poor yields make them impossible for practicable use in LIBs (Chen *et al.,* 2015)**.** Thus, reduced graphene oxide (rGO) is often the preferred material for its feasible mass production and its properties which come close to those of graphene (Feng *et al.,* 2020). The production of rGO usually begins with oxidation of graphite, which expands the distances between layers of graphite sheets (Brisebois and Siaj, 2020). While the electrical conductivity is improved during reduction when compared to GO, there are inevitable residual oxygen atoms and defects on the surface and edge of rGO that contribute to some loss of electrical conductivity when compared to graphene (Chen *et al.,* 2020).

When rGO is chosen as anode material, it shows much better performance than graphite because of its high specific surface area (Wu *et al.,* 2019). In addition to this, composite materials, which have the important synergistic effects that extensively advance the overall electrochemical performance in both cathode and anode materials for LIBs, have been preferably used (Qi *et al.,* 2017). Furthermore, composite materials with 3D structures such as rGO composite aerogels exhibit extraordinary rate capability and cyclic performance (Li *et al.,* 2019; Tarcan *et al.,* 2020).

$CoFe_2O_4$, GeO_2, Fe_3O_4 metal oxides nanoparticles are regarded as potential anode materials for LIBs due to their high reversible capacity, fast power capability, good safety, and long cycle life (Zeng *et al.,* 2015). However, these pristine metal oxide nanoparticles still struggle from serious pulverization and agglomeration problems during the repeated Li^+ insertion/extraction

process, which leads to a fast fade capability and low cycling stability, impeding its functional usage (Jana, Scheer and Polarz, 2017).

Conductive carbon matrices have been commonly used to resolve the above problems and handle to absorb volume changes and enhance the structural stability of these metal oxide nanoparticles. Zeng *et al*. (2015) reported that $CoFe_2O_4$/rGO composite aerogels show greatly improved rate capability and long-term stability without obvious capacity fading for 1000 cycles at high rates of up to 4.5 A g^{-1}. This electrode design would be carried out to other ferrites such as Fe_3O_4 which gives excellent electrochemical performances (Liang and Lu, 2020; Shi *et al.,* 2020). Yang *et al.* (2016) produced GeO_2/carbon fibres as an anode for lithium-ion batteries that display excellent cycling stability with a high reversible capacity of 838.93 mA hg^{-1} after 100 cycles at a current density of 50 mA g^{-1}. Chen *et al.* (2019) synthesized Ge/reduced graphene oxide (RGO) composite with a small size of Ge nanoparticles for the advanced anode materials of LIBs. The anodes based on Ge/RGO composite have displayed very high electrochemical performance in terms of specific capacity, rate capability and long-term cycling stability under high rates (Chen *et al.,* 2019).

Purpose of this work is to demonstrate a simple method for obtaining rGO aerogels doped with different metal oxide nanoparticles, GeO_2, $CoFe_2O_4$, and Fe_3O_4 by using supercritical drying method to overcome several of the limitations discussed above. In the literature, $CoFe_2O_4$ and Fe_3O_4 have been mostly used with freeze drying method followed by solvothermal method to obtain composite aerogels as anode materials for lithium-ion batteries. In addition to this, there is no work about reduced graphene oxide aerogels doped with GeO_2 nanoparticles. The properties of aerogels such as surface area, morphology, the chemical composition, and electrochemical measurements as an anode material for LIBs were investigated in this work.

4.4 Synthesis of metal oxide nanoparticles

4.4.1 Materials and characterization methods

All materials for the synthesis of reinforced reduced graphene oxide aerogels were used without any further treatment. Germanium tetrachloride ($GeCl_4$) and ethanol (99.99%; EtOH), diethyl ether (≥ 99.5 %) were purchased from Alfa Aesar. Chloride hexahydrate ($FeCl_3.6H_2O$), iron (II) chloride tetrahydrate ($FeCl_2.4H_2O$), ammonium hydroxide (NH_4OH; 28.0-30.0% NH_3 basis), sodium citrate tribasic dehydrate ($C_6H_5O_7.2H_2O.3Na$), Fe(III) acetylacetonate, Co(II) acetylacetonate, and 2-(2-(2-methoxyethoxy)-ethoxy)acetic acid, MEEAA, were supplied by Sigma Aldrich. Lastly, graphene oxide dispersion (5mg/mL in H_2O) was provided by Royal Elite in Shanghai, China.

X-ray diffraction (XRD) was carried out using PanalyticalX'pert Pro diffractometer with an X'Celerator area detector, and Cu Kα X-rays were used to investigate the crystal and amorphous structure. Raman spectroscopy was recorded by a Lambram HR Evolution spectrometer. Scanning electron microscopy (SEM) measurements were performed by a ZEISS LEO 1530 microscope operated at 5 kV. SEM images were taken on the surface. The specific surface area of the aerogels was determined by Brunauer-Emmet Teller (BET) method on a QuanttachromeAutosorbiQ. Prior to gas sorption analyses with nitrogen at 77 K, the samples were outgassed at 80°C for at least 18h.

All experiments were done by me in the Laboratory for Multifunctional Materials in the Department of Materials at ETH, Zurich.

4.4.2 Synthesis of GeO_2 nanoparticles

Germanium dioxide (GeO_2) nanostructures have two main polymorphs: hexagonal (trigonal) quartz-like structure and tetragonal (cubic) rutile-like structure (Micoulaut *et al*., 2006) which show unique and attractive physicochemical and optical properties for applications in optical, electronic and optoelectronic devices (Devyatykh *et al.,* 1980; Fleming, 1984; Wu *et al.,* 2001).

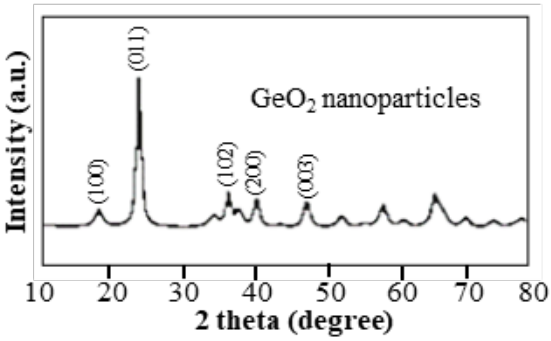

Figure 4. 3 XRD pattern of GeO_2 nanoparticles.

GeO_2 nanoparticles were synthesized as explained in the paper from Son *et al*. (2014). Firstly, the hexagonal GeO_2 nanoparticles with size 11 nm and deviation standard of ~20% were prepared by oxidization of $GeCl_4$ in water. 26 ml of absolute ethanol, 0.830 ml of de-ionized water and 0,1 ml of $GeCl_4$ were stirred in the ice bath for 10 hours for reaction time as control variables. Son et al. (2014) reported that the smaller GeO_2 nanoparticles can be produced in more nonpolar alcohol solvent, at lower concentrations, and lower temperature, because these experimental conditions provide a slow reaction rate for the nucleation of the particles (Son et al., 2014). The resulting product was centrifuged at 4000 rpm for 10 minute and washed with 40 ml diethyl ether 2 times then vacuum-dried overnight.

Figure 4.3 shows the powder X-ray diffraction (XRD) patterns of GeO_2 nanoparticles. The size of nanoparticles was calculated according to the Scherrer equation (4.1) (Patterson, 1939). The diffraction patterns were indexed for pure hexagonal (α-quartz phase, trigonal system) with space group $P3_121$ (N° 152) and lattice constants of a = b = 4.9823424 Å, c = 5.642891 Å (Smith and Isaacs, 1964).

$$\mathrm{B}\,(2\theta) = K\lambda/\mathrm{L} \cdot \cos\theta \tag{4.1}$$

4.4.3 Synthesis of Fe_3O_4 nanoparticles

Fe_3O_4 nanoparticles were synthesized as explained in the paper from Kim *et al*. (2015). Aqueous ferrofluid was produced by the modified co-precipitation method (Lim et al., 2010). Iron (III) chloride hexahydrate ($FeCl_3.6H_2O$, 7.3 g) and iron (II) chloride tetrahydrate ($FeCl_2.4H_2O$, 6g) were mixed with 25 ml of distilled water under stirring, then 35 ml of NH_4OH (28.0-30.0% NH_3 basis) was added and the colour of the iron oxide solution rapidly changed which demonstrates the onset of magnetites (Fe_3O_4) formation. When the solution colour turned into black, 100 ml of sodium citrate tribasic dehydrate ($C_6H_5O_7.2H_2O.3Na$, 1.0M) was added into the Fe_3O_4 solution to obtain citrate capped Fe_3O_4 particles.

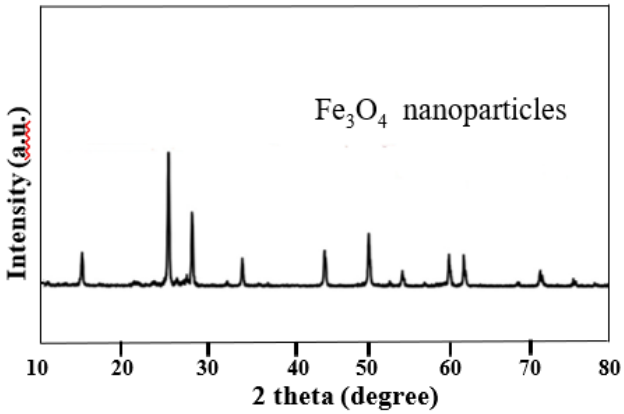

Figure 4. 4 XRD pattern of Fe_3O_4nanoparticles.

The X-ray (XRD) image of the produced Fe_3O_4 is demonstrated in Figure 4.4. Fe_3O_4 shows peak diffraction at 2θ = 24.1º, 33.4º, 50º, 54.1º, and 62.3º referring to the hexagonal phase of hematite (α–Fe_2O_3)(JCPDS card no. 33–0664). The nanoparticle size of Fe_3O_4 was 18 nm which was estimated by the Scherrer equation.

4.4.4 Synthesis of $CoFe_2O_4$ nanoparticles

2mmol Fe and 1 mmol Co were dissolved in 20 ml benzyl alcohol for 3 hours, then the solution was separated into 4 parts for microwave reaction at 195°C for 10 minutes to synthesize $CoFe_2O_4$. The obtained solution was separated into 2 parts and diethyl ether was added to wash. The solution was centrifuged at 4000 rpm for 15 minutes 4 times. After centrifugation, the

obtained precipitate was dispersed in Milli-Q water containing 2-(2-(2-methoxyethoxy)-ethoxy) acetic acid, MEEAA, and ultrasonicated for 2h until a stable dispersion formed. In the end, homogeneous dispersion without precipitate was achieved (Zeng *et al*., 2015).

After rinsing and drying, a black powder was synthesized, then it was identified by powder X-ray diffraction (see Figure 4.5). The crystalline size of $CoFe_2O_4$ which was measured to be 7nm was calculated from the (400) and (440) reflections (Malinowska *et al.,* 2020) by using the Scherrer equation.

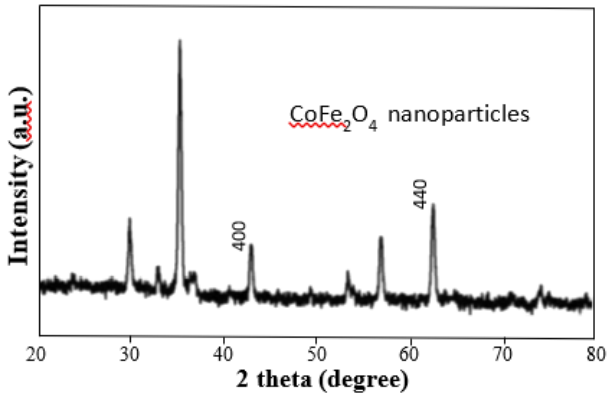

Figure 4. 5 XRD pattern of $CoFe_2O_4$ nanoparticles.

4.5 Synthesis of rGO and composite aerogels

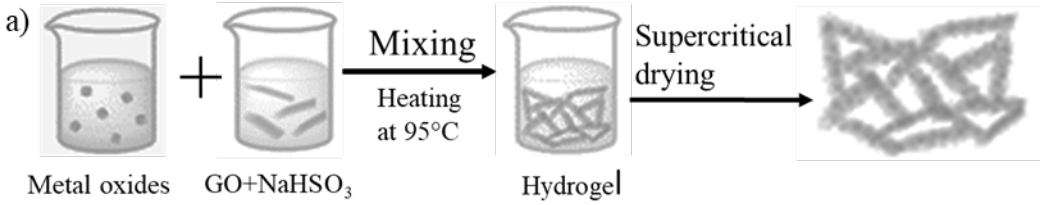

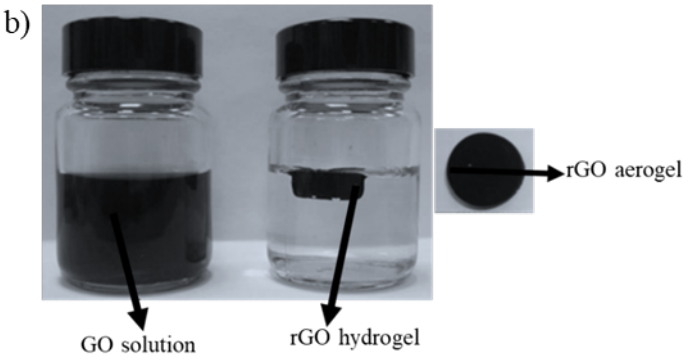

Figure 4. 6 Synthesis scheme of a) rGO aerogel and b) digital photographs of GO solution and rGO aerogel.

The optimum GO concentration was 5mg/mL because the shape and volume of the as-prepared reduced graphene oxide aerogel remained almost the same as original reduced graphene oxide

hydrogel. First of all, 5 ml commercial GO solution was sonicated for 30 minutes, then 300mg of sodium bisulfide ($NaHSO_3$) as the reducing agent was added and the solution was placed in a sonication bath for 5 min. The resultant slurry was then heated in an oven at 95°C for 6 h. The reduced graphene oxide hydrogel was washed by water, then methanol was used to remove the remnant $NaHSO_3$ in the samples. Lastly, the sample was soaked in large amount of acetone for complete solvent exchange, and then dried by supercritical CO_2 to produce rGO aerogel. In that process, the temperature and pressure are increased above the critical point of the pore liquid, following a path which makes the liquid a supercritical fluid without formation of a liquid-gas interface, so no capillary pressure develops in the pores (Kistler, 1932) as discussed in Chapter 1, section 1.2.1. Supercritical fluid is eliminated by depressurization while the temperature remains above the critical temperature, 42°C and 8.5 MPa. The pore liquid of wet gels which is acetone is exchanged with a fluid that has a lower critical point, which is carbon dioxide, CO_2, the critical point at 31°C and 7.38 MPa (Fábián *et al.,* 2019).

To prepare rGO composite aerogels, 7.5 mg of as prepared before metal oxide nanoparticles were added into the 5ml GO solution and then it was sonicated for 30 minutes. The remaining processes to synthesize rGO composite aerogels were the same as the production of a monolithic rGO aerogel. Metal and metalloid oxide nanoparticles weight percentages were 60wt% in rGO composite aerogels. Figure 4.6 demonstrates a diagram of the synthesis process of monolithic rGO aerogel by using supercritical drying technique.

Hydrogel Formation:

Initially, the chemical reaction between sodium bisulfide and GO sheets leads to the oxygen-containing groups to be gradually removed. Deoxygenation causes the hydrophilicity of GO sheets to convert into hydrophobicity. The GO sheets then isolate from the water and form a rGO hydrogel, which has a densely packed structure (Chen *et al.,* 2019). Hydrogel formation is discussed in more detail in chapter 5, page:115.

4.6 Electrochemical Test

Electrode Preparation:

The prepared composite aerogel on a Ti current collector was additionally vacuum-dried at 100º C and directly used as electrode without any additives.

Electrochemical Measurements:

Electrodes were placed in Swagelok-type cells in an Ar-filled glovebox (H_2O, O_2 < 0.1 ppm). Li metal (99.9%, Alfa-Aesar) was used as both reference and counter electrode. A glass fiber separator was soaked with electrolyte (1 M $LiPF_6$ in 1:1 wt % ethylene carbonate (EC)/dimethyl

carbonate (DMC), Novolyte). All electrochemical measurements were performed by using a Biologic instrument (VMP3) at room temperature. The electrodes were cycled between 0.01 and 3 V vs Li/Li^+ at a constant current density of 100 mAg^{-1}. 1 C is defined as 1 Ag^{-1}.

4.7 Results and discussion

Reduced graphene oxide aerogels doped with different metal oxide nanoparticles were fabricated by using supercritical drying method. Colloidally stable nanoparticles were required, and they could be achieved through tailoring the surface chemistry. Then metal oxide nanoparticles were added into the GO solution. After supercritical drying, crack free aerogels were synthesized and directly used as the electrode without any additives. The shape of the composite aerogels depends on the shape of containers.

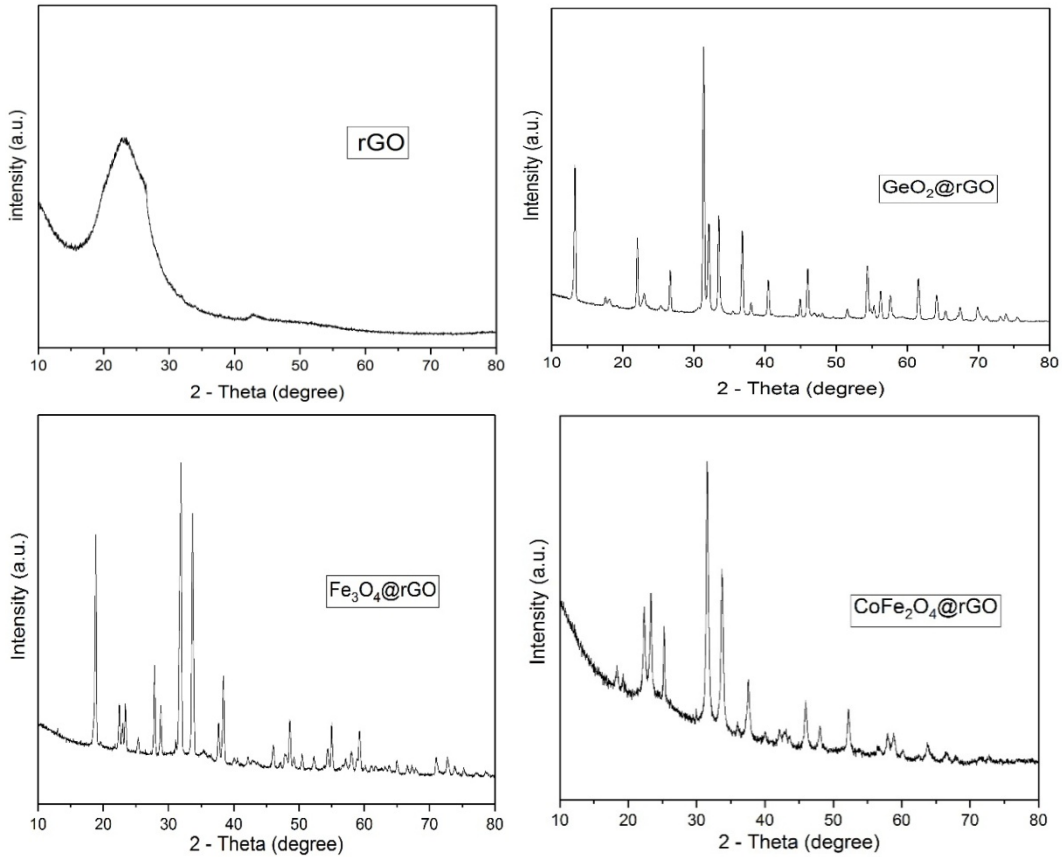

Figure 4. 7 XRD patterns of rGO and rGO@nanoparticles composite aerogels.

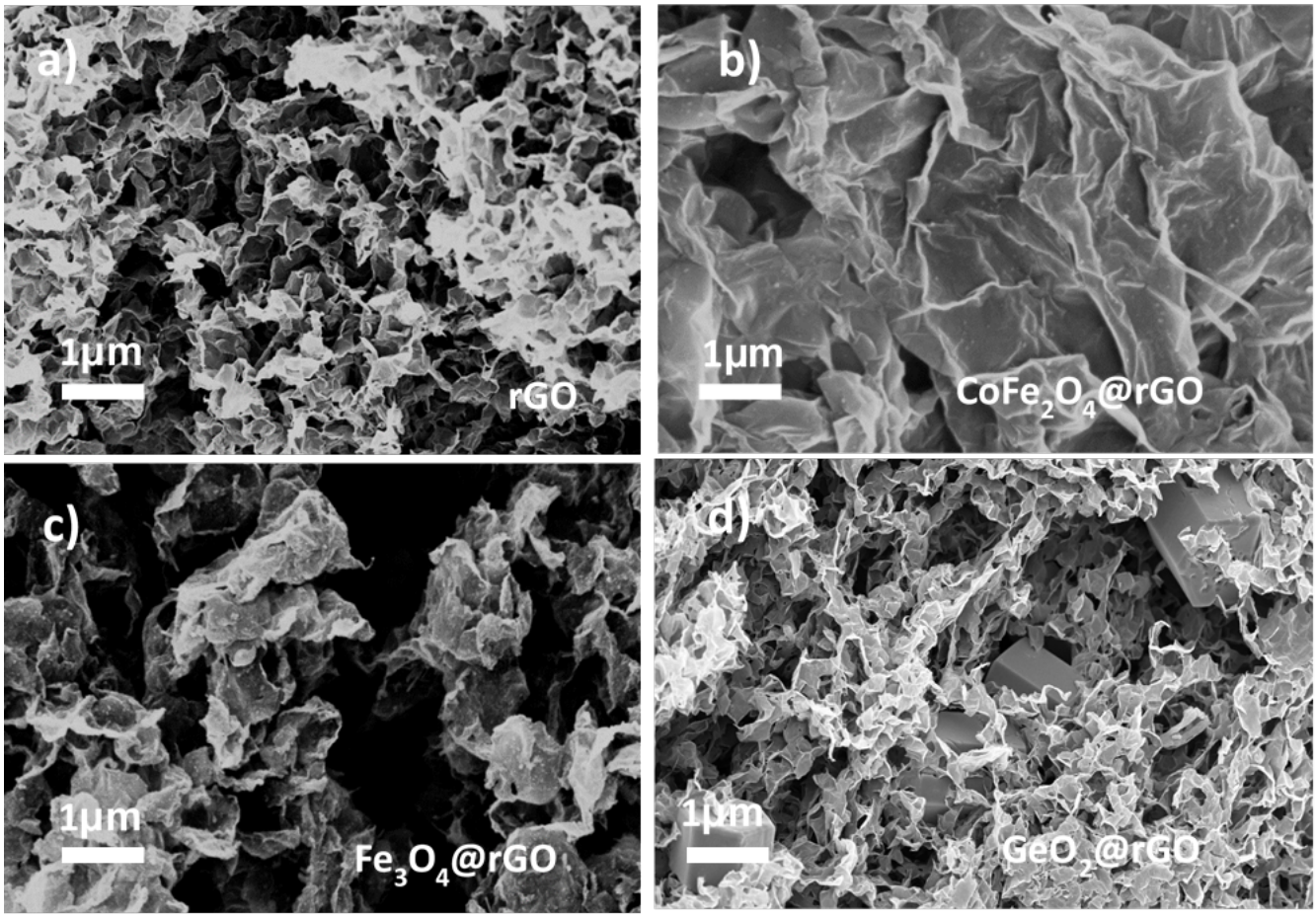

Figure 4. 8 SEM images of the rGO and rGO@nanoparticles composite aerogels.

X-ray diffraction (XRD) is applied to demonstrate the crystallinity and gained phase information for the prepared aerogels. Figure 4.7 presents the XRD pattern of the pure rGO and all composite aerogels in this work. After the reduction of GO, a new wide diffraction peak formed at 23.5°, corresponding to an interlayer spacing of 0.38nm, which is an indicative of the formation a poorly ordered graphite-like material (Aragaw, 2019). $CoFe_2O_4$@rGO composite aerogel shows the five main characteristic diffraction peaks at 30º, 35.4º, 43.1º, 57º and 62.6º are attributed to the (220), (311), (400), (511) and (440) planes of a face-centred cubic spinel $CoFe_2O_4$ (JCPDS No. 22-1086) (Xia *et al.,* 2012). For Fe_3O_4@rGO and GeO_2@rGO composite aerogels, the broad diffraction peak of rGO aerogel fades away. The reason can be that the face-to-face stacking is absent because of the large number of nanoparticles on both sides of reduced graphene oxide sheets.

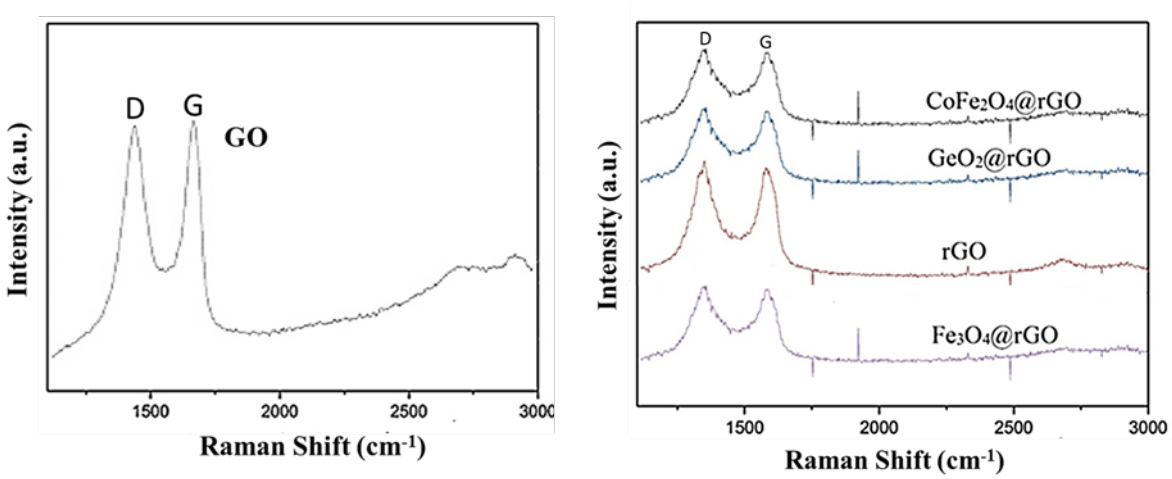

Figure 4. 9 Raman spectra of GO, monolithic rGO and composite aerogels.

Figure 4.8 shows the scanning of electron microscopy images of rGO and composite aerogels. The microscopic analysis indicates that the rGO and composite aerogels have a sponge like structure interconnected with macro-pores and extremely wrinkled surfaces of the cell wall. Metal oxide nanoparticles are anchored homogeneously on the graphene. The GeO_2@rGO aerogel was comprised of hexagonal GeO_2 sub-microparticles, wrinkled graphene nanosheets, in which the GeO_2 particles were homogeneously enwrapped.

Raman spectroscopy was used to discriminate between ordered and disordered graphene-based structures. Figure 4.9 demonstrates the Raman spectra representative of different locations corresponding to various areas of GO and aerogels. All Raman spectra of GO and aerogels displayed two intense peaks: The D band near 1340 cm−1 and the G band (about 1590 cm−1), typical of the carbonaceous materials (Paillet *et al.,* 2017). The D band was assigned to the radial motions of the carbon atoms on the aromatic rings and it is typically associated with local defects and disorder, in particular on the edges of graphene and graphite platelets (Akhavan, 2011; Hilder et al., 2012). The G line is generally allocated to a primary in-plane vibrational mode, an indicative of the movement of pairs of sp2 hybridized carbon–carbon bonds (Ferrari et al., 2006). The ratio of the intensities of the D/G bands for the rGO and composite aerogel are approximately 1.11, which is bigger than that for GO (0.93). The rise in the D/G ratio implies an increase in the number of sp2 domains in the rGO aerogel, which supports the reduction of GO (Chen, Li and Guo, 2011).

Type IV adsorption isotherm is observed for rGO aerogels in figure 4.10(a), which means that it is a mesoporous material. The specific surface area of rGO aerogel is 1225.035 m^2g^{-1} which is higher than those of most graphene-based porous materials. The pore size distribution (see Figure 4.10b) derived from desorption branch by the Barret-Joyner-Halenda method

demonstrates that most of the pores distribute within a range of 2 to 50 nm with a most probable pore diameter of roughly 18 nm.

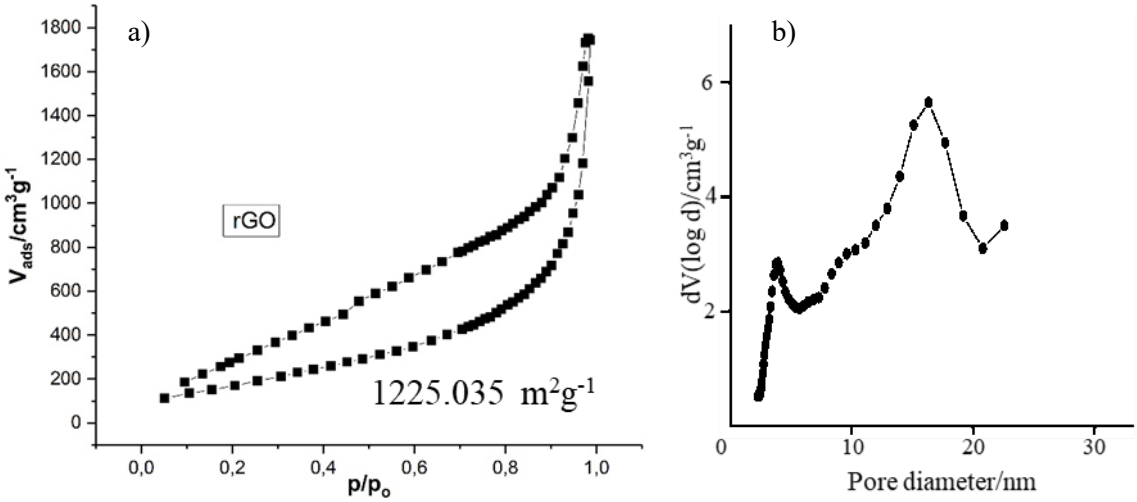

Figure 4. 10 (a) N_2 adsorption-desorption isotherms and (b) pore size distribution of rGO aerogel.

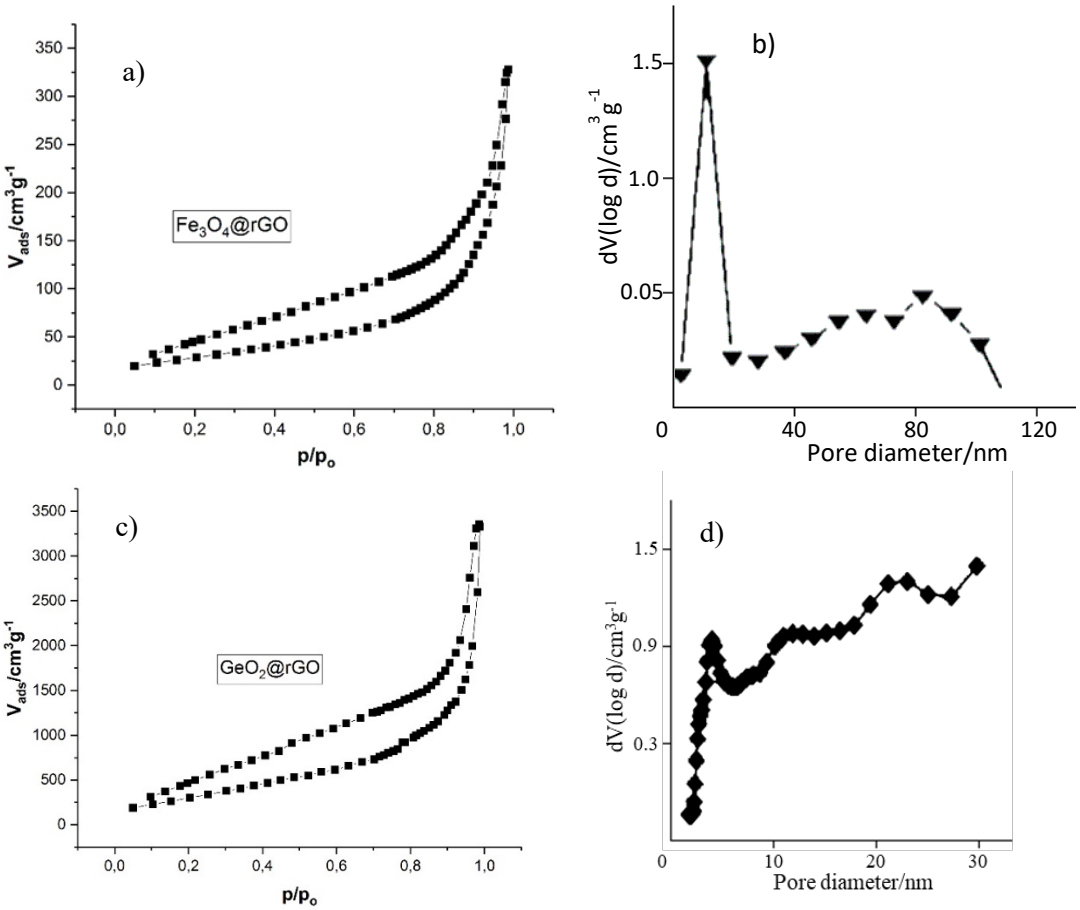

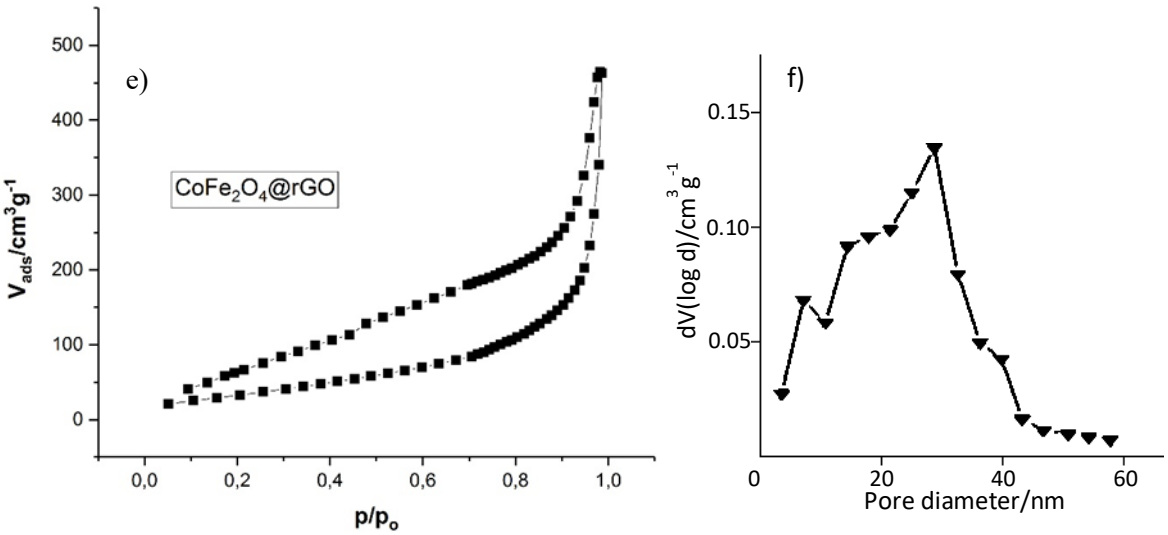

Figure 4. 11 (a, c, d) N_2 adsorption-desorption isotherms and (b, d, f) pore size distribution of Fe_3O_4@rGO, GeO_2@rGO and $CoFe_2O_4$ aerogels, respectively.

A Brunauer-Emmett-Teller (BET) analysis (see figure 4.11a) of nitrogen adsorption/desorption isotherms revealed that the specific surface area of Fe_3O_4@rGO composite aerogel is 278 m^2 g^{-1}, as well as considerable meso- and macroporosity as illustrated in Figure 4.11b. Compared to monolithic rGO aerogel, the surface area of Fe_3O_4@rGO composite aerogel decreased because of the large amount of Fe_3O_4. Moreover, it is convex inward, so there is no inflection point dependent on the nitrogen absorption desorption isotherm curve.

The specific surface area of 324.71 m^2g^{-1} for $CoFe_2O_4$@rGO composite aerogel together with meso- and macroporous features can be obtained by N_2 adsorption-desorption isotherm and BJH pore distribution, respectively (see Figure 4.11e, f). Like Fe_3O_4, the large amount of $CoFe_2O_4$ decreased the surface area of $CoFe_2O_4$@rGO composite aerogel.

Lastly, Brunauer–Emmett–Teller (BET) analysis was utilised to uncover the porous nature of the resulting GeO_2@rGO composite aerogel which has a large surface area, 672.242 m^2g^{-1}, with micro and mesoporosity (pore volume = 1.6 cm^3 g^{-1}) respectively, as demonstrated in Figure 4.13c, d.

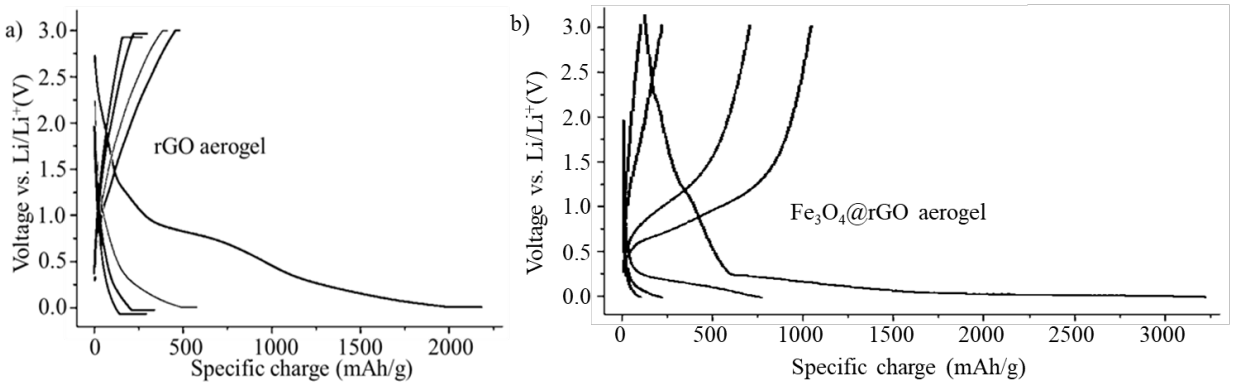

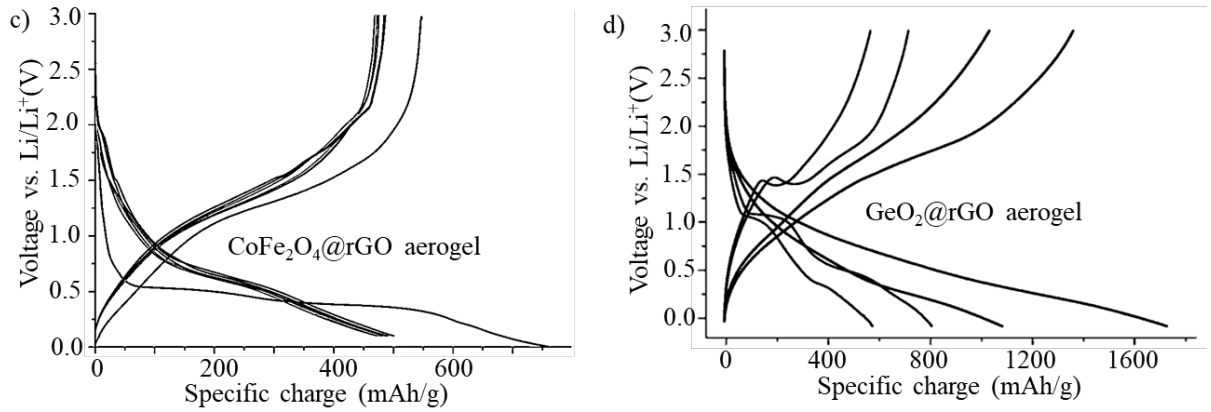

Figure 4. 12 Constant current + constant voltage (CC+CV) cycling graph for a) rGO aerogel, b) Fe_3O_4@rGO, c) $CoFe_2O_4$@rGO and d) GeO_2@rGO composite aerogels.

In figure 4.12 a, pure rGO aerogels without metal oxide nanoparticles have extremely high initial discharge capacity which is 2178 $mAhg^{-1}$, but the first capacity of de-lithiation is 471 $mAhg^{-1}$. After the first cycle, the total capacities maintain to fall on every cycle. After five cycles, it can only supply a capacity of 292 $mAhg^{-1}$ for discharge and 266 $mAhg^{-1}$ for charge. These charges are similar to graphite electrodes, demonstrating restacking of the rGO sheets to a graphite like structure (Yoo *et al.,* 2008). The loss of capacity can be explained by the formation of the solid electrode interphase (SEI) film in the first discharge process (Sathish *et al.,* 2012). Although, initial discharge capacity of Fe_3O_4@rGO aerogel was 3248 $mAhg^{-1}$, this value decreased to 758 $mAhg^{-1}$ in the second discharge (see figure 4.12 b). This situation indicates that the electrode is partially disintegrated after the first discharge and charging process of the electrode (Deshmukh *et al.,* 2020). This shows that the lithium-ion reaction does not occur reversibly. As shown in Figure 4.12 c, 752 $mAhg^{-1}$ of capacity was achieved for $CoFe_2O_4$@rGO aerogel in the first cycle. Large irreversible capacity loss was observed in the second cycle, which can be attributed to the interfacial reaction between the active material, the electrolyte and the phase change, which are common in the majority of hosts for lithium intercalation (Abdel Maksoud *et al.,* 2020). The first discharge capacity obtained for the GeO_2@rGO aerogel was 1768 $mAhg^{-1}$ but the capacity quickly fades during ongoing cycles.

4.8 Conclusion

In this chapter, the basic information about theory of lithium-ion batteries and anode active materials was reviewed. By using supercritical drying method, monolithic reduced graphene oxide and doped with different metal oxide nanoparticles aerogels were synthesized. $CoFe_2O_4$, Fe_3O_4, GeO_2 nanoparticles were produced by using different methods. Then, crystalline sizes of metal oxides were calculated from using XRD Bragg reflections by the Scherrer equation.

Furthermore, this review outlines how to prepare samples for electrochemical testing of aerogels as an anode material. According to BET analysis, which provides precise specific surface area for the evaluation of aerogels, Type IV adsorption isotherm is found for rGO aerogel. The rGO aerogel has the highest specific surface area, 1225.035 m^2g^{-1}, but loading with a large number of nanoparticles decrease the surface area of composite aerogels.

Lastly, electrochemical results as anode materials of aerogels were not as good as expected. The main reason can be that the ionic and electronic electrical conductivity of aerogels are comparatively inferior, leading to the low electronic transfer and ion diffusion efficiency, which might severely decline the electrochemical properties for Li-ion batteries as a semiconductor material (P. Pender et al., 2020). To solve this issue, annealing process should be carried out to remove the remaining oxygen which contains moieties in aerogel to raise the electrical conductivity.

References

Abdel Maksoud, M., Fahim, R., Shalan, A., Abd Elkodous, M., Olojede, S., Osman, A., Farrell, C., Al-Muhtaseb, A., Awed, A., Ashour, A. and Rooney, D., 2020. Advanced materials and technologies for supercapacitors used in energy conversion and storage: a review. *Environmental Chemistry Letters*.

Akhavan, O., 2011. Photocatalytic reduction of graphene oxides hybridized by ZnO nanoparticles in ethanol. *Carbon*, 49(1), pp.11-18.

Aragaw, B. (2019) Reduced graphene oxide-intercalated graphene oxide nano-hybrid for enhanced photoelectrochemical water reduction. *Journal of Nanostructure in Chemistry*, 10(1), pp. 9-18.

Aricò, A., Bruce, P., Scrosati, B., Tarascon, J. and van Schalkwijk, W., 2005. Nanostructured materials for advanced energy conversion and storage devices. *Nature Materials*, 4(5), pp.366-377.

Battistel, A., Palagonia, M., Brogioli, D., La Mantia, F., and Trócoli, R. (2020) Electrochemical Methods for Lithium Recovery: A Comprehensive and Critical Review. *Advanced Materials*, 32(23), p. 1905440.

Baunach, M., Jaiser, S., Schmelzle, S., Nirschl, H., Scharfer, P. and Schabel, W., 2015. Delamination behavior of lithium-ion battery anodes: Influence of drying temperature during electrode processing. *Drying Technology*, 34(4), pp.462-473.

Boyanov, S., Bernardi, J., Gillot, F., Dupont, L., Womes, M., Tarascon, J., Monconduit, L. and Doublet, M., 2006. FeP: Another Attractive Anode for the Li-Ion Battery Enlisting a Reversible Two-Step Insertion/Conversion Process. *Chemistry of Materials*, 18(15), pp.3531-3538.

Brisebois, P. and Siaj, M. (2020) Harvesting graphene oxide – years 1859 to 2019: a review of its structure, synthesis, properties and exfoliation. *Journal of Materials Chemistry C*, 8(5), pp. 1517-1547.

Cabana, J., Monconduit, L., Larcher, D. and Palacín, M., 2010. Beyond Intercalation-Based Li-Ion Batteries: The State of the Art and Challenges of Electrode Materials Reacting Through Conversion Reactions. *Advanced Materials*, 22(35), pp.E170-E192.

Chen, D., Li, L. and Guo, L., 2011. An environment-friendly preparation of reduced graphene oxide nanosheets via amino acid. *Nanotechnology*, 22(32), p.325601.

Chen, J., Li, H., Zhang, L., Du, C., Fang, T. and Hu, J., 2020. Direct Reduction of Graphene Oxide/Nanofibrillated Cellulose Composite Film and its Electrical Conductivity Research. *Scientific Reports*, 10(1).

Chen, K., Song, S. and Xue, D., 2015. Beyond graphene: materials chemistry toward high performance inorganic functional materials. *Journal of Materials Chemistry A*, 3(6), pp.2441-2453.

Chen, K., Sun, C. and Xue, D., 2015. Morphology engineering of high-performance binary oxide electrodes. *Physical Chemistry Chemical Physics*, 17(2), pp.732-750.

Deshmukh, A., Dwivedi, P., Nalawade, A., Qureshi, M. and Shelke, M., 2020. Highly durable Li-ion battery anode from Fe3O4 nanoparticles embedded in nitrogen-doped porous carbon with improved rate capabilities. *Journal of Materials Science*.

Devyatykh, G., Dianov, E., Karpychev, N., Mazavin, S., Mashinskiĭ, V., Neustruev, V., Nikolaĭchik, A., Prokhorov, A., Ritus, A., Sokolov, N. and Yushin, A., 1980. Material dispersion and Rayleigh scattering in glassy germanium dioxide, a substance with promising applications in low-loss optical fiber waveguides. *Soviet Journal of Quantum Electronics*, 10(7), pp.900-902.

Du, H., Huang, K., Li, M., Xia, Y., Sun, Y., Yu, M., and Geng, B. (2018) Gas template-assisted spray pyrolysis: A facile strategy to produce porous hollow Co3O4 with tunable porosity for high-performance lithium-ion battery anode materials. *Nano Research*, 11(3), pp. 1490-1499.

Fábián, B., Horvai, G., Idrissi, A., and Jedlovszky, P. (2019) Vapour-liquid equilibrium of acetone-CO2 mixtures of different compositions at the vicinity of the critical point. *Journal of CO2 Utilization*, 34, pp. 465-471.

Fang, S., Bresser, D. and Passerini, S., 2019. Transition Metal Oxide Anodes for Electrochemical Energy Storage in Lithium- and Sodium-Ion Batteries. *Advanced Energy Materials*, 10(1), p.1902485.

Fang, S., Bresser, D., and Passerini, S. (2019) Transition Metal Oxide Anodes for Electrochemical Energy Storage in Lithium- and Sodium-Ion Batteries. *Advanced Energy Materials*, 10(1), p. 1902485.

Feng, J., Ye, Y., Xiao, M., Wu, G., and Ke, Y. (2020) Synthetic routes of the reduced graphene oxide. *Chemical Papers*, 74(11), pp. 3767-3783.

Fleming, J., 1984. Dispersion in GeO_2–SiO_2 glasses. *Applied Optics*, 23(24), p.4486.

Gao, J., Shi, S. and Li, H., 2016. Brief overview of electrochemical potential in lithium ion batteries. *Chinese Physics B*, 25(1), p.018210.

Gielen, D., Boshell, F., Saygin, D., Bazilian, M., Wagner, N., and Gorini, R. (2019) The role of renewable energy in the global energy transformation. *Energy Strategy Reviews*, 24, pp. 38-50.

Goodenough, J., 2014. Electrochemical energy storage in a sustainable modern society. *Energy Environ. Sci.*, 7(1), pp.14-18.

Guo, J., Deng, Z., Yan, S., Lang, Y., Gong, J., Wang, L., and Liang, G. (2020) Preparation and electrochemical performance of LiNi0.5Mn1.5O4 spinels with different particle sizes and surface orientations as cathode materials for lithium-ion battery. *Journal of Materials Science*, 55(27), pp. 13157-13176.

Guo, X., Zhang, L., Ding, Y., Goodenough, J., and Yu, G. (2019) Room-temperature liquid metal and alloy systems for energy storage applications. *Energy & Environmental Science*, 12(9), pp. 2605-2619.

Haselrieder, W., Westphal, B., Bockholt, H., Diener, A., Höft, S. and Kwade, A., 2015. Measuring the coating adhesion strength of electrodes for lithium-ion batteries. *International Journal of Adhesion and Adhesives*, 60, pp.1-8.

Hilder, M., Winther-Jensen, O., Winther-Jensen, B. and MacFarlane, D., 2012. Graphene/zinc nanocomposites by electrochemical co-deposition. *Physical Chemistry Chemical Physics*, 14(40), p.14034.

Indrikova, M., Grunwald, S., Golks, F., Netz, A., Westphal, B. and Kwade, A., 2015. The Morphology of Battery Electrodes with the Focus of the Conductive Additives Paths. *Journal of The Electrochemical Society*, 162(10), pp.A2021-A2025.

Jaiser, S., Sanchez Salach, N., Baunach, M., Scharfer, P. and Schabel, W., 2017. Impact of drying conditions and wet film properties on adhesion and film solidification of lithium-ion battery anodes. *Drying Technology*, 35(15), pp.1807-1817.

Jana, A., Scheer, E. and Polarz, S., 2017. Synthesis of graphene–transition metal oxide hybrid nanoparticles and their application in various fields. *Beilstein Journal of Nanotechnology*, 8, pp.688-714.

Jin, J., Zheng, Y., Huang, S., Sun, P., Srikanth, N., Kong, L., Yan, Q., and Zhou, K. (2019) Directly anchoring 2D NiCo metal–organic frameworks on few-layer black phosphorus for advanced lithium-ion batteries. *Journal of Materials Chemistry A*, 7(2), pp. 783-790.

Kim, K., Kim, J., Lee, S. and Lee, J., 2015. Employment of Chitosan–linked Iron Oxides as Mesoporous Anode Materials for Improved Lithium–ion Batteries. *Electrochimica Acta*, 170, pp.146-153.

Kistler, S., 1932. Coherent Expanded Aerogels. *Rubber Chemistry and Technology*, 5(4), pp.600-603.

Kraytsberg, A. and Ein-Eli, Y., 2016. Conveying Advanced Li-ion Battery Materials into Practice The Impact of Electrode Slurry Preparation Skills. *Advanced Energy Materials*, 6(21), p.1600655.

Li, J., Yun, X., Hu, Z., Xi, L., Li, N., Tang, H., Lu, P., and Zhu, Y. (2019) Three-dimensional nitrogen and phosphorus co-doped carbon quantum dots/reduced graphene oxide composite

aerogels with a hierarchical porous structure as superior electrode materials for supercapacitors. *Journal of Materials Chemistry A*, 7(46), pp. 26311-26325.

Liang, Y. and Lu, W. (2020) Gamma-irradiation synthesis of Fe3O4/rGO nanocomposites as lithium-ion battery anodes. *Journal of Materials Science: Materials in Electronics*.

Licht, S., Douglas, A., Ren, J., Carter, R., Lefler, M. and Pint, C., 2016. Carbon Nanotubes Produced from Ambient Carbon Dioxide for Environmentally Sustainable Lithium-Ion and Sodium-Ion Battery Anodes. *ACS Central Science*, 2(3), pp.162-168.

Lim, S., Yang, D., Lee, W., (2010). Fabrication of magnetite–hydrogel nanocomposites with clustered magnetite cores and poly(N–isopropylacrylamide–co–acrylic acid) shells for drug delivery application. *J. Nanosci. Nanotechnol*., 10, p. 7295.

Liu, Z., Yuan, X., Zhang, S., Wang, J., Huang, Q., Yu, N., Zhu, Y., Fu, L., Wang, F., Chen, Y., and Wu, Y. (2019) Three-dimensional ordered porous electrode materials for electrochemical energy storage. *NPG Asia Materials*, 11(1).

Mahmood, N., Tang, T. and Hou, Y., 2016. Nanostructured Anode Materials for Lithium Ion Batteries: Progress, Challenge and Perspective. *Advanced Energy Materials*, 6(17), p.1600374.

Makhov, S. and Ivanishchev, A. (2020) Long-Term Cycling Behavior of Electrospun Separators for Lithium-Ion Batteries: A Comparison with Conventional Separators. *Energies*, 13(9), p. 2183.

Malik, K., Rahman, S., Khondaker, A., Abubakar, I., Aina, Y., and Hasan, M. (2019) Correction to: Renewable energy utilization to promote sustainability in GCC countries: policies, drivers, and barriers. *Environmental Science and Pollution Research*, 26(30), pp. 31550-31551.

Malinowska, I., Ryżyńska, Z., Mrotek, E., Klimczuk, T., and Zielińska-Jurek, A. (2020) Synthesis of CoFe2O4 Nanoparticles: The Effect of Ionic Strength, Concentration, and Precursor Type on Morphology and Magnetic Properties. *Journal of Nanomaterials*, 2020, pp. 1-12.

Micoulaut, M., Cormier, L. and Henderson, G., 2006. The structure of amorphous, crystalline and liquid GeO2. *Journal of Physics: Condensed Matter*, 18(45), pp.R753-R784.

Mohamed, N. and Allam, N. (2020) Recent advances in the design of cathode materials for Li-ion batteries. *RSC Advances*, 10(37), pp. 21662-21685.

P. Pender, J., Jha, G., Youn, D., Ziegler, J., Andoni, I., Choi, E., Heller, A., Dunn, B., Weiss, P., Penner*, R. and Mullins*, C., 2020. Electrode Degradation in Lithium-Ion Batteries. *Acs Nano*, pp.1243–1295.

Paillet, M., Parret, R., Sauvajol, J., and Colomban, P. (2017) Graphene and related 2D materials: An overview of the Raman studies. *Journal of Raman Spectroscopy*, 49(1), pp. 8-12.

Patterson, A., 1939. The Scherrer Formula for X-Ray Particle Size Determination. *Physical Review*, 56(10), pp.978-982.

Pecher, O., Carretero-González, J., Griffith, K. and Grey, C., 2016. Materials' Methods: NMR in Battery Research. *Chemistry of Materials*, 29(1), pp.213-242.

Poizot, P., Laruelle, S., Grugeon, S., Dupont, L. and Tarascon, J., 2000. Nano-sized transition-metal oxides as negative-electrode materials for lithium-ion batteries. *Nature*, 407(6803), pp.496-499.

Qi, W., Shapter, J., Wu, Q., Yin, T., Gao, G. and Cui, D., 2017. Nanostructured anode materials for lithium-ion batteries: principle, recent progress and future perspectives. *Journal of Materials Chemistry A*, 5(37), pp.19521-19540.

Qiao, W., Huang, W., Liu, Y., Li, X., Chen, L. and Tang, J., 2016. Photonics: Toward Scalable Flexible Nanomanufacturing for Photonic Structures and Devices (Adv. Mater. 47/2016). *Advanced Materials*, 28(47), pp.10344-10344.

Raccichini, R., Varzi, A., Passerini, S. and Scrosati, B., 2014. The role of graphene for electrochemical energy storage. *Nature Materials*, 14(3), pp.271-279.

Reddy, M., Subba Rao, G. and Chowdari, B., 2013. Metal Oxides and Oxysalts as Anode Materials for Li Ion Batteries. *Chemical Reviews*, 113(7), pp.5364-5457.

Rowsell, J., Pralong, V. and Nazar, L., 2001. Layered Lithium Iron Nitride: A Promising Anode Material for Li-Ion Batteries. *Journal of the American Chemical Society*, 123(35), pp.8598-8599.

Sathish, M., Tomai, T. and Honma, I., 2012. Graphene anchored with Fe_3O_4 nanoparticles as anode for enhanced Li-ion storage. *Journal of Power Sources*, 217, pp.85-91.

Schilde, C., Mages-Sauter, C., Kwade, A. and Schuchmann, H., 2011. Efficiency of different dispersing devices for dispersing nanosized silica and alumina. *Powder Technology*, 207(1-3), pp.353-361.

Shi, Y., Wang, K., Li, H., Wang, H., Li, X., Wu, X., Zhang, J., Xie, H., Su, Z., Wang, J., and Sun, H. (2020) Fe3O4 nanoflakes-RGO composites: A high rate anode material for lithium-ion batteries. *Applied Surface Science*, 511, p. 145465.

Smith, A., LaChance, A., Zeng, S., Liu, B. and Sun, L., 2019. Synthesis, properties, and applications of graphene oxide/reduced graphene oxide and their nanocomposites. *Nano Materials Science*, 1(1), pp.31-47.

Smith, G. and Isaacs, P., 1964. The crystal structure of quartz-like GeO2. *Acta Crystallographica*, 17(7), pp.842-846.

Son, Y., Park, M., Son, Y., Lee, J., Jang, J., Kim, Y. and Cho, J., 2014. Quantum Confinement and Its Related Effects on the Critical Size of GeO_2 Nanoparticles Anodes for Lithium Batteries. *Nano Letters*, 14(2), pp.1005-1010.

Sun, P., Bisschop, R., Niu, H., and Huang, X. (2020) Correction to: A Review of Battery Fires in Electric Vehicles. *Fire Technology*, 56(4), pp. 1411-1411.

Tiwari, S., Sahoo, S., Wang, N., and Huczko, A. (2020) Graphene research and their outputs: Status and prospect. *Journal of Science: Advanced Materials and Devices*, 5(1), pp. 10-29.

Wang, H., Yao, C., Nie, H., Wang, K., Zhong, Y., Chen, P., Mei, S. and Zhang, Q., 2020. Recent progress in carbonyl-based organic polymers as promising electrode materials for lithium-ion batteries (LIBs). *Journal of Materials Chemistry A*, 8(24), pp.11906-11922.

Wang, Q., Jiao, L., Du, H., Wang, Y. and Yuan, H., 2014. Fe_3O_4 nanoparticles grown on graphene as advanced electrode materials for supercapacitors. *Journal of Power Sources*, 245, pp.101-106.

Westphal, B., Bockholt, H., Gunther, T., Haselrieder, W. and Kwade, A., 2015. Influence of Convective Drying Parameters on Electrode Performance and Physical Electrode Properties. *ECS Transactions*, 64(22), pp.57-68.

Wu, J., Cao, Y., Zhao, H., Mao, J., and Guo, Z. (2019) The critical role of carbon in marrying silicon and graphite anodes for high-energy lithium-ion batteries. *Carbon Energy*, 1(1), pp. 57-76.

Wu, X., Song, W., Zhao, B., Sun, Y. and Du, J., 2001. Preparation and photoluminescence properties of crystalline GeO2 nanowires. *Chemical Physics Letters*, 349(3-4), pp.210-214.

Xia, H., Zhu, D., Fu, Y. and Wang, X., 2012. CoFe2O4-graphene nanocomposite as a high-capacity anode material for lithium-ion batteries. *Electrochimica Acta*, 83, pp.166-174.

Yang, Q., Sun, T., Yu, J. and Ma, J., 2016. Electrospinning of GeO2–C fibers and electrochemical application in lithium-ion batteries. *Chinese Chemical Letters*, 27(3), pp.412-416.

Yoo, E., Kim, J., Hosono, E., Zhou, H., Kudo, T. and Honma, I., 2008. Large Reversible Li Storage of Graphene Nanosheet Families for Use in Rechargeable Lithium Ion Batteries. *Nano Letters*, 8(8), pp.2277-2282.

Zeng, G., Shi, N., Hess, M., Chen, X., Cheng, W., Fan, T. and Niederberger, M., 2015. A General Method of Fabricating Flexible Spinel-Type Oxide/Reduced Graphene Oxide Nanocomposite Aerogels as Advanced Anodes for Lithium-Ion Batteries. *ACS Nano*, 9(4), pp.4227-4235.

Zhan, C., Wu, T., Lu, J., and Amine, K. (2018) Dissolution, migration, and deposition of transition metal ions in Li-ion batteries exemplified by Mn-based cathodes – a critical review. *Energy & Environmental Science*, 11(2), pp. 243-257.

Zhang, B., Ghimbeu, C., Laberty, C., Vix-Guterl, C. and Tarascon, J., 2015. Correlation Between Microstructure and Na Storage Behavior in Hard Carbon. *Advanced Energy Materials*, 6(1), p.1501588.

Zhang, H., 2015. Ultrathin Two-Dimensional Nanomaterials. *ACS Nano*, 9(10), pp.9451-9469.

Zhang, H., Zhao, H., Khan, M., Zou, W., Xu, J., Zhang, L. and Zhang, J., 2018. Recent progress in advanced electrode materials, separators and electrolytes for lithium batteries. *Journal of Materials Chemistry A*, 6(42), pp.20564-20620.

Zhu, J., Tu, W., Pan, H., Zhang, H., Liu, B., Cheng, Y., Deng, Z., and Zhang, H. (2020) Self-Templating Synthesis of Hollow Co3O4 Nanoparticles Embedded in N,S-Dual-Doped Reduced Graphene Oxide for Lithium Ion Batteries. *ACS Nano*, 1

Chapter 5 Preparation of reduced graphene oxide aerogels (rGO) by using ambient pressure drying (APD) method

The main purpose of this chapter is to explain the potential of large-scale and low-cost production of graphene aerogels by using ordinary instruments for the ambient pressure drying method with a different approach. This chapter presents results of characterisations such as XRD, SEM and Raman spectroscopy.

5.1 Ambient pressure dried reduced graphene oxide aerogels by using an ice-template method

Graphene, the one-atomic carbon atomic lattice, has extraordinary properties that are closely related to synthesising method. The graph sheets' defects and restacking problems weaken the perfect characteristics of ideal graphene, in particular electrical properties and high surface area. Three dimensional (3D) monoliths are developed in order to dissipate these drawbacks. Graphene sheet assemblies in 3D-structures not only preserve the basic properties of graphene, but also provide the advantages of high accessible surface area, interconnected channels, adjustable pore structure, and less aggregation (Chen, Zhu and Chen, 2018; Gürünlü *et al.,* 2020; Korkmaz and Kariper, 2020).

The key procedures for obtaining these arranged structures have been established based on direct gelation and self-assembly of functionalized graphene sheets. Aerogels are usually prepared by a wet chemical route such as sol-gel reaction but through different precursors and conditions. GO is the precursor material for the production of 3D graphene structures in most research studies. GO sheets can connect to obtain a 3D structure via reduction, addition of a cross-linking agent, or increase of the concentration of GO (Maleki, 2016; Gorgolis and Galiotis, 2017; Wasalathilake *et al.,* 2018).

The chemical and hydrothermal reductions are the most common techniques to synthesize graphene monolith from GO suspension. The chemical method is carried out at lower temperatures and pressure compared to hydrothermal reduction method. Consequently, equipment and requirements, both of which have unquestionable importance for practical applications, are much more available for chemical reduction than for thermal reduction (Salehabadi *et al.,* 2018; He *et al.,* 2019; Nosrati *et al.,* 2019).

The chemical reduction of the GO was usually achieved by using reducing agents such as hydrazine / hydrazine derivatives (Stankovich *et al.,* 2007; Park and Ruoff, 2010), sodium borohydride ($NaBH_4$) (Yang *et al.,* 2015). Therefore, an environmentally friendly, economical, and strong reducing agent is significant to produce high quality reduced graphene oxide (rGO). For industrial applications, green reducing agents such as formamidinesulfinic acid (FAS) (Ma

et al., 2013), l-ascorbic acid(L-AA), and sodium sulphide (Na_2SO_3) (He *et al.,* 2014) have been utilised. Chen et al. (2014) have used a diversity of sulfur-containing components and compared their reduction performance to other reductants' reduction performance. The results displayed that sodium bisulfide ($NaHSO_3$) is as effective as hydrazine to reduce graphene oxide. In addition to this, GO reduced by $NaHSO_3$ showed better electrical conductivity performance, approximately 27% higher than the ones reduced by hydrazine (Chua and Pumera, 2014). Besides all these, to produce a graphene aerogel with a well-defined form, the liquid inside gels must be replaced by air using a particular drying method, for example freeze drying or super-critical drying (Long *et al.,* 2018; Zu *et al.,* 2018) which could provide the dry sample with minimal distortion of structure. However, freeze drying and supercritical drying techniques that need special equipment are too laborious and expensive (Wang *et al.,* 2019; Geng *et al.,* 2020). On the contrary, the ambient pressure drying (APD) technique is quite convenient and energy-saving, without the use of special devices operating under high pressure, at ultra-low temperature or a vacuum environment (Yang *et al.,* 2015). Thus, the ambient drying technique is highly needed for large-scale and cheap industrial production of graphene aerogels.

In this study, ambient pressure dried graphene aerogels were synthesized by recasting a reduced graphene oxide (GO) hydrogel with an ice-template method.

5.2 Materials and characterization methods

Natural graphite flakes (99.8% purity) and sulphuric acid (98%) were purchased from VWR. Phosphoric acid (85%), dihydrogen dioxide (35%), potassium permanganate (99%), chlorotrimethylsilane (≥99%), and hydrochloric acid (37%) were purchased from Sigma. All reagents were used without further purification. Deionised (DI) water (18 MΩ/cm resistivity) from Nanopore purification system was used in all experiments. Ethanol (99.99%; EtOH), sodium bisulphite (≥58.5% SO_2; $NaHSO_3$) were purchased by Sigma Aldrich.

X-ray diffraction (XRD) was carried out using PanalyticalX'pert Pro diffractometer with an X'Celerator area detector and Cu Kα X-rays were used to investigate the crystal and amorphous morphology. Raman spectroscopy was recorded by a Lambram HR Evolution spectrometer. Scanning electron microscopy (SEM) measurements were performed by a ZEISS LEO 1530 microscope operated at 5 kV.

All experiments were done by me in the Laboratory for Multifunctional Materials in the Department of Materials at ETH, Zurich.

5.3 Synthesis of rGO aerogels

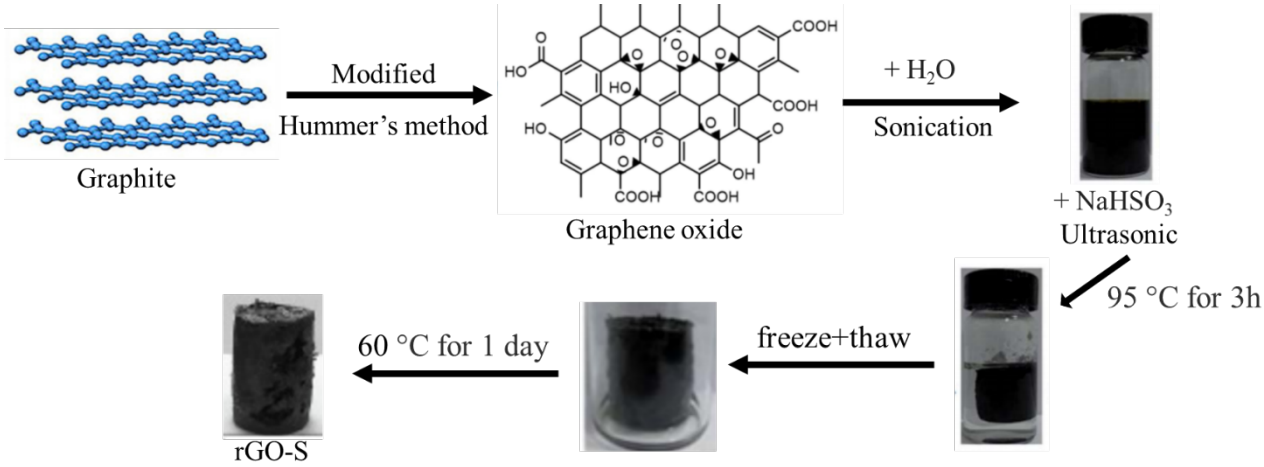

Figure 5. 1 Preparation of sulfenyl-reduced graphene aerogel (rGO-S).

The synthesis of the rGO is shown in Figure 5.1. Firstly, GO was obtained by using modified hummer methods (Wang, Salihi and Šiller, 2017) which is mentioned in chapter 2. 20 ml GO aqueous dispersion (40 mg GO sheets and 20 ml DI water) and 200 mg of $NaHSO_3$ was placed in an ultrasonic for 15 min. The resultant slurry was then heated at 95 °C for 3 h (Zhang *et al.,* 2018). To remove sulphate ion, hydrogel was washed with deionized water and refreshed every 4 hours for one day. After that, hydrogel was frozen in the fridge for 4 h at -18 ºC followed by thawing at room temperature. Then water was replaced by 200 ml ethanol for 24h. Finally, rGO hydrogel was dried on the heater at 60°C for 24h to obtain rGO aerogel.

5.4 Hydrogel formation

In the beginning, the chemical reaction between sodium bisulfide and GO sheets causes gradual removal of the oxygen-containing groups. It is common knowledge (Li *et al.,* 2020) that these functional groups lead to hydrophilic nature of GO sheets. When GO sheets begin to lose these moieties, the hydrophilicity turns into hydrophobicity because of deoxygenation. Then GO sheets isolate from water and shape a closely packed structure, known as rGO hydrogel (Chen *et al.,* 2019). The increase in the reduction level results in the increase of π-π interactions between conjugated rGO sheets, therefore hydrogel shrinks in dimensions (Shadkam *et al.,* 2020). The appropriate reduction time can be considered that the hydrogel is packed completely, and the shrinkage stops. A vessel-shaped hydrogel is floated in a clear solution in the end of the reduction (Chabot *et al.,* 2014; Xiong *et al.,* 2015).

5.5 Reduction mechanism

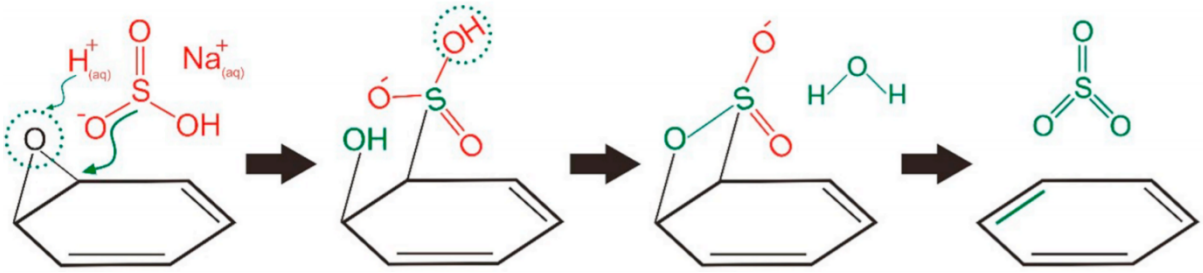

Figure 5. 2 Reduction mechanism using of $NaHSO_3$ as a reductant (Shadkam et al., 2020).

There are not many researches that show the reduction mechanism using $NaHSO_3$ as a reductant. It has been suggested that the sulphur-including reductants can open the epoxy ring and improve the de-epoxidation step of the reduction (Chen *et al.*, 2014). The process is illustrated schematically in Figure 5.2 (Shadkam *et al.,* 2020). The primary mechanism takes place upon dissociation of $NaHSO_3$ in aqueous media and the production of HSO_3^-. These ions attack the C-O bond and substitute the C-S bond. The free oxygen is then ready to protonate and give a water molecule. In the last stage of the reduction, SO_3 molecules are separated from reduced GO sheet and turned into soluble SO_4^{2-} ions, which can be easily washed out from the system. It is very beneficial that this material does not leave any by-products in the final hydrogel (Chen, Yan and Bangal, 2010; Wu *et al.,* 2019).

5.6 Results and discussion

Reduced graphene oxide aerogels were produced by using ambient pressure drying (APD) method. The aerogels synthesized via APD usually exhibited a severe shrinkage or collapse of the wet gel in volume after drying because of the capillary pressure (*P*) (Zhao *et al.,* 2012). The capillary pressure is associated with the contact angle (θ), surface tension of the pore liquid (γ) and pore radius (R), according to the equation below, Laplace formula (5.1) (Rowlinson and Widom, 2013):

$$P = \frac{2\gamma\cos\theta}{R} \tag{5.1}$$

From this equation, it is obviously found out that *P* is inversely proportional to the pore radius (R) if the contact angle (θ) and surface tension (γ) remain constant. Consequently, the enlargement of the pores of graphene gels will be an extremely effective way to reduce the capillary force (Yang *et al.,* 2015).

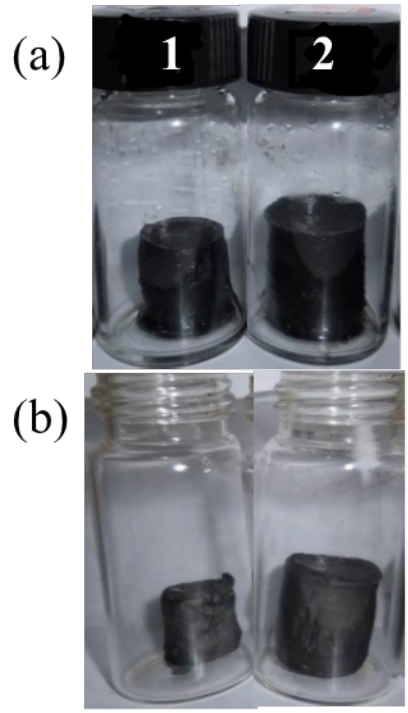

Table 5 Different reduction time to prepare rGO hydrogels

Reduction time	rGO-S hydrogels
6h	Sample 1
3h	Sample 2

Figure 5. 3 Digital images of the time-dependent formation process: (a) reduced graphene oxide hydrogel with different reduction times, (b) rGO-S aerogels after the freeze-thaw process.

It has been reported that, the higher cooling rates of freezing will result in smaller pore diameters (Qiu *et al.,* 2012). Therefore, in this study, slower cooling rates of freezing provide larger pore diameters. As illustrated in Figure 5.3, it is obviously seen that three hours is the optimal reduction time to prepare rGO-S aerogels. The shape and volume of the synthesized rGO-S aerogel has almost the same size as original rGO hydrogel. On the contrary, more reduction time (6h-sample1, see table 5) for synthesized rGO-S aerogels will cause more collapse or shrinkage. Because more reduction time results in mobility of GO sheets remarkably reduced, ice crystals are unable to push the sheets to the crystal boundary (Qiu *et al.,* 2012).

The crystal structures of graphite, GO, and rGO aerogels were determined by XRD analysis (see figure 5.4). It was found that, instead of peak at 10.5ºC for GO, a new broadened diffraction peak, which is close to the peak of the graphite, appeared in the aerogels. These results indicate π–π stacking between the reduced graphene oxide sheets in aerogel and inhomogeneous graphite-like carbon crystalline state (Masjedi-Arani *et al.,* 2017; Safajou *et al.,* 2017; Shadkam *et al.,* 2020).

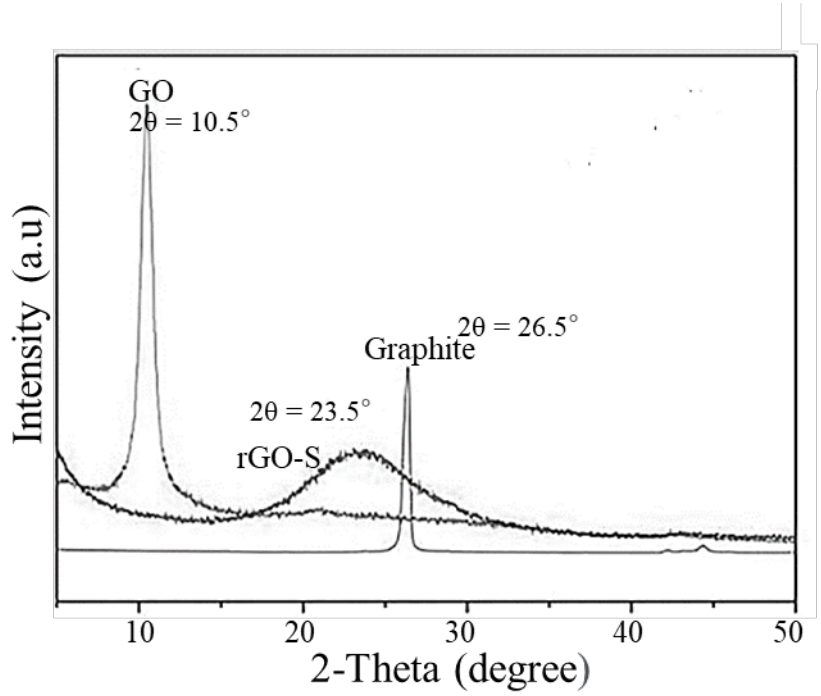

Figure 5. 4 XRD patterns of GO, graphite and rGO-S aerogel.

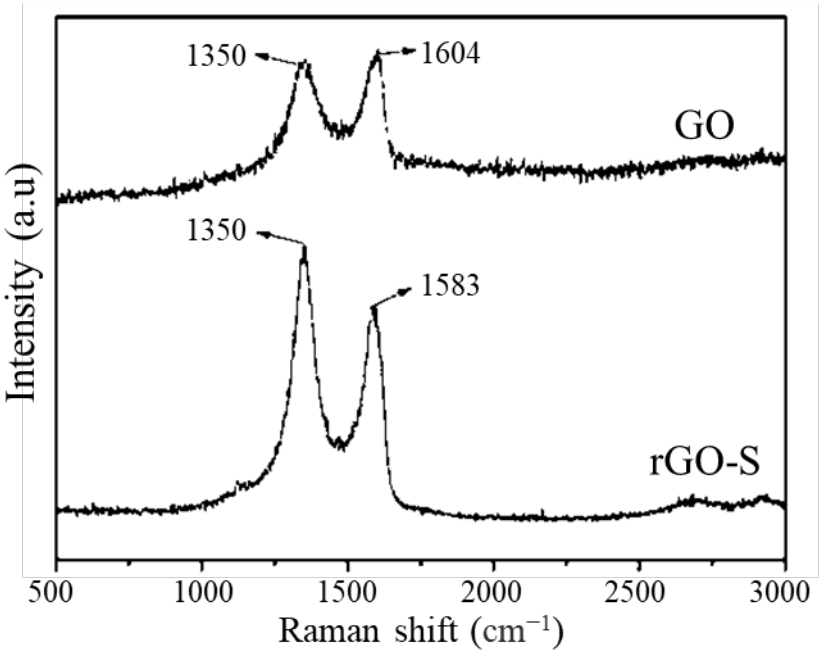

Figure 5. 5 Raman spectra of GO and rGO-S.

The Raman spectra of GO and rGO-S aerogels are illustrated in Figure 5.5. The spectrum of GO exhibited two prominent bands located at 1604 cm^{-1} (G band) and 1350 cm^{-1} (D band). The spectrum of S-rGA also has both G and D bands (at 1583 and 1350 cm^{-1}). The G band shifted from 1604 to 1583 cm^{-1}, indicating the reduction of GO during the chemical treatment. The intensity ratio of the D and G band (I_D/I_G) is commonly used as an indicator of the relative disorder present in graphitic structures. The increment of I_D/I_G for rGO-S aerogel While ID/IG

for GO is stable, the increment of ID/IG for rGO-S aerogel demonstrates the reduction of exfoliated GO (Zhang *et al.,* 2018).

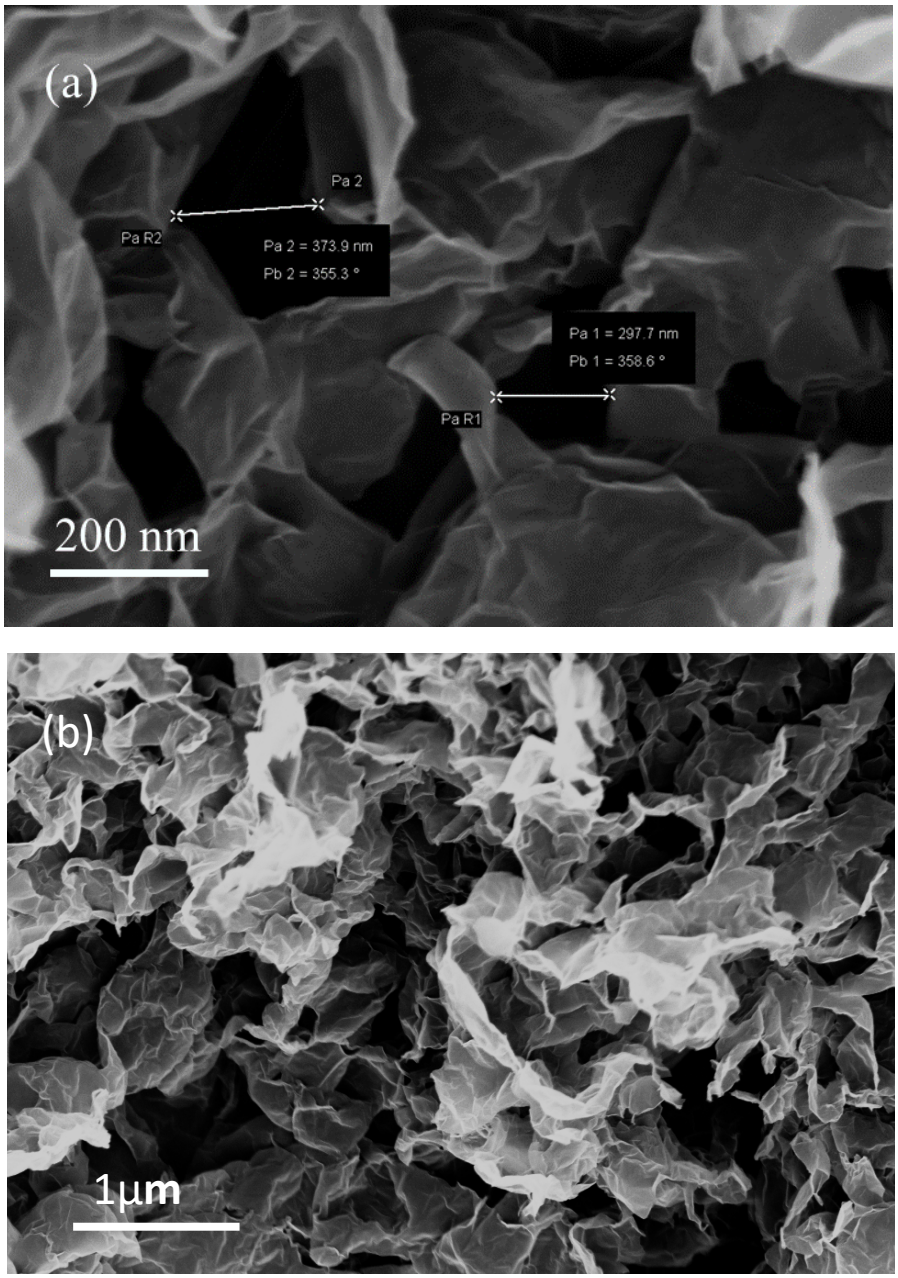

Figure 5. 6 SEM images of rGO-S aerogels.

The morphology of the produced graphene aerogel was investigated using scanning electron microscope (SEM) technique. Figure 5.6 demonstrates SEM images of rGO-S aerogels. The three-dimensional structure of the rGO-S aerogel can be clearly seen from SEM images possessing interconnected porous structure. Graphene oxide sheets stack and arrange to form rGO hydrogel.

5.7 Conclusion

Ambient pressure dried graphene aerogels were successfully obtained with ordinary instruments by recasting reduced graphene oxide hydrogel with an ice-template method. $NaHSO_3$ can enhance the de-epoxidation of GO sheets. The removal of each epoxy moiety on the edge of the GO plane can give two carbon atoms from the covalent bond and add them to the basal plane to increase the electrical conductivity (Shadkam *et al.,* 2020). After annealing process to remove remaining oxygen – containing moieties in aerogel, it can be used in some applications of both storage and transfer of energy for batteries. I believe that ambient pressure dried graphene aerogel obtained by using ordinary devices with freeze-thaw process can be large scale and low-cost industrial product.

References

Chabot, V., Higgins, D., Yu, A., Xiao, X., Chen, Z. and Zhang, J., 2014. A review of graphene and graphene oxide sponge: material synthesis and applications to energy and the environment. *Energy & Environmental Science*, 7(5), p.1564.

Chen, C., Zhu, X. and Chen, B., 2018. Covalently cross-linked graphene oxide aerogel with stable structure for high-efficiency water purification. *Chemical Engineering Journal*, 354, pp.896-904.

Chen, W., Yan, L. and Bangal, P., 2010. Chemical Reduction of Graphene Oxide to Graphene by Sulfur-Containing Compounds. *The Journal of Physical Chemistry C*, 114(47), pp.19885-19890.

Chen, X., Lai, D., Yuan, B., and Fu, M. (2019) Tuning oxygen clusters on graphene oxide to synthesize graphene aerogels with crumpled nanosheets for effective removal of organic pollutants. *Carbon*, 143, pp. 897-907.

Chua, C. and Pumera, M., 2014. Chemical reduction of graphene oxide: a synthetic chemistry viewpoint. *Chem. Soc. Rev.*, 43(1), pp.291-312.

Geng, Y., Li, Z., Chen, M., Zhao, H. and Zhang, L., 2020. The preparation of graphene foam by one-step reduction and air-drying for oil–water separation. *Journal of Sol-Gel Science and Technology*, 94(2), pp.375-383.

Gorgolis, G. and Galiotis, C., 2017. Graphene aerogels: a review. *2D Materials*, 4(3), p.032001.

Gürünlü, B., Taşdelen Yücedağ, Ç. and Bayramoğlu, M., 2020. Green Synthesis of Graphene from Graphite in Molten Salt Medium. *Journal of Nanomaterials*, 2020, pp.1-12.

He, M., Zhang, R., Zhang, K., Liu, Y., Su, Y. and Jiang, Z., 2019. Reduced graphene oxide aerogel membranes fabricated through hydrogen bond mediation for highly efficient oil/water separation. *Journal of Materials Chemistry A*, 7(18), pp.11468-11477.

Korkmaz, S. and Kariper, İ., 2020. Graphene and graphene oxide-based aerogels: Synthesis, characteristics and supercapacitor applications. *Journal of Energy Storage*, 27, p.101038.

Li, C., Chen, X., Shen, L., and Bao, N. (2020) Revisiting the Oxidation of Graphite: Reaction Mechanism, Chemical Stability, and Structure Self-Regulation. *ACS Omega*, 5(7), pp. 3397-3404.

Long, L., Weng, Y. and Wang, Y., 2018. Cellulose Aerogels: Synthesis, Applications, and Prospects. *Polymers*, 10(6), p.623.

Ma, Q., Song, J., Jin, C., Li, Z., Liu, J., Meng, S., Zhao, J. and Guo, Y., 2013. A rapid and easy approach for the reduction of graphene oxide by formamidinesulfinic acid. *Carbon*, 54, pp.36-41.

Maleki, H., 2016. Recent advances in aerogels for environmental remediation applications: A review. *Chemical Engineering Journal*, 300, pp.98-118.

Masjedi-Arani, M. and Salavati-Niasari, M., 2017. Novel synthesis of Zn2GeO4/graphene nanocomposite for enhanced electrochemical hydrogen storage performance. *International Journal of Hydrogen Energy*, 42(27), pp.17184-17191.

Nosrati, H., Mamoory, R., Dabir, F., Perez, M., Rodriguez, M., Svend Le, D. and Bünger, C., 2019. In situ synthesis of three-dimensional graphene-hydroxyapatite nano powders via hydrothermal process. *Materials Chemistry and Physics*, 222, pp.251-255.

Nosrati, H., Mamoory, R., Dabir, F., Svend Le, D., Bünger, C., Perez, M. and Rodriguez, M., 2019. Effects of hydrothermal pressure on in situ synthesis of 3D graphene- hydroxyapatite nano structured powders. *Ceramics International*, 45(2), pp.1761-1769.

Park, S. and Ruoff, R., 2010. Erratum: Chemical methods for the production of graphenes. *Nature Nanotechnology*, 5(4), pp.309-309.

Qiu, L., Liu, J., Chang, S., Wu, Y. and Li, D., 2012. Biomimetic superelastic graphene-based cellular monoliths. *Nature Communications*, 3(1).

Rowlinson, J. and Widom, B., 2013. *Molecular Theory Of Capillarity*. Newburyport: Dover Publications.

Safajou, H., Khojasteh, H., Salavati-Niasari, M. and Mortazavi-Derazkola, S., 2017. Enhanced photocatalytic degradation of dyes over graphene/Pd/TiO2 nanocomposites: TiO2 nanowires versus TiO2 nanoparticles. *Journal of Colloid and Interface Science*, 498, pp.423-432.

Salehabadi, A., Salavati-Niasari, M. and Ghiyasiyan-Arani, M., 2018. Self-assembly of hydrogen storage materials based multi-walled carbon nanotubes (MWCNTs) and Dy3Fe5O12 (DFO) nanoparticles. *Journal of Alloys and Compounds*, 745, pp.789-797.

Shadkam, R., Naderi, M., Ghazitabar, A., Asghari-Alamdari, A. and Shateri, S., 2020. Enhanced electrochemical performance of graphene aerogels by using combined reducing agents based on mild chemical reduction method. *Ceramics International*, 46(14), pp.22197-22207.

Wang, H., Wang, C., Liu, S., Chen, L. and Yang, S., 2019. Superhydrophobic and superoleophilic graphene aerogel for adsorption of oil pollutants from water. *RSC Advances*, 9(15), pp.8569-8574.

Wasalathilake, K., Galpaya, D., Ayoko, G. and Yan, C., 2018. Understanding the structure-property relationships in hydrothermally reduced graphene oxide hydrogels. *Carbon*, 137, pp.282-290.

Wu, D., Wang, T., Wang, L. and Jia, D., 2019. Hydrothermal synthesis of nitrogen, sulfur co-doped graphene and its high performance in supercapacitor and oxygen reduction reaction. *Microporous and Mesoporous Materials*, 290, p.109556.

Xiong, G., Luo, H., Zuo, G., Ren, K. and Wan, Y., 2015. Novel porous graphene oxide and hydroxyapatite nanosheets-reinforced sodium alginate hybrid nanocomposites for medical applications. *Materials Characterization*, 107, pp.419-425.

Yang, H., Zhang, T., Jiang, M., Duan, Y. and Zhang, J., 2015. Ambient pressure dried graphene aerogels with superelasticity and multifunctionality. *Journal of Materials Chemistry A*, 3(38), pp.19268-19272.

Yang, Z., Zheng, Q., Qiu, H., Li, J. and Yang, J., 2015. A simple method for the reduction of graphene oxide by sodium borohydride with $CaCl_2$ as a catalyst. *Carbon*, 86, p.372.

Zhang, W., Chen, J., Hu, Y., Fang, Z., Cheng, J. and Chen, Y., 2018. Adsorption characteristics of tetrabromobisphenol A onto sodium bisulfite reduced graphene oxide aerogels. *Colloids and Surfaces A: Physicochemical and Engineering Aspects*, 538, pp.781-788.

Zhao, Y., Hu, C., Hu, Y., Cheng, H., Shi, G. and Qu, L., 2012. A Versatile, Ultralight, Nitrogen-Doped Graphene Framework. *Angewandte Chemie*, 124(45), pp.11533-11537.

Zu, G., Shimizu, T., Kanamori, K., Zhu, Y., Maeno, A., Kaji, H., Shen, J. and Nakanishi, K., 2018. Transparent, Superflexible Doubly Cross-Linked Polyvinylpolymethylsiloxane Aerogel Superinsulators via Ambient Pressure Drying. *ACS Nano*, 12(1), pp.521-532.

Chapter 6 Conclusion and future work

This chapter summarizes the conclusion of results of the work which is completed in this thesis and offers the areas that could be investigated in future.

6.1 Thesis conclusion

This thesis reports the progressive development of aerogels such as synthesis techniques, reinforcement techniques to improve mechanical properties, technical characteristics, and development of aerogel applications.

In chapter 3 of this thesis, sodium bicarbonate ambient pressure drying approach is used to synthesize low cost monolithic and composite silica aerogels mixed with GO by using water glass as a precursor. SiO_2-GO composite aerogel with 0.1 wt% GO has the biggest surface area which is 578 m^2/g, with an average pore diameter of 6.45 nm and a pore volume of 0.98 cm^3/g. The strong interaction between GO and silica matrix provides mechanical strength enhancements. The mechanical strength of aerogels is increased, and the aerogel composite displays toughness instead of traditional fragility. In addition to these, monolithic and composite Si/GO aerogels were degassed at 200 °C because the particle size and the pore diameter slightly decreased when the heating temperature is more than 200 °C (Liu *et al.,* 2013). However, graphene oxide aerogels with different nanoparticles (see chapter 4) were degassed at 80 °C. The reason to use different temperature is that reduced graphene oxide aerogels have larger pore sizes so 80 °C is the optimum temperature for degassing.

Chapter 4 presents production of different metal oxide nanoparticles, such as GeO_2, $CoFe_2O_4$, and Fe_3O_4. These metal oxide nanoparticles are then used as additives to produce reduced graphene oxide (rGO) composite aerogels for investigation of physical properties such as surface area, morphology, the chemical composition, and electrochemical measurements as an anode material for LIBs. Crystalline sizes of metal oxides are determined from using XRD Bragg reflections by the Scherrer equation. In addition, this chapter describes how to prepare samples for electrochemical testing of aerogels as an anode material. Based on BET analysis, which gives precise specific surface area evaluation of aerogels, Type IV adsorption isotherm is found for rGO aerogel. The rGO aerogel has the highest specific surface area, 1225.035 m^2g^{-1}, but loading with large number of nanoparticles reduces the surface area of composite aerogels.

Lastly, electrochemical results as anode materials of aerogels are not as good as expected. The primary reason may be that the ionic and electronic electrical conductivity of aerogels are comparatively inferior, leading to the low electronic transfer and ion diffusion efficiency, which might severely decline the electrochemical properties for Li-ion batteries as a semiconductor

material (P. Pender et al., 2020). In order to solve this problem, annealing process can be done to remove remaining oxygen containing moieties in aerogel to raise the electrical conductivity. In chapter 5 of this thesis, reduced graphene oxide aerogels are synthesized by using ambient pressure drying (APD) method. The main aim of this chapter is to explain how to obtain large-scale and cheap industrial production of graphene aerogels. The aerogels produced with APD generally show a severe shrinkage or collapse of the wet gel in volume after drying because of the capillary pressure (*P*) (Zhao *et al.,* 2012). If contact angle (θ) and surface tension (γ) are constant, *P* is inversely proportional to the pore radius (R). Therefore, the enlargement of the pores of graphene gels will be an extremely effective way to reduce the capillary force (Yang *et al.,* 2015).

In this chapter, slower cooling rates of freezing gives larger pore diameters by recasting reduced graphene oxide hydrogel with an ice-template method. Reduction mechanism which uses $NaHSO_3$ as a reductant is explained. $NaHSO_3$ can improve the de-epoxidation of GO sheets (Shadkam et al., 2020).

6.2 Future work

As mentioned in chapter 5, graphene aerogels have many excellent properties, including high specific surface area, low density, and excellent conductivity, which make them excellent candidates for electrode material of supercapacitors and lithium-ion batteries (Xiong *et al.,* 2019).

The most common methods for generating graphene monolith from GO suspension are the chemical and hydrothermal reductions. The chemical route operates at low temperatures compared with thermal reduction which operates at high temperatures and the pressures. Thus, chemical reduction equipment and conditions are much more usable than thermal reduction, which is undeniable for practical applications (Moon *et al.,* 2010; Gorgolis and Galiotis, 2017; Nosrati *et al.,* 2019). Li et al. (2018) recently used graphene paper in electrode production and found out a capacity of 57 Fg^{-1} which was enhanced by additives. Moreover, Ghazitabar et al. (2019) produced electrodes from graphene aerogel, which was reduced just by l-ascorbic acid (LAA) and obtained 71 Fg^{-1} capacitances. As mentioned in chapter 5, $NaHSO_3$ can develop the de-epoxidation of GO sheets, as a result the electrical conductivity of reduced graphene oxide (Shadkam *et al.,* 2020) increases. Here as future work, we propose a new combined system which is composed of L-AA and $NaHSO_3$ acting as reducing agents. The enhancement of mechanical stability of synthesized Graphene Hydrogel (GH) and Aerogel (GA) will be discussed through the exploration of surface chemistry of rGO sheets and the pore structure. Accurately, the electrochemical performance of the best sample will be characterized and

compared to some of the reported results in the literature. Besides all these, ice template method will be improved by using further reduction of graphene oxide hydrogel to remove oxygen moieties, so without annealing, it can be used for lithium-ion batteries with utilising different metal oxide nanoparticles.

Compressive tests will also be conducted along the axial direction and radial direction of the further reduced graphene oxide aerogels. The good compressibility of the graphene aerogels provides collection of the absorbed oil by simple absorption–squeezing cycles (Li et al., 2014). If the results show that graphene aerogels can be recycled as a compressive material, then these graphene aerogels will be used for oil absorption.

6.2.1 Fabrication of further reduction graphene aerogels

In brief, 10 ml graphene oxide dispersion will be first mixed with different ratios of LAA and $NaHSO_3$, then the resultant slurries will be sealed in glass vial heated for 45 min at 95ºC for synthesis partially reduced graphene oxide hydrogel. Secondly, the hydrogel will be cooled at room temperature and followed by freeze thaw process in the freezer (-18ºC) and room temperature. The freeze-recast hydrogel will be further reduced (95ºC) by the initial reductants to get completely reduced graphene hydrogel by LAA and $NaHSO_3$. Lastly, the reduced graphene oxide hydrogel will be washed by dialysis water to remove soluble species and dried in the oven at 60ºC for 24 hours to produce the ambient pressure dried graphene aerogel.

After production of ambient pressure dried graphene aerogels, all the characterization tests will be done as mentioned above.

6.3 Reduced graphene oxide - silica nanocomposite aerogels

More than 10 million m^3 of crude oil is generated worldwide every day (Short-Term Energy Outlook - U.S. Energy Information Administration (EIA), 2020). This oil is typically generated in remote areas and transported to processing refineries. Around 5.8 million tonnes of crude oil have been poured into the sea during transportation over the last 50 years (Statistics - ITOPF, 2020). Recently, the most typical routes for oil spill clean-up at sea contain: i) chemical methods, using dispersants/solidifiers (Ivshina *et al.,* 2015); ii) bioremediation, including membrane bioreactor technology; iii) in-situ controlled burning (Sepehri and Sarrafzadeh, 2018); iv) mechanical methods, through booms and skimmers; v) sorption (Sepehri and Sarrafzadeh, 2019). Among the several procedures developed are the cleaning of water spills due to the specific ability to remove contaminants without damaging the environment (Gao *et al.,* 2019).

Early successful strategies to generate SiO_2 aerogels with tailored hydrophobicity have focused on surface modification with hydrophobic non-hydrolyzable functionalities such as fluoro-

propyl (Thakkar *et al.,* 2020). Such strongly hydrophobic organosilica was successfully used for the separation of water from organic solvents (Hrubesh *et al.,* 2001; John G. Reynolds *et al.,* 2001).

Hydrophilic carbon nanostructures such as carbon dots and graphene oxide (GO) have been used as additives owing to their ability to disperse in silica matrix (Lei *et al.,* 2017). In chapter 3, the production of silica aerogels filled with GO increased mechanical strength of composite aerogels compared to that of the monolithic silica aerogel.

In the future work, the application of SiO_2 composite aerogels containing reduced graphene oxide (rGO) as oil sorbents will be produced by a sol-gel method based on co-gelaation of waterglass as silica precursor and of previously prepared graphene oxide.

References

Eia.gov. 2020. *Short-Term Energy Outlook - U.S. Energy Information Administration (EIA)*. [online] Available at: <https://www.eia.gov/outlooks/steo/report/natgas.php>

Gao, X., Zhou, Y., Liu, S., Tan, Y., Cheng, Z. and Shen, Z., 2019. FeN3-embedded carbon as an efficient sorbent for mercury adsorption: A theoretical study. *Chemical Engineering Journal*, 374, pp.1337-1343.

Ghazitabar, A., Naderi, M., Fatmehsari Haghshenas, D. and Rezaei, M., 2019. Synthesis of N-doped graphene aerogel/Co3O4/ZnO ternary nanocomposite via mild reduction method with an emphasis on its electrochemical characteristics. *Journal of Alloys and Compounds*, 794, pp.625-633.

Gorgolis, G. and Galiotis, C., 2017. Graphene aerogels: a review. *2D Materials*, 4(3), p.032001.

Hrubesh, L., Coronado, P., and Satcher, J. (2001) Solvent removal from water with hydrophobic aerogels. *Journal of Non-Crystalline Solids*, 285(1-3), pp. 328-332.

Itopf.org. 2020. *Statistics - ITOPF*. [online] Available at: <https://www.itopf.org/knowledge-resources/data-statistics/statistics/> [Accessed 21 September 2020].

Ivshina, I., Kuyukina, M., Krivoruchko, A., Elkin, A., Makarov, S., Cunningham, C., Peshkur, T., Atlas, R. and Philp, J., 2015. Oil spill problems and sustainable response strategies through new technologies. *Environmental Science: Processes & Impacts*, 17(7), pp.1201-1219.

John G. Reynolds, Paul R. Coronado, (2001) Hydrophobic Aerogels for Oil-Spill Cleanup? Intrinsic Absorbing Properties. *Energy Sources*, 23(9), pp. 831-843.

Lei, Y., Hu, Z., Cao, B., Chen, X., and Song, H. (2017) Enhancements of thermal insulation and mechanical property of silica aerogel monoliths by mixing graphene oxide. *Materials Chemistry and Physics*, 187, pp. 183-190.

Li, J., Li, J., Meng, H., Xie, S., Zhang, B., Li, L., Ma, H., Zhang, J. and Yu, M., 2014. Ultra-light, compressible and fire-resistant graphene aerogel as a highly efficient and recyclable absorbent for organic liquids. *Journal of Materials Chemistry A*, 2(9), p.2934.

Li, X., Tang, Y., Song, J., Yang, W., Wang, M., Zhu, C., Zhao, W., Zheng, J. and Lin, Y., 2018. Self-supporting activated carbon/carbon nanotube/reduced graphene oxide flexible electrode for high performance supercapacitor. *Carbon*, 129, pp.236-244.

Nosrati, H., Mamoory, R., Dabir, F., Svend Le, D., Bünger, C., Perez, M. and Rodriguez, M., 2019. Effects of hydrothermal pressure on in situ synthesis of 3D graphene- hydroxyapatite nano structured powders. *Ceramics International*, 45(2), pp.1761-1769.

P. Pender, J., Jha, G., Youn, D., Ziegler, J., Andoni, I., Choi, E., Heller, A., Dunn, B., Weiss, P., Penner*, R. and Mullins*, C., 2020. Electrode Degradation in Lithium-Ion Batteries. *Acs Nano*, pp.1243–1295.

Sepehri, A. and Sarrafzadeh, M., 2018. Effect of nitrifiers community on fouling mitigation and nitrification efficiency in a membrane bioreactor. *Chemical Engineering and Processing - Process Intensification*, 128, pp.10-18.

Sepehri, A. and Sarrafzadeh, M., 2019. Activity enhancement of ammonia-oxidizing bacteria and nitrite-oxidizing bacteria in activated sludge process: metabolite reduction and CO_2 mitigation intensification process. *Applied Water Science*, 9(5).

Shadkam, R., Naderi, M., Ghazitabar, A., Asghari-Alamdari, A. and Shateri, S., 2020. Enhanced electrochemical performance of graphene aerogels by using combined reducing agents based on mild chemical reduction method. *Ceramics International*, 46(14), pp.22197-22207.

Shadkam, R., Naderi, M., Ghazitabar, A., Asghari-Alamdari, A. and Shateri, S., 2020. Enhanced electrochemical performance of graphene aerogels by using combined reducing agents based on mild chemical reduction method. *Ceramics International*, 46(14), pp.22197-22207.

Thakkar, S., Pinna, A., Carbonaro, C., Malfatti, L., Guardia, P., Cabot, A. and Casula, M., 2020. Performance of oil sorbents based on reduced graphene oxide–silica composite aerogels. *Journal of Environmental Chemical Engineering*, 8(1), p.103632.

Xiong, C., Li, B., Lin, X., Liu, H., Xu, Y., Mao, J., Duan, C., Li, T. and Ni, Y., 2019. The recent progress on three-dimensional porous graphene-based hybrid structure for supercapacitor. *Composites Part B: Engineering*, 165, pp.10-46.

Yang, H., Zhang, T., Jiang, M., Duan, Y. and Zhang, J., 2015. Ambient pressure dried graphene aerogels with superelasticity and multifunctionality. *Journal of Materials Chemistry A*, 3(38), pp.19268-19272.

Zhao, Y., Hu, C., Hu, Y., Cheng, H., Shi, G. and Qu, L., 2012. A Versatile, Ultralight, Nitrogen-Doped Graphene Framework. *Angewandte Chemie*, 124(45), pp.11533-11537.

Chapter 7 Appendix

7.1 Appendix A. Degassing process and surface area measurements with Surfer analyser

The main page of Surfer acquisition program which is shown in Figure 7.1 includes the commands and dialog boxes to set parameters and to save the analysis. In the beginning, for BET and BJH analysis, samples are degassed. It starts with degassing of empty burette for 15 mins at 120 ºC to vaporise water adsorbed on the glass surface of the burette. Then the weight (m_1) of the empty degassed burette is determined by utilising a microbalance. Next stage is degassing the sample of desired mass (0.1-0.2 g) for 8 hours at 200 ºC. Figure 7. 2 displays automatic temperature control page for degassing the samples.

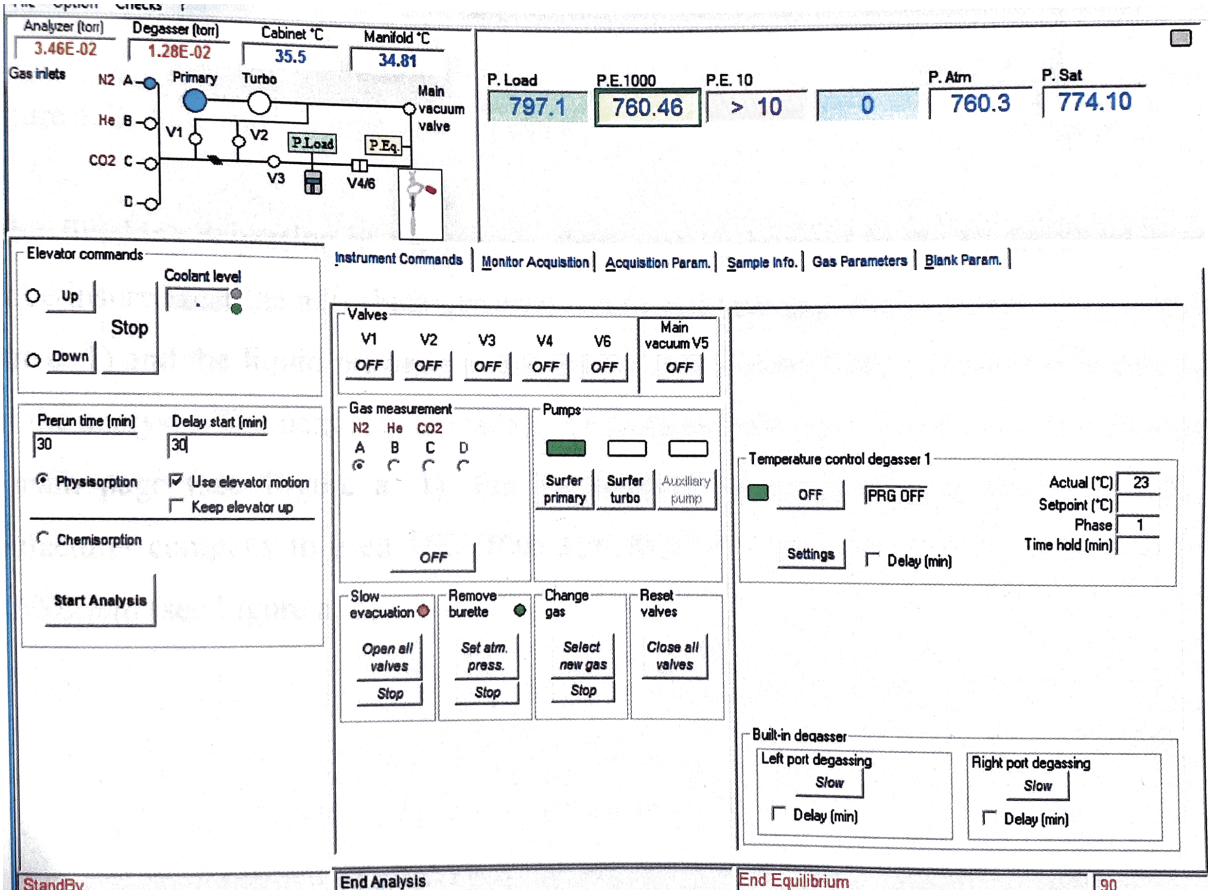

Figure 7. 1 Surfer acquisition main page.

Following degassing stage, the net mass of the degasses sample is calculated as $m=m_2 - m_1$. Then, the burette is put into the Surfer axquisition. The adsorbate gas utilised is nitrogen. The acquisition parameters tab of the main page (see figure 7.1) is chosen. For mesoporous sample, *METHOD MACROPORE and MESOPORE WITH 10 TORR TRANSD.mtd* is used (see Figure 7. 3).

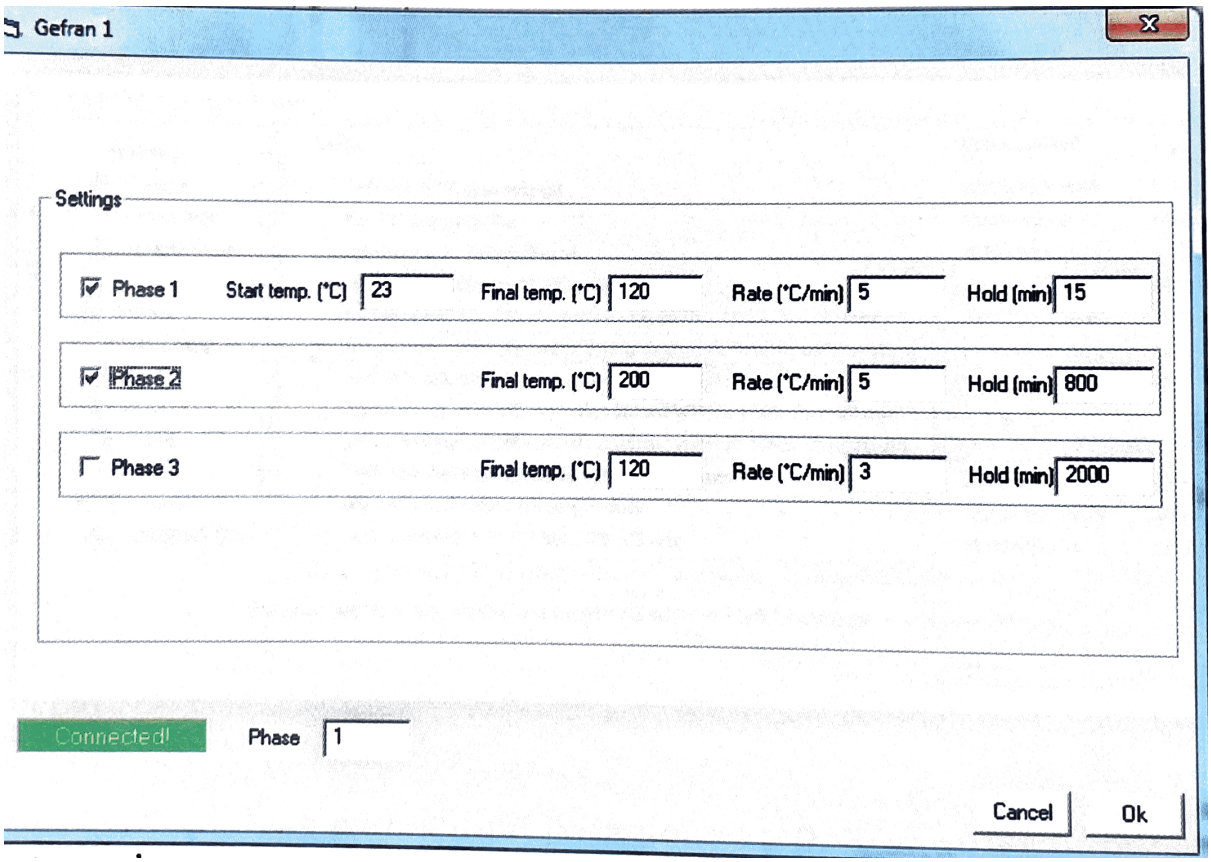

Figure 7. 2 Automatic temperature control

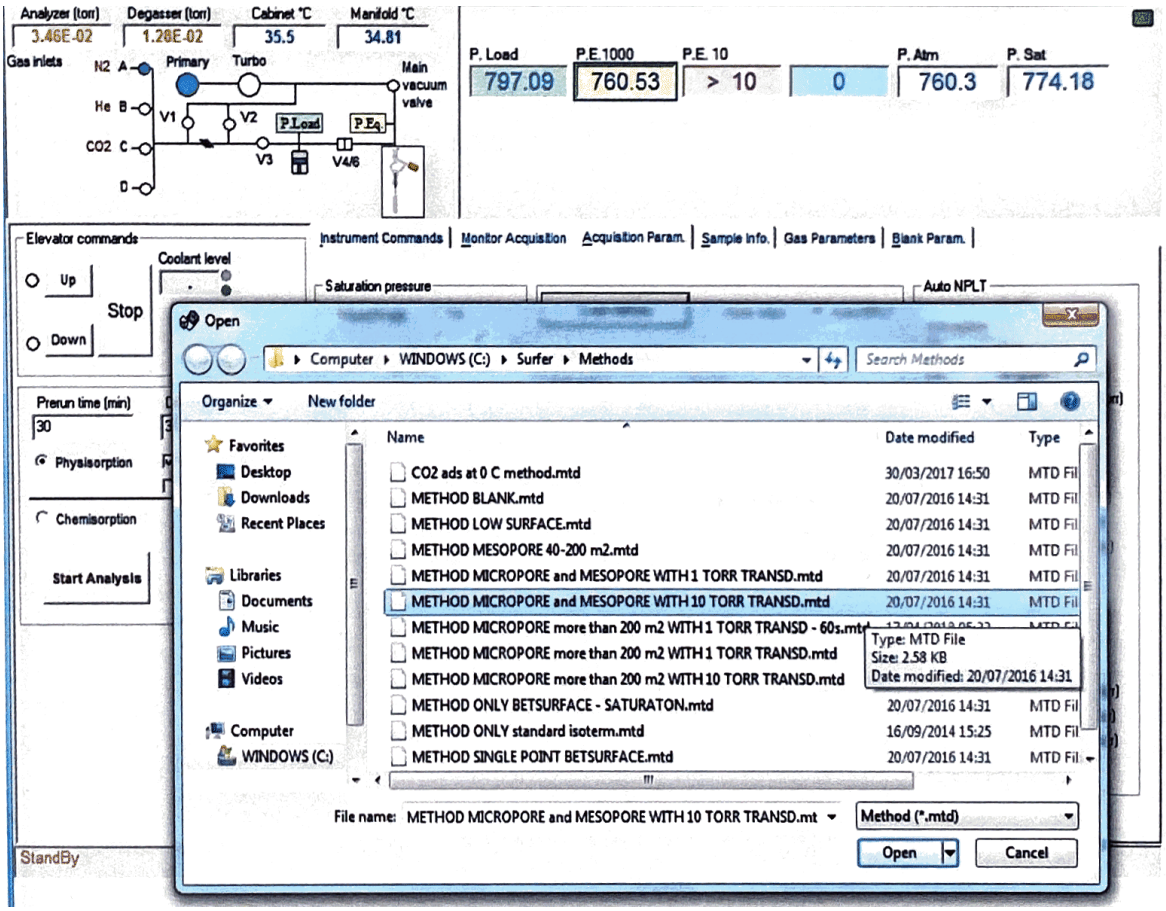

Figure 7. 3 Load method for acquisition parameters tab.

Materials information for example the name, the operation date, mass of the material and density of the material are written by using the material info tab to show the page of the material information in Figure 7. 3.

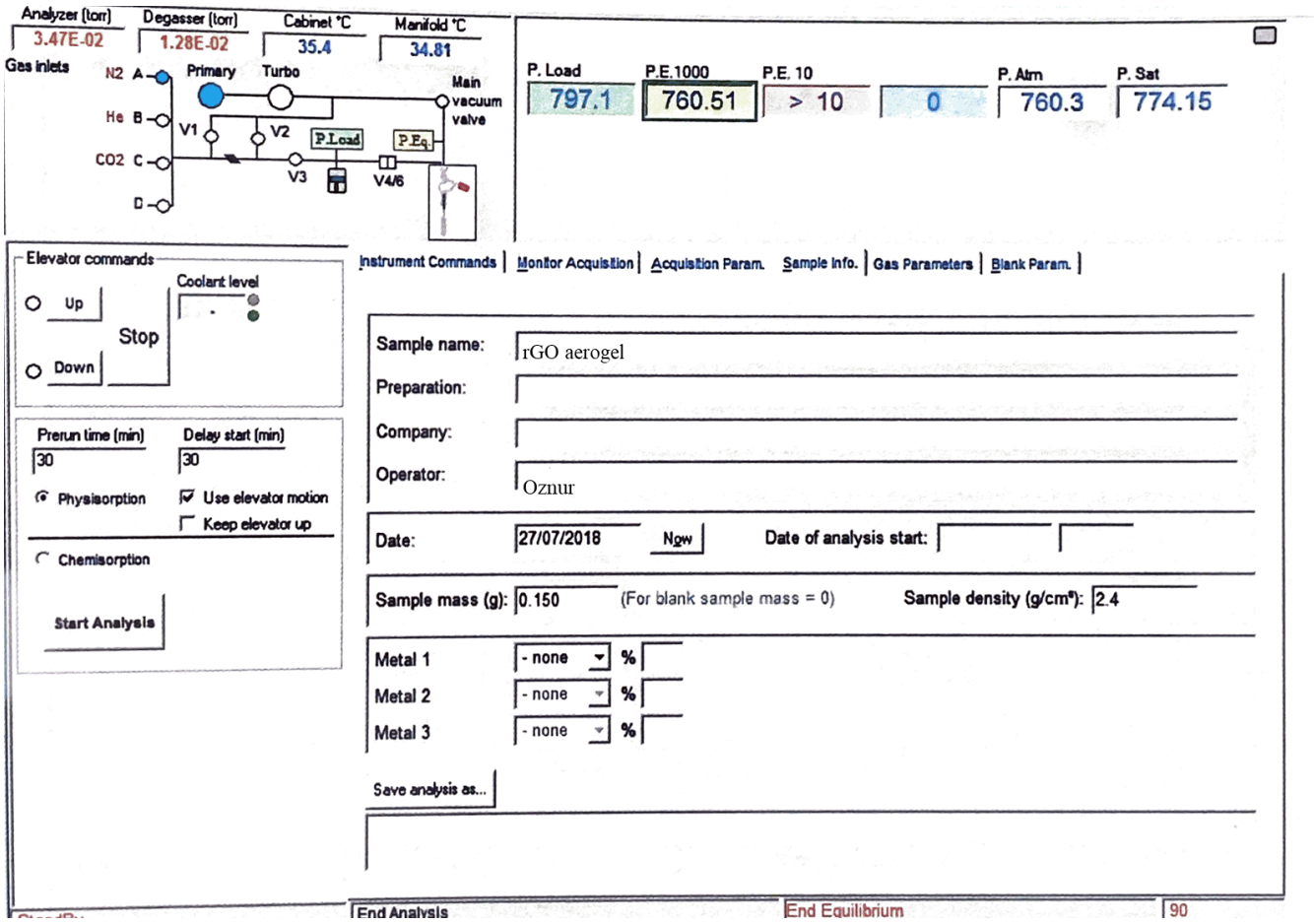

Figure 7. 4 Sample info page

The blank parameter of the burette must be filled by using blank parameter tab which is shown in Figure 7.4. Following the finishing the setting of all parameters, it is suggested that setting the pre-run time and the delay time at 30 minutes for each.

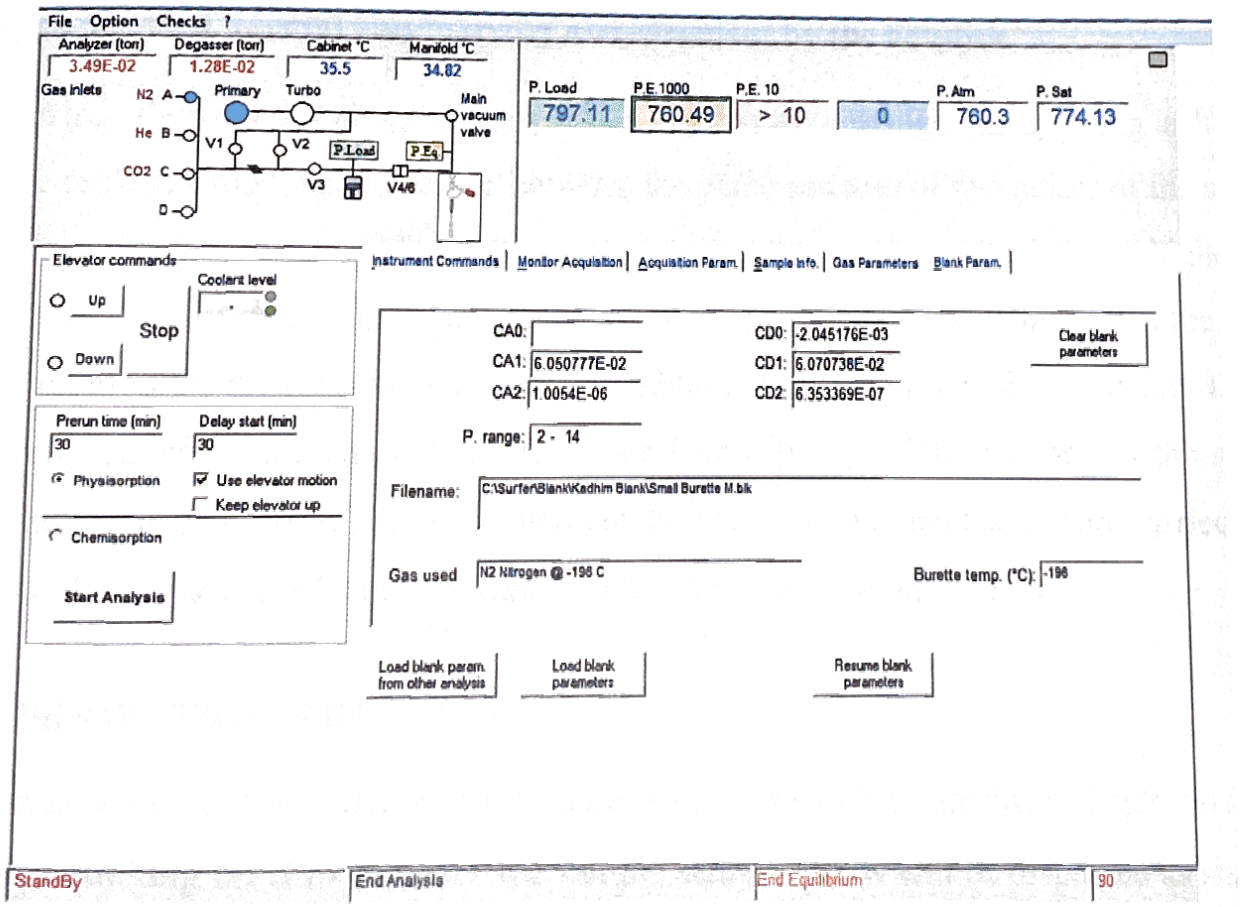

Figure 7. 5 Blank parameters tab.

Before starting the analysis, the system requires to be outgassed. When degassing is completed, the pressure of the system should be E-03 torr and then the turbo pump is used to reach vacuum of E-06 torr. Finally, the analysis is started by pressing the start analysis tab.

7.2 Appendix B. Cell preparation

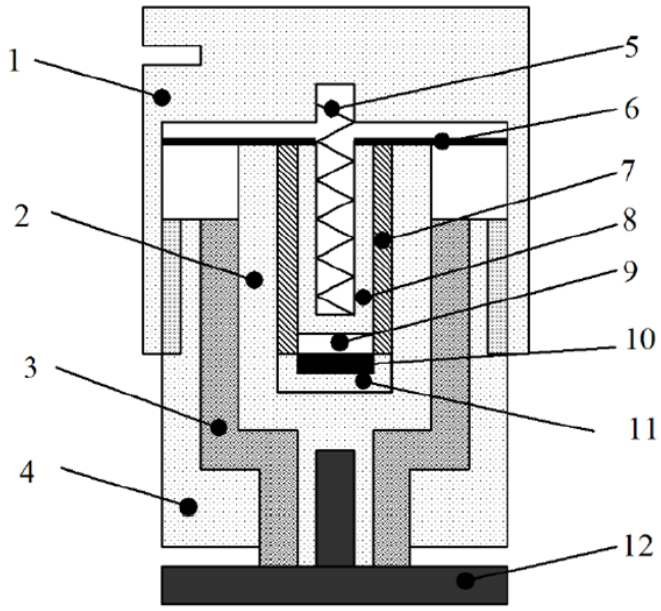

1. Top (stainless steel)
2. Inner part (titanium)
3. Insulator
4. Bottom (stainless steel)
5. Spring
6. Sealing ring
7. Insulator
8. Cylinder (titanium)
9. Counter electrode (Li metal)
10. Cathodic material
11. Coated current collector
12. Working electrode contact

Figure 7. 6 Electrochemical cell scheme used in the experiments.

A cell must be assembled for electrochemical analysis. The scheme of the cell is primarily made of titanium (see Figure 7. 6). The counter electrode was placed into a titanium-made cylinder (8) and pressed with a spring (5) against the working electrode coated onto a titanium current collector (10). Between the two electrodes there was a separator soaked in the electrolyte. The cell assembling was arranged in an argon-filled glove box (H_2O < 1 ppm, O_2= 0.1 ppm). Electrodes have been placed in Swagelok-type cells in an Ar-filled glovebox (H_2O, O_2 < 0.1 ppm). Li metal (99.9%, Alfa-Aesar) used as both reference and counter electrode. A glass fiber separator was soaked with electrolyte (1 M $LiPF_6$ in 1:1 wt % ethylene carbonate (EC)/dimethyl carbonate (DMC), Novolyte). All electrochemical measurements were performed by using a Biologic instrument (VMP3) at room temperature. The electrodes were cycled between 0.01 and 3 V vs Li/Li^+ at a constant current density of 100 mAg^{-1}. 1 C is defined as 1 Ag^{-1}.

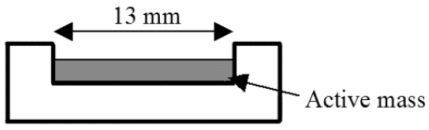

Figure 7. 7 Scheme of the current collector filled with active mass, with surface area = 1.3 cm^2.

5-10 mg electrode material has typically been put onto the current collector (see figure 7.7), followed by heat treatment to vaporise NMP and any H_2O absorbed on/in the materials. The

heat treatment was generally conducted at 100 °C overnight or even longer. The weight of electrode materials was measured and multiplied by 90% to only refer to the active materials. After that, the current collector was sent into the glove box, and assembled into the cell.

Cell voltage:

The free energy of the resulting chemical reaction can be determined from the Gibb free energy:

$$U^0 = \Delta E^0 = \frac{-\Delta G^0}{zF} \quad [V]$$

Current density:

The current density j is calculated by dividing the total current I flow through an electrode by the electrode area A. The normal case is that the geometrical area is used:

$$j = \frac{I}{A} \quad [A/cm^2]$$

Charge capacity:

The charge capacity Q is the total amount of charge obtainable from a cell:

$$Q = \int_{t_1}^{t_2} I(t)dt \quad [Ah]$$

7.3 Appendix C. List of publications

- During my master studies, I worked for the Scientific and Technological Research Council of Turkey (TUBITAK) on the project number 215M617.
- Akin, I. and Kaya, O., 2017. Microstructures and properties of silicon carbide- and graphene nanoplatelet-reinforced titanium diboride composites. Journal of Alloys and Compounds, 729, pp.949-959.
- 'Synthesis of sodium silicate-based silica aerogels with graphene oxide by ambient pressure drying'. This manuscript has been accepted by the Journal of Porous Materials. Requested minor revisions are in progress.

7.4 List of posters and certificates

1. University of Warwick, Faraday Conference 2017, poster presentation about Synthesis of waterglass-based silica aerogels reinforced with graphene oxide, Warwick.
2. Hult Prize Certificate, 2017.
3. Sensors Day 2018, Fitzwilliam College, University of Cambridge.
4. The International Symposium on Inorganic and Environmental Materials 2018 at Ghent University, June 17-21, 2018, Pand - Onderbergen - Ghent (Belgium). I gave a poster presentation, 'Graphene oxide immobilized in silica aerogels'.
5. I went to Zurich for 3 months (01/2019 to 04/2019) as a researcher and I worked laboratory for multifunctional materials in the Department of Materials at ETH Zurich
6. 1st Conference on Aerogel Inspired Materials is based at the Urban Sciences Building, 1 Science Square, September 18-20, 2019, Newcastle upon Tyne, NE4 5TG. My poster ' Preparation and Characterization of Reduced Graphene Oxide Aerogels Doped with Different Metal Oxide Nanoparticles for Lithium-Ion Batteries' won the second prize which is consisting of a signed certificate, a £50 RSC book voucher, a short book entitled “Elements of Popular Science” which was put together as part of the International Year of the Periodic Table celebrations, and a periodic table themed lanyard was awarded.